Edwards, K.J., Bach, W., Klaus, A., and the Expedition 336 Scientists
Proceedings of the Integrated Ocean Drilling Program, Volume 336

Site U1382[1]

Expedition 336 Scientists[2]

Chapter contents

Site summary

Integrated Ocean Drilling Program (IODP) Expedition 336 Hole U1382A was drilled 50 m west of Deep Sea Drilling Project (DSDP) Hole 395A at 22°45.353′N, 46°04.891′W, in 4483 m water depth. The primary objective for Hole U1382A was to install a subseafloor borehole observatory (CORK) to perform long-term coupled microbiological, biogeochemical, and hydrological experiments in uppermost basaltic crust in this area of very low conductive heat flow. Coring and downhole logging of basement were also conducted.

After the reentry cone with 53 m of 16 inch casing was jetted in, the hole was deepened by drilling with a 14¾ inch tricone bit to 110 meters below seafloor (mbsf) without coring. Basement was encountered at 90 mbsf, and 3 m of basement was penetrated in 30 min. The interval from 93 to 99 mbsf was drilled very quickly and is inferred to be sediment; however, the underlying formation to 110 mbsf was drilled slowly (2–3 m/h) without significant torque. Casing (10¾ inch) was installed and successfully cemented to 102 mbsf. Rotary core barrel (RCB) coring recovered basement from 110 to 210 mbsf (Cores 336-U1382A-2R through 12R). In total, 32 m of core was retrieved, with recovery rates ranging from 15% to 63%. This succession resembles the lithostratigraphy encountered in DSDP Holes 395 and 395A and provided excellent sampling material for various microbiological and petrologic studies.

The shipboard petrologists divided the core into eight lithologic units, comprising numerous subunits. Major unit boundaries are defined by contacts between massive and pillowed flows and interlayered sedimentary units. Each major lava flow unit consists of several cooling units, which are recognized by glassy or variolitic margins or marked changes in grain size. Results from thin section studies reveal a large range of grain sizes (glassy to medium grained) and diverse textures (aphanitic to subophitic or intersertal). Basalts are either aphyric or plagioclase-olivine-phyric and have <3% vesicles. Phenocryst contents range up to 25%, with plagioclase being more abundant than olivine. All of the volcanic rocks recovered from Hole U1382A are affected only by low-temperature alteration by seawater, manifesting as replacement of groundmass and phenocrysts, vesicle filling, glassy margin replacement, and vein formation with adjacent brown alteration halos. Chilled margins often show advanced palagonitization, which develops as blotchy alteration texture following the primary

---

[1] Expedition 336 Scientists, 2012. Site U1382. *In* Edwards, K.J., Bach, W., Klaus, A., and the Expedition 336 Scientists, *Proc. IODP,* 336: Tokyo (Integrated Ocean Drilling Program Management International, Inc.). doi:10.2204/iodp.proc.336.104.2012

[2] **Expedition 336 Scientists' addresses.**

variolitic texture of the mesostasis. The extent of alteration ranges up to 20%, with clay (smectite and celadonite) being the most abundant secondary phase, followed by Fe oxyhydroxides and minor zeolites and carbonates. The recovered section has between 13 and 20 veins/m, with vein thickness being usually <0.2 mm. A sedimentary unit in Cores 336-U1382A-8R and 9R features a variety of clasts, including plutonic and mantle rocks. The peridotites are weakly serpentinized harzburgites and lherzolites with a protogranular texture. The intensity of deformation of the gabbroic lithologies ranges from undeformed to mylonitic. Minor cataclastic deformation of the peridotites has led to the development of carbonate-filled vein networks, along which the rocks have been subjected to oxidative alteration, resulting in the breakdown of olivine to clay, oxide, and carbonate.

Physical properties measurements reveal typical *P*-wave velocities for these lithologies and a correlation between sonic velocity and porosity of the basalt. Elevated potassium and uranium concentrations in the oxidatively altered part of the core were revealed by natural gamma radiation (NGR) core scanning. Thermal conductivity also reflected the typical values associated with basalt and peridotite and showed small variations with depth.

Whole-rock geochemistry analyses reveal systematic differences in compositions between aphyric and porphyritic basalt, which are due to plagioclase accumulation in the porphyritic basalt. The aphyric basalts show a liquid line of descent that is controlled by the fractional crystallization of olivine. As the extent of alteration increases, weight loss on ignition (LOI) values and potassium concentrations also increase. Immobile trace element ratios (Zr/Y and Ti/Zr) indicate that parental magma compositions for the basalts above and below the sedimentary unit are different from each other. Petrographically and geochemically, the basalts correspond to the uppermost lithologic units identified in Hole 395A. Likewise, a sedimentary unit with varied plutonic and mantle rocks was also observed in Hole 395A.

A primary objective of basement coring was to obtain samples for microbiological analysis. We collected 46 hard rock and 2 sediment whole-round samples for these studies (11% of core recovered). Samples were preserved for ship-based (deep ultraviolet [UV] fluorescence scanning, culturing and enrichment, and fluorescent microsphere analysis) and shore-based (DNA and RNA analysis, fluorescence in situ hybridization [FISH], cell counting, and isotopic analysis) studies. Generally, 1–3 microbiology hard rock samples were collected from every core section. Hard rock samples span a range of lithologic units, alteration states, and presence of chilled margins, and some contain veins or fractures. Additionally, a few recovered plastic bags that held the fluorescent microsphere solutions in the core catcher were collected as a contamination check via DNA analysis.

An open-hole section of 105.61 m was logged over a period of ~19.5 h with two tool strings (the adapted microbiology combination I [AMC I] and the Formation MicroScanner [FMS]–Hostile Environment Natural Gamma Ray Sonde [HNGS]). Downhole log measurements include natural total and spectral gamma radiation, temperature, density, electrical resistivity, electrical images, and deep UV–induced fluorescence (acquired with the new Deep Exploration Biosphere Investigative tool [DEBI-t]). The borehole remained in good condition throughout logging, and no obvious tight spots were encountered in open hole. Integration of core and log measurements and observations showed excellent correspondence between potassium concentrations provided by shipboard NGR, the spectral gamma ray logging tool, and whole-rock geochemical analyses. FMS data were combined with images of the external surfaces of whole-round cores. Prominent veins with alteration halos in cores from the massive flows were matched with fractures in the FMS images. Also, logging results constrain the depth of the peridotite interval from 165 to 167 mbsf (based on density and low K/U ratios).

Downhole hydrologic (packer) tests failed because ship heave up to 3 m prevented the packer from sealing in the casing for more than 10 min.

A CORK to monitor and sample a single interval in uppermost basement was successfully installed in Hole U1382A. The 210 m deep hole was sealed with a 189 m long CORK with nine external umbilicals and a retrievable internal instrument string. The umbilicals include one for pressure monitoring, two for microbiological sampling, and six for fluid sampling. The retrievable internal instrument string comprises several osmotic pump-driven samplers for basement fluids and microorganisms as well as enrichment experiments, an oxygen probe, and a thermistor with data recorder. The samplers and probes extend from 146 to 174 mbsf and are kept in position by a 150 lb sinker bar at 177 m. A pressure gauge and a fast-pumping OsmoSampler are situated in the wellhead and monitor/sample fluids from 162 mbsf.

Operations

The primary objective for Hole U1382A was to install a single-level CORK to perform long-term coupled microbiological, biogeochemical, and hydrological experiments in uppermost basaltic crust. We installed a reentry cone with 53 m of 16 inch casing, installed 102 m of 10¾ inch casing and cemented it a few meters into the basaltic basement, cored 100 m of basalt below the casing, conducted downhole logging and hydrologic (packer) experiments, and installed a CORK that extends to 188.7 mbsf.

After operations in Hole 395A, we intended to go directly to Hole U1382A (50 m west of Hole 395A). However, we had to leave the area because of Tropical Storm Philippe. After the ship was secured for transit at 0215 h on 29 September 2011, we headed to the northeast to avoid the approaching storm (all times are local ship time, Universal Time Coordinated [UTC] – 3 h). After Tropical Storm Philippe crossed over the North Pond drilling area, we returned to Hole U1382A at 1224 h on 1 October. All operational tasks at Site U1382, along with task start and end times, are listed in Table T1.

We assembled a reentry cone and 52.98 m of 16 inch casing and lowered it to the seafloor. The trip was temporarily suspended to install the camera system, which was lowered as the pipe trip continued to just above the seafloor. When the casing shoe was just above the seafloor, the top drive was picked up and the drill string was spaced out to start Hole U1382A. We started jetting in the reentry system at 0745 h on 2 October. After 2.75 h the reentry cone mud skirt was landed on the seafloor and verified with the camera system, and the casing running tool was released from the casing. The camera system was then pulled to the surface as the drill string and running tool were pulled back to the rig floor. The bottomhole assembly (BHA) was set back, and the running tool was detorqued at the rig floor. The BHA for drilling the 14¾ inch hole was assembled, and the drill string was tripped to just above the reentry system. During the pipe trip, the camera system was installed and lowered as the drill string was tripped to bottom. After the drill string was spaced out for reentry, the bit reentered Hole U1382A at 0348 h on 3 October. The top drive was then picked up, and the drill string was run to the casing shoe and spaced out for drilling. The sediment section was drilled without coring from 4547 to 4584 meters below rig floor (53–90 mbsf), at which point basement was contacted. Drilling parameters indicated a fairly hard formation from 90 to 93 mbsf, but drilling proceeded fairly quickly from 93 to 99 mbsf. From 99 to 110 mbsf, drilling parameters again were slow and consistent, indicating a hard formation. We decided to terminate the hole at 110 mbsf to allow 8 m of rathole below 10¾ inch casing that would extend to 102 mbsf. After the hole was conditioned, the bit was tripped above the casing shoe, the top drive was removed, and the drill string was tripped back to the rig floor. Before we could begin rigging up for running casing, we had to slip and cut 115 ft of drill line. We assembled 101.86 m of 10¾ inch casing that included a 14¾ inch outside diameter swellable packer one joint from the top and a casing hanger with a seal ring. We attached the casing running tool, lowered the entire casing string to the seafloor, and reentered Hole U1382A at 1355 h on 4 October. The casing was lowered smoothly into the hole until the last couple of meters, when we had to circulate to help clear the way so it could fully land. After the casing string was fully landed and latched, we cemented it in place with 20 bbl of cement blended with lost-circulation material (Cello-Flake). The cement displacement calculation was made to leave ~15 m of cement inside the casing above the casing shoe. Once we released the casing running tool from the casing hanger (1712 h on 4 October), we pumped seawater through the drill string to clean it of any remaining cement. Before we retrieved the casing running tool, we performed a 30 min survey of the Hole 395A reentry system (50 m to the west). The casing running tool arrived back on the rig floor at 0200 h on 5 October.

Our next step was RCB coring, so we assembled a new C-7 RCB bit (with center bit) with a three-stand BHA and lowered it to the seafloor. A break in tripping pipe occurred around 1030 h to install the camera system, but the system was quickly retrieved when the subsea camera did not work. The pipe trip continued for another hour and was halted again to install the repaired camera system. At 1330 h the drill string was spaced out for reentry, and Hole U1382A was quickly reentered at 1337 h. The bit was carefully run into the hole, and cement was encountered 14 m above the casing shoe (1 m below the expected 15 m). The top drive was then picked up, and the cement was drilled from 88 mbsf to just below the casing shoe that had been positioned at 102 mbsf. We circulated mud to clean the hole, recovered the center bit by wireline, dropped an RCB core barrel, and RCB coring began. The first core on deck, Core 336-U1382A-2R, arrived at 2245 h on 5 October. Coring continued through Core 336-U1382A-12R, which was on board at 2320 h on 7 October. We cored 100 m of section from 110 to 210 mbsf and recovered 31.8 m (32%; Table T2). After coring was completed, five wiper trips were made from total depth to the casing shoe and back to total depth. The first three trips revealed tight spots and circulation problems. The fourth and fifth trips were made with no evidence of drag or circulation problems, and no fill was found at the bottom of the hole. After hole cleaning and conditioning were completed, the drill string was tripped from the hole, clearing the seafloor at 0729 h on 8 October.

After the bit was back on the rig floor and before logging began, we assembled a stand of 6¾ inch perforated and coated drill collars for the lowermost portion of the CORK installation. We wanted to make up the drill collars before assembling the CORK to make it easier and more efficient to paint with epoxy prior to being deployed. Next, we assembled a logging BHA with a logging bit and the drill string packer, lowered it 64 m into Hole U1382A, and began deploying the logging tools. Logging proceeded with a modified triple combination tool string, with the DEBI-t on the bottom of the string (see **"Downhole logging"**). Log data were collected while the string was lowered to the bottom of the hole. However, while logging upward, the power failed ~20 m below the casing. The tool string was pulled to the surface, and the problem was found to be in the cablehead. The cablehead was reterminated, and we decided to run the FMS-sonic tool string next. After two successful passes, the lower portion of the FMS (calipers) would not enter the logging bit. After 2 h of working the string up and down, opening and closing the calipers, and pumping seawater, the entire tool string was able to pass through the logging bit; when it was recovered, one of the caliper arms had been damaged. We then spaced out the drill string for the hydrologic (packer) flow test and began attempting to inflate the packer. We made four attempts to set the packer inside the 10¾ inch casing; however, each time, high vessel heave (3 m) caused the packer to deflate, so the experiment was terminated. Before pulling out of the hole and installing the CORK, we lowered the entire BHA (including the deflated packer) until the logging bit reached the bottom of the hole to check that the hole was still open to full depth. We did not encounter any problem intervals and found only ~1.5 m of fill. The drill string was recovered, and the bit was back on board at 1328 h on 10 October. Before we could begin our next operation, we had to slip and cut 115 ft of drill line. We started assembling the CORK at 1500 h on 10 October. Details of the CORK are shown in Figures **F1** and **F2** and Tables **T3** and **T4.**

The preassembled 6¾ inch coated, painted, and perforated drill collar stand was picked up and run through the rotary table. Epoxy paint was used to touch up rust marks, and 10% ethanol was used to wipe grease from all exposed steel between the bottom of the casing and the top of the combination packer. After a crossover was installed, we attached 15.35 m of 5½ inch coated and perforated casing. Miniscreens were attached to the outside of the lowermost perforated 5½ inch casing joint. The lowermost four miniscreens included one titanium microbiology screen (connected to a Tefzel umbilical) and three stainless steel miniscreens for chemistry (two connected to ⅛ inch stainless umbilicals and one attached to a ¼ inch umbilical). The next set of four miniscreens, including a second titanium microbiology screen (connected to a Tefzel umbilical) and three stainless steel miniscreens for chemistry (one connected to a ⅛ inch stainless umbilical and two attached to ¼ inch umbilicals), was placed just above the first set of miniscreens. The stainless steel miniscreen for pressure (connected to a ¼ inch stainless umbilical) was strapped to the casing immediately above the second set of miniscreens. Crossovers to the 4½ inch fiberglass casing were installed, and then 44.25 m of 4½ inch fiberglass casing was made up. Umbilicals from the miniscreens and plastic Kwik-zip centralizers were installed on the outside of the casing as it was run. Next to be installed was a crossover from the fiberglass casing to the landing seat for the instrument string, followed by the joint with the swellable and inflatable packers. Umbilicals were terminated and connected to the bottom and top of the combination packer. Above the packers, ~91.01 m of uncoated and unperforated 4½ inch steel casing was run, followed by the CORK head. All pressure and sampling lines were connected to the bottom of the CORK. It took us 10 h to complete assembly, and the bottom of the CORK string extends to 188.7 mbsf.

Our next step was to assemble and install the OsmoSampler string into the CORK at the rig floor (see **"CORK observatory"**). Modifications were made before and during installation (thicker springs were installed, and parts were ground off of the latching mechanisms so they would stick out further) so that it would latch into the CORK head; however, these modifications did not work. The CORK head was submerged for 10 min to clear the pressure line of air, and then the CORK head was raised through the moonpool. A fast-flow OsmoSampler system was attached, and all of the unused valves were closed. The used valves include one pressure valve and a ⅛ inch chemistry line attached to the fast-flow OsmoSampler (see **"CORK observatory"**). The CORK was then lowered to ~100 m. The camera system was test fit over the CORK, and at 0630 h on 11 October, we began lowering the CORK package to the seafloor. The camera system was installed, and Hole U1382A was reentered for the last time at 1630 h on 11 October.

After carefully lowering the CORK into the hole, we landed the CORK at 1820 h on 11 October. The packer was inflated (to 1400 psi, which then bled off to ~1280–1300 psi), and the camera was pulled to the surface. Next, the remotely operated vehicle (ROV) platform was assembled and rigged up with the ROV deployment tool attached below the camera system and then lowered back to the seafloor.

The platform was released over the CORK at 0055 h on 12 October. The camera system was retrieved and after the ROV deployment system was removed, the camera was lowered back to the bottom to observe the final step of installing the Hole U1382A CORK—releasing the running tool from the CORK. This was successfully released at 0425 h on 12 October. The drill string with the CORK running tool was recovered back on board at 1145 h, ending Hole U1382A.

CORK observatory

Hole U1382A was cased through the sediment section (~90 mbsf) with 10¾ inch casing to 102 mbsf (see **"Operations,"** Fig. **F1**). The casing was cemented in place with cement that included Cello-Flake lost-circulation material. The cement extended 14 m uphole from the casing shoe inside the casing. Below the casing (1 m), the cement reached 103 mbsf. The hole was then RCB cored to 210 mbsf. Hole instabilities caused fill in the deepest ~1.5 m of the hole, based on a depth check with the logging bit after the aborted packer operations (see **"Packer experiments"**).

On the basis of drilling rate and core recovery, the screens and downhole instrument string targeted a zone centered at 161 mbsf (Fig. **F1**). Only one zone was targeted in this CORK. Because of the need to keep the CORK in tension, heavy, perforated, resin-coated drill collars were used at the bottom of the CORK assembly. The monitoring section of the CORK comprises (from the bottom up) a bullnose that is not restricted (terminates at a depth of 188.7 mbsf), six perforated 6 inch diameter drill collars, a crossover, a 15 m long section of perforated 5½ inch diameter casing, a crossover to fiberglass, five nonslotted fiberglass casings, a crossover, a landing seat (3⅜ inch), and a combination packer (inflatable and swellable) that was set in casing with its base at 101.4 mbsf (see Figs. **F1, F2;** Table **T3**).

All steel portions are coated with either Xylan, TK-34XT, or Amerlock to reduce reactivity (**Edwards et al.,** 2012, **Orcutt et al.,** 2012). However, due to handling operations, some steel was exposed. The bullnose and drill collars were connected, painted with an epoxy, and hung in the derrick several days prior to use. As these sections were lowered through the moonpool, they were wiped with 10% ethanol and painted with a fast-drying epoxy paint (Alocit 28) that also dries in water. The perforated 5½ inch casing sections were connected one at time, cleaned, and painted as they were lowered past the moonpool. Above the combination packer is more steel casing, which was untreated because none of this section is exposed to the formation of interest.

Umbilicals with internal stainless steel or Tefzel tubing were strapped to the outside of the casing and connected to miniscreens located at ~159–161.6 mbsf (see Fig. **F1;** Table **T3**). Nine miniscreens were deployed: two were attached to ½ inch diameter Tefzel tubing, one was attached to ¼ inch stainless steel tubing for pressure, and six were attached to stainless steel tubing bundles for geochemistry (three with ⅛ inch diameter and three with ¼ inch diameter). An additional ½ inch diameter stainless steel tube was used to inflate the packer, which has a check valve that opens at 25 psi (172 kPa).

The wellhead is a standard lateral CORK (L-CORK); however, the 4 inch diameter ball valve was removed and inspected. No visible cracks were evident, but it was replaced by a steel cap.

Downhole samplers and experiments

The downhole tool string consists of six different OsmoSampler packages, a dissolved oxygen sensor and recorder, two miniature temperature recorders, sinker bars, sealing plugs, and interspersed sections of ⅜ inch (0.95 cm) Spectra rope (Table **T4**). Complete details of this deployment are provided in **Edwards et al.** (2012), but a summary is provided here for completeness. The general features of OsmoSamplers are summarized in detail in Wheat et al. (2011).

In brief, OsmoSampler packages consist of a series of small-bore tubing, osmotic pumps, and in some cases microbial substrate materials (Flow-through Osmo Colonization System [FLOCS]; Orcutt et al., 2010, 2011). Each package includes a ½ inch (1.27 cm) diameter stainless steel strength member and stainless steel couplers to attach to other packages, line, sinker bars, or sealing plugs. All of the pump parts, excluding the membranes and O-rings, are made from polyvinyl chloride (PVC). Membranes were purchased from Alzet (2ML1), and O-rings are silicon based. Sample tubing is 1⁄16 inch diameter copper or Teflon with an inner diameter of ~1.19 mm and a length of 1000 ft (304 m). This tubing is spooled onto rods such that the rod and tubing fit within the inner diameter of a protective tube of clear PVC. The OsmoSampler packages were made with an outer diameter of 2⅞ inches (7.30 cm) in order to fit within the confines of the borehole, which was constrained by the inner diameter of the landing seat that isolates the monitoring interval inside the 4½ inch casing (tapered gravity seals).

Six types of OsmoSampler packages were deployed: standard, gas, acid addition, BioOsmoSampling System (BOSS), enrichment, and microbiology (MBIO) (Wheat et al., 2011). The standard package consists of three Teflon sample coils that are connected in series and open on one end, with an eight-membrane pump attached to the other end. Similarly, the gas sampler has three copper sample coils and a single eight-membrane pump. The acid-addition package is a standard package with two additional Teflon coils and an additional one-membrane pump at the intake. This pump draws borehole fluids into one coil while expelling saturated salt from the pump into the other coil filled with dilute subboiled HCl (20 mL 6N HCl in 500 mL of deionized distilled [18.2 MΩ] water). This acid-filled coil is attached to a T-connector, with the other T-positions connected to a short inlet to sample borehole fluids and to the intake of the equivalent of a standard OsmoSampler package. The BOSS package is identical to the acid-addition package, except that a solution of 2 mL of saturated $HgCl_2$ in 75% RNAlater (Ambion) replaces the dilute acid solution. The enrichment package also has the same configuration, but a solution of 1.2 mM nitrate in sterile seawater replaces the dilute acid solution, and a FLOCS microbial colonization experiment (Orcutt et al. 2011, see below) is connected to the T-connector that leads to the standard package. Fluids flow through two FLOCS columns before reaching the first Teflon sample coil. Attached to the FLOCS are a series of mineral chips that are exposed directly to the formation. The MBIO package consists of two standard packages, each with a FLOCS experiment attached to the intake. Only one FLOCS column is attached to each standard package, and mineral chips are included and exposed to the formation.

To investigate the activity and diversity of microorganisms in deep basement, microbial colonization experiments with defined mineral substrates are placed in the borehole to encourage in situ growth seeded by planktonic microorganisms in the borehole fluids. The concept, design, and demonstration of the FLOCS is discussed in detail elsewhere (Orcutt et al., 2010, 2011; Wheat et al., 2011) and is only briefly outlined here. The design of the FLOCS units used during this expedition is described in **Edwards et al.** (2012). The Hole U1382A CORK instrument string contains two FLOCS units: one in the enrichment OsmoSampler package and one in the MBIO package. The enrichment OsmoSampler FLOCS unit pulls formation fluids mixed with enrichment solution through two serially connected chambers containing cassettes of different substrates (basalts, olivine, siderite, sphalerite, chalcopyrite, pyrrhotite, hematite, pyrite, and glass wool and beads; for details see **Edwards et al.,** 2012). Separate osmotic pumps irrigate each chamber of the FLOCS unit in the MBIO package. One chamber contains basalts, olivine, siderite, sphalerite, chalcopyrite, pyrrhotite, and hematite; the other chamber contains larger volumes of glassy basalt and pyrite, plus glass wool and glass beads. All of the FLOCS have eight panels of rock chips (2–4 chips/panel, ~3 mm × 3 mm) mounted on one side of the FLOCS body to allow passive colonization on polished rock chips (as opposed to the slow advective pumped colonization in the chambers; see **Edwards et al.,** 2012, for details). The enrichment OsmoSampler FLOCS contains grids of barite, Hole 395A basalts, sphalerite, pyrite, goethite, and hematite. The MBIO OsmoSampler FLOCS contains grids of rhyolite, glassy basalt, Hole 395A basalt, olivine, chalcopyrite, pyrrhotite, and magnetite.

Attempts were made to minimize potential contamination of the FLOCS experiments. All rock substrates were autoclaved prior to use, and gloves were worn during assembly of the units. Prior to connection to the OsmoSampler package, the chambers of all FLOCS units were flushed with ethanol, distilled water, and filter-sterilized (0.2 µm mesh) Site 395 surface seawater, and the exterior of the FLOCS body with the mounted rock-chip panels was washed in a sterile Whirl-Pak bag with ethanol and kept closed in baked (450°C) aluminum foil wrappers. Assembled OsmoSampler packages sat for 1–2 days prior to deployment with the intake for the FLOCS chambers connected to a syringe of sterile filtered seawater. The rock-chip panels were exposed to minimally circulating air during this time (i.e., circulation was restricted to the few small openings in the OsmoSampler package sleeves).

Autonomous temperature and oxygen measurement probes were deployed at different locations along the instrument string (Table **T4**). One novel dissolved-oxygen probe (Aanderaa Optode 4330, thermal couplers, and digital recorders) was deployed. This recorder was programmed to measure dissolved oxygen and temperature once per day, with enough memory and battery life to record data for ~5 y. Excluding the temperature sensor in the dissolved-oxygen probe, two other temperature probes were deployed. These probes were purchased from Antares and Onset, and they fit within holes drilled into the plastic couplers in the OsmoSampler packages. Both probes provide a dynamic range that covers the expected temperatures (2°–30°C), but the Antares probes have greater sensitivity (see Fisher et al., 2005).

The remaining elements of the downhole tool string include the sinker bar, sealing plugs, and Spectra rope. A sinker bar (150 lb in water) was placed at the bottom of the string to help pull the string elements into the hole. A middle sinker bar (100 lb in water) was placed above the plug to help pull in the rope attached to the top plug. Below the top plug (1 m) is a smaller sinker bar (10 lb in water), with the joining Spectra rope covered by heavy-duty hydraulic hose.

The sinker bars and sealing plug are made of stainless steel and coated with Xylan. The Spectra rope (⅜ inch) allowed us to space out the OsmoSampler packages, sinker bars, and plugs to achieve the scientific goal of isolating and sampling specific horizons (see Fig. **F1**). In Table **T4** the exact lengths of Spectra rope are provided, as well as the expected length when taking into account a stretch of 1.5%. Note that some of the Spectra depths in the table exceed the length between seals. Additional Spectra rope was desired to ensure that the plugs would reach the sealing seats with 1–2 m of excess rope.

After the downhole OsmoSampler string was deployed, we deployed an OsmoSampler system attached to the CORK head, tapping into the targeted zone ⅛ inch diameter stainless steel umbilical line. This system consists of standard and MBIO OsmoSampler packages and a new fast-flow osmotic pump (for additional details see **Edwards et al.,** 2012). The fast-flow pump was attached in parallel to two 17 L reservoirs, with the intakes joined by a T-connector and directly attached to a modified handle system. The handle was connected to the valve for the ⅛ inch stainless steel umbilical line that samples the targeted zone. The narrow-diameter sample line was chosen to minimize the dead volume of the sample line and therefore the residence time of the fluid in the line. The fast-flow pump was modified to reduce the pumping rate to 150 mL/day (from 300 mL/day) by placing a Mylar sheet with five 1 inch diameter circular holes between the membrane and membrane support grid. This rate was chosen so that the 34 L freshwater reservoir would last 7.5 months, longer than the 6 month deployment time. This pump was placed in seawater and kept at 4°C for 4 days prior to deployment to verify the pumping rate and condition the membrane. The standard and MBIO packages, each with a 12-membrane pump and 1 Teflon sample coil, were attached (via T-connectors) to the intake tubing between the handle and the pump reservoir in order to subsample the formation fluids before entering the pump reservoir. The system was attached to the wellhead via a network of zip ties and rubber bands so that the package would remain on the CORK during deployment but allow recovery with an ROV.

Scientific and operational implications

The CORK plumbing was finished before the CORK head was landed on the moonpool doors. The CORK running tool was removed, exposing the top of the wellhead at the rig floor, and the bushings were installed to stabilize the CORK. The instrument string was deployed as designed. The top plug was deployed last but initially did not latch properly; it released with too little pull based on a gauge reading of several hundred pounds per square inch. After some modification it was decided that the top plug latch may be working. With the instrument string in place, the CORK running tool was secured to the CORK, and a new hydraulic hose was made to connect to the packer inflation line. The CORK was lowered ~5 m below the ship with all the valves open for 10 min. The CORK was then brought back to the ship, where the valves (including the pressure purge valves) were closed, the cap to the underwater mateable connector was removed, and the fast-flow OsmoSampler package was installed. During the deployment of the CORK, water surged up the casing because of the swell and the lowering of the casing, which suggests that the latch on the top plug was not latching as designed, allowing water to flow up the casing when the ship was descending in the trough. However, the plugs sealed the borehole when the ship ascended with the next wave. The CORK and ROV platform were landed, and the CORK running tool unlatched as planned.

Petrology, hard rock and sediment geochemistry, and structural geology

Basement was cored from 110 to 210 mbsf with an overall recovery of 32%. The recovered core material was divided into 8 major lithologic units comprising 17 subunits on the basis of changes in rock lithology, lava morphology, rock texture, and phenocryst occurrence (Fig. **F3;** Table **T5**). Major unit boundaries were defined by contacts between massive and pillowed flow and interlayered sedimentary units. The basalts comprise seven distinct chemical types—one highly plagioclase-olivine-phyric basalt and the rest aphyric (Fig. **F4**). Each basalt type consists of basaltic flows, pillow sequences, and perhaps intrusive doleritic massive flow units, ranging in thickness from 1.7 m (Unit 3) to 23.9 m (Unit 2). The sequence cored includes three massive aphyric units (Units 1, 3, and 8) and one porphyritic unit (Unit 6) lacking most contacts and glassy zones. The porphyritic basalts below the brecciated unit (Unit 5) correspond stratigraphically to basalts cored in Hole 395A. The aphyric pillow basalts in Units 2, 4, and 7 are petrologically similar, but the bulk rock chemical data indicate that Unit 7 may be derived from a parental magma with distinct Zr/Y and Ti/Zr ratios. Each major lava flow unit consists of several cooling units that are recognizable by glassy or variolitic margins or marked changes in groundmass grain size. Initial results from thin section studies reveal a wide range of grain sizes (glassy to medium grained) and textures (aphanitic to subophitic or intersertal). Basalts are either aphyric or plagioclase-olivine-phyric and have <3% vesicles. Phenocryst contents are as high as 25%, with plagioclase being more abundant than olivine. The extent of alteration ranges up to 20%, with clay (smectite, nontronite, and celadonite) being the most abundant secondary phase, followed by Fe oxyhydroxide and to a lesser extent zeolite and carbonate. Trace amounts of secondary pyrite were observed in thin sections.

The sedimentary breccia unit (Unit 5) in Cores 336-U1382A-8R and 9R (161.3–173.2 mbsf) features a variety of clasts, including plutonic and mantle rocks as well as basalts. The peridotites are weakly serpentinized harzburgites and lherzolites with a protogranular texture (Fig. **F4C**). The intensity of deformation of the gabbroic lithologies ranges from undeformed to mylonitic. Minor cataclastic deformation of the peridotites has led to the development of carbonate-filled vein networks, along which the rocks have been subjected to oxidative alteration, resulting in the breakdown of olivine to clay, oxide, and carbonate. The sedimentary breccia of Unit 5 consists of different lithologies, but the lack of contacts and likely disturbance during drilling preclude a determination of depth relationships between the numerous basaltic and gabbroic cobbles associated with sediment layers.

Lithologic units

Unit 1

Depth: 110.0–119.61 mbsf
Lithology: nonvesicular aphyric fine- to medium-grained basalt

This aphyric basalt unit is composed of four subunits that are distinguished mostly on the basis of groundmass grain size (contacts were not recovered). The basalts are nonvesicular (<1% vesicles) and are probably from the same cooling unit part of a massive flow. Alteration is generally slight to moderate at 5%–20%. The upper part of the unit (Subunits 1-1 and 1-2) is pervasively altered, whereas the lower part displays well-developed alteration halos and patches along veins and broken surfaces of the pieces (Fig. **F4A**). Within the grayish-brown halos, olivine microphenocrysts are extensively altered to an assemblage of secondary brown clay (smectite) and Fe oxyhydroxides (± iddingsite), whereas plagioclase and clinopyroxene remain unaltered. Minor carbonate, locally enriched in pieces (e.g., Section 336-U1382A-3R-2 [Piece 12]), and zeolite also fill voids in vugs and veins. In most recovered pieces, darker gray (freshest) basalt is surrounded by grayish-brown alteration halos, which develop due to the extensive oxidation of olivine microphenocrysts and interstitial glass (palagonitization) between fresh plagioclase laths as long as 4 mm (Fig. **F5**). Gray basalt displays occasional alteration of fresh olivine (<5%).

Unit 2

Depth: 119.61–143.45 mbsf
Lithology: sparsely vesicular aphyric cryptocrystalline pillow basalt

This aphyric basalt unit comprises 18 chilled margins (all defined as subunits) that were identified on the basis of glassy or variolitic margins (Fig. **F6**). The basalts are non to sparsely vesicular (0%–3% vesicles) with crypto- to microcrystalline groundmass. Recovered basalts are fresh (<1%) to slightly altered (up to 7%), with often spectacular blotchy alteration developing within the devitrified variolitic glass of pillow margins. Within alteration patches, euhedral olivine microcrysts are partly replaced by Fe-rich smectite (± iddingsite) in a slightly altered micro- to cryptocrystalline groundmass. Vesicles are filled with abundant Fe oxyhydroxides (± iddingsite), smectite (± celadonite), and minor zeolite (phillipsite) and carbonate. Some vesicles remain unfilled, with only a thin dark green (nontronite) coating. The grayish-brown alteration halos often have more unfilled or zeolite/carbonate-rich vesicles than the freshest dark gray groundmass, which contains mostly smectite-filled vesicles. In many cases, patchy alteration cannot be attributed to haloed veins on the basis of recovered specimens. Pervasive alteration is not common but rather develops as dark gray patches/blotches in grayish-brown alteration patches. The freshest dark gray microcrystalline groundmass may have faint and irregular (1 mm wide) dark brown alteration halos along veinlets as a result of Fe oxide staining.

Volcanic breccia (hyaloclastite) was recovered in two pieces (Sections 336-U1382A-4R-2 [Piece 4], Subunit 2-5; and 5R-1 [Piece 21], Subunit 2-13) (Fig. **F7**). Hyaloclastite in Subunit 2-5 is poorly sorted (clast size ranges from 1 to 4 mm) and is composed of 60% angular clasts of altered micro- to cryptocrystalline basalt (aphyric and nonvesicular) with moderate alteration (20%). The matrix (40%) is composed of subequal amounts of fine-grained to cryptocrystalline Fe oxyhydroxides (± iddingsite), smectite, and light brown clay of potential sedimentary origin. Zeolite and carbonate may also be associated with matrix filling and clast alteration (no X-ray diffraction [XRD] or thin section samples were taken of hyaloclastites). The hyaloclastite in Subunit 2-13 is also poorly sorted (clast size ranges from 1 to 10 mm) but has substantially higher clast abundance (85%). It is composed of angular clasts of aphyric nonvesicular basalt displaying extensive concentric alteration halos (average alteration = 60%). Fresh glass is partially devitrified. The matrix (15%) is composed of reddish-brown clay.

Unit 3

Depth: 143.45–145.17 mbsf
Lithology: nonvesicular aphyric fine- to medium-grained basalt

This unit of nonvesicular aphyric fine- to medium-grained massive basalt lacks any contacts and was defined as massive/basaltic flow. Alteration is patchy and restricted to grayish-brown alteration halos in which the groundmass is moderately altered (up to 15%) as a result of olivine and interstitial glass replacement by Fe-rich clay (iddingsite and smectite). The largest piece (Section 336-U1382A-6R-3 [Piece 1]) is 65 cm long and has centimeter-wide grayish-brown alteration halos along both sides.

Unit 4

Depth: 145.17–154.41 mbsf
Lithology: sparsely vesicular aphyric cryptocrystalline basalt

This unit of aphyric basalt is composed of eight subunits that were identified on the basis of glassy or variolitic chilled pillow margins. The basalts are generally sparsely vesicular (up to 5% vesicle abundance) with crypto- to microcrystalline groundmass. Recovered basalts are fresh (<1%) to slightly altered (up to 8%) with common blotchy alteration textures of devitrified variolitic glass in pillow margins. Alteration patches have mixed Fe oxyhydroxides and brown clays (smectite and iddingsite) replacing olivine and interstitial glass in the groundmass and filling vesicles. Subunit 4-1 is nonvesicular and pervasively altered (10% alteration). Aphyric fine-grained basalts (e.g., Subunit 4-3) generally develop patchy alteration patterns, whereas cryptocrystalline variolitic devitrified chilled margins develop dark brown blotches. Alteration intensity increases along radial veinlets near pillow margins.

Unit 5

Depth: 161.30–173.24 mbsf
Lithology: sedimentary breccia

This unit is composed of mixed lithologies of basalt (porphyritic and aphyric), sediment, breccia, plutonic rock (gabbro), and serpentinized lherzolite and harzburgite (Figs. F8, F9). Plutonic rocks and serpentinites are intercalated with pelagic nannofossil ooze having different degrees of induration and porphyritic volcanic rocks that were encountered above. Aphyric basalt at the top of Core 336-U1382A-8R is possibly from debris that fell into the hole during repeated wiper trips conducted after Core 7R was cut. The association of sediment with basalt, peridotite, and gabbroic rock is interpreted to result from mass wasting. As detailed below, eight main lithologies were identified in this unit:

1. Two short sections of soft sediment (Sections 336-U1382A-8R-2 and 8R-3) were recovered in Core 8R. These sections are composed of brownish-yellow calcareous nannofossil ooze that was disturbed by the drilling process. This unit contains volcanic clasts of grain size ranging from very fine to fine sand that could have been introduced during drilling.
2. Two intervals of more indurated calcareous nannofossil ooze, defined as chalk, were recovered in two pieces from Cores 8R and 9R (Sections 336-U1382A-8R-4 [Piece 2] and 9R-1 [Piece 18]). The piece from Core 9R was taken as a MBIO sample, and only a photograph is available for description. The chalk is light brown and contains volcanic clasts.
3. Two pieces of poorly sorted sedimentary breccia were recovered in Core 8R (Sections 336-U1382A-8R-1 [Piece 8] and 8R-4 [Piece 4]; Fig. F9). These pieces contain 30%–40% angular clasts ranging in size from 0.2 to 10 mm (fine sand to pebble). The clasts are composed of altered serpentinites (with foliated structures), possibly altered gabbroic rocks, and aphyric basalt. The matrix is composed of sedimentary light brown nannofossil clayey chalk.
4. Several pieces of coarse-grained porphyroclastic and mylonitic gabbros were recovered in Cores 8R and 9R. Sections 336-U1382A-8R-1 (Piece 4) and 8R-4 (Piece 3) are rounded pebbles of variably altered coarse- to medium-grained olivine gabbro. Altered olivine shows a foliated texture, whereas altered euhedral pyroxene is partly replaced by serpentine and chlorite. Section 336-U1382A-8R-1 (Piece 11) is characterized by completely altered olivine gabbro with pseudomorphic replacement to primary mineral assemblages by serpentine and chlorite. Section 336-U1382A-9R-1 (Piece 5) is the only piece of olivine gabbro ultramylonite recovered.
5. Several pieces of variably serpentinized harzburgite were recovered in Cores 8R and 9R (Sections 336-U1382A-8R-4 [Pieces 5 and 6], 8R-4 [Piece 9], 9R-1 [Piece 3], and 9R-1 [Pieces 12–17], Figs. F4C, F8). Contiguous pieces recovered in Section 9R-1 (Pieces 12–17) show common mesh texture of partly altered serpentine developed between/within coarse- and medium-grained olivine grains. Coarse- and medium-grained pyroxene shows moderate alteration. Olivine (50%–70% abundance) is partially to totally (30%–100% alteration) replaced by serpentine, which is locally

oxidized to Fe-rich clay assemblages in light green-brown alteration halos developed along thick (1–3 mm) carbonate (aragonite) veins (e.g., at 165.44 and 171.8 mbsf). Section 336-U1382A-9R-1 (Piece 12) is intruded by gabbroic plagioclase-rich veins, and another piece (Section 8R-4 [Piece 8]) is a fragment of dark green lherzolite having the least overall extent of serpentinization.

6. A single piece of serpentinized lherzolite (Section 336-U1382A-8R-4 [Piece 8]) recovered in Core 8R is composed of coarse- and medium-grained granular to porphyroclastic olivine (mode = 65%) and granular pyroxene (mode = 34%).
7. Several pieces of sparsely vesicular, aphyric cryptocrystalline to fine-grained basalt were recovered throughout Cores 8R and 9R (top: Section 336-U1382A-8R-1 [Piece 6]); bottom: Section 9R-1 [Piece 11]). Pieces have slightly to moderately altered cryptocrystalline groundmass with disseminated iron oxide–rich clay. As for other lithologies in Unit 5, no contact was recovered and the pieces are possibly derived from borehole wall breakouts from Unit 4 above.
8. Several pieces (some of them oriented) of highly porphyritic, sparsely to moderately vesicular (0%–10%) basalt were recovered throughout Cores 8R and 9R (Sections 336-U1382A-8R-1 [Piece 2] and 9R-2 [Piece 14]). These basalt pieces are generally similar to the plagioclase-olivine-phyric basalts encountered in Unit 6 below. The alteration is patchy, with euhedral olivine phenocrysts partly altered to iddingsite or whitish clay. Plagioclase phenocrysts are fresh. Vesicles are filled with abundant smectite (± celadonite), Fe oxyhydroxide (± iddingsite), and possibly minor zeolite and carbonate. The occurrence of porphyritic basalts in this unit may represent a basaltic flow—similar to or part of Unit 6 within Cores 8R and 9R.

Unit 6

Depth: 173.24–191.24 mbsf

Lithology: highly plagioclase-olivine-phyric fine-grained basalt

This unit of plagioclase-olivine-phyric basalt is composed of three subunits that are mostly distinguished from each other by groundmass grain size because no contacts were recovered (Fig. **F10**). The basalts are sparsely vesicular (<3% vesicles) and probably represent the same cooling unit of a massive flow. This unit is dominantly glomerophyric in texture and has microcrystalline to fine-grained groundmass. The groundmass is fine grained in Subunit 6-1 and microcrystalline with numerous microphenocrysts in Subunit 6-2. Interstitial glass is mostly devitrified and partly altered to palagonite. Euhedral plagioclase phenocryst abundance is ~20%, with crystal sizes ranging from <1 to 12 mm. Olivine phenocrysts are less abundant (mode = 3%) and smaller (0.5–4 mm). Fresh glomerocrysts of plagioclase show clinopyroxene and olivine inclusions. Euhedral olivine phenocrysts are partly altered (~40% alteration) to brown clay (smectite ± iddingsite) in the alteration patches, whereas plagioclase remains fresh or is merely tainted with Fe oxides.

Unit 7

Depth: 191.24–201.93 mbsf

Lithology: sparsely vesicular aphyric cryptocrystalline basalt

This unit of aphyric basalt is similar to Unit 4 and comprises seven subunits identified on basis of glassy or variolitic chilled pillow margins (Fig. **F11**). The basalts are generally sparsely vesicular (up to 5% vesicle abundance) with crypto- to microcrystalline groundmass. Recovered basalts are fresh (<1%) to moderately altered (up to 20%; Subunit 7-5), with a common blotchy alteration texture of devitrified variolitic glass in pillow margins. Alteration patches have mixed Fe oxyhydroxide and brown clay (smectite and iddingsite) and minor carbonate replacing olivine and interstitial glass in the groundmass and filling vesicles. The cryptocrystalline groundmass has numerous olivine microphenocrysts that are variably altered (average = ~60%).

Unit 8

Depth: 201.93–206.76 mbsf

Lithology: nonvesicular aphyric fine- to medium-grained basalt

This last unit is composed of aphyric fine- to medium-grained basalt, which suggests a massive flow unit at the bottom of Hole U1382A (Fig. **F12**). The basalts are slightly to moderately altered (6%–10% alteration) with common alteration halos and patches. Because of the lack of recovered contacts and the unknown thickness of this unit, it was not possible to assign a specific flow type. Therefore, this unit has been described as basaltic flow.

Igneous petrology

Aphyric fine- to medium-grained massive basalt (Units 1, 3, and 8)

The massive basalts in Units 1, 3, and 8 are aphyric, and the groundmass texture of all of the fine- to medium-grained basalts is intersertal to subophitic. The groundmass consists of 40%–47% tabular plagioclase (1–3 mm), 36%–43% anhedral clinopyroxene (0.3–1 mm), and ~2% small (<0.1 mm) equant to elongate to skeletal Fe-Ti oxide minerals. The morphology of the olivine crystals is equant, and some of them form in inclusions in plagioclase (Fig. F13A). Anhedral clinopyroxene crystals are intergrown with plagioclase. Primary sulfide minerals are observed in some samples, but they are very small (<0.1 mm) and rare. The microcrystalline groundmass is quench-textured mesostasis, composed mainly of sheaves of intergrown plagioclase and clinopyroxene that make up to 6%–10% of the rock.

Aphyric cryptocrystalline pillowed basalt (Units 2, 4, and 7)

The cryptocrystalline pillow basalt in Units 2, 4, and 7 is generally aphyric, and significant parts (~40%) of the samples contain olivine microphenocrysts (0.1–0.3 mm) in a glassy to fine-grained groundmass. Most of the olivine microphenocrysts are euhedral equant to elongate crystals. Although it has been almost completely replaced by alteration minerals in some samples (Sections 336-U1382A-3R-2 [Piece 11], 4R-3 [Piece 8], and 5R-1 [Piece 7]), olivine can be recognized from the pseudomorph outline (Fig. F13B).

The groundmass grain size ranges from glassy/cryptocrystalline to microcrystalline/fine grained, which corresponds to chilled margins and the interior of pillow lobes, respectively. The groundmass texture of glassy/cryptocrystalline basalt is aphanitic to spherulitic to variolitic and that of microcrystalline/fine-grained basalt is intersertal. Except for glassy pillow margins (described below), the groundmass generally consists of as much as 50% acicular and tabular plagioclase and up to 40% anhedral clinopyroxene intergrown with plagioclase. In all samples, plagioclase seems to be slightly more abundant than clinopyroxene, although the small grain size makes it very difficult to determine the exact proportions of plagioclase and clinopyroxene with an optical microscope. In addition to the plagioclase and clinopyroxene crystals, opaque Fe-Ti oxides commonly occur as minute (<10 µm) equant or elongate crystals making up 1%–2% of the groundmass. Rare primary sulfide grains are also very small (<10 µm).

The aphyric basalts from Units 2, 4, and 7 include ~17% pillow margins showing variolitic texture with or without fresh volcanic glass. In thin section observation, the groundmass of the pillow rims typically consists of three different parts from the outer to inner portions of the pillow (Fig. F6): (1) glassy to cryptocrystalline groundmass with skeletal olivine crystals and rare varioles, (2) a variolitic center with numerous varioles consisting of swirls of plagioclase needles and linked-chain olivine in a buff matrix lacking varioles, and (3) a microcrystalline part with faint variolitic texture and abundant sheaves of plagioclase needles. In these chilled pillow margins, the proportions of the groundmass phases cannot be accurately quantified due to the predominance of cryptocrystalline mesostasis.

Highly plagioclase-olivine(clinopyroxene)-phyric massive basalt (Unit 6)

The basalts from Unit 6 are characterized by the presence of ~20% euhedral to subhedral tabular plagioclase phenocrysts (up to 4 mm). Between 30% and 50% of the phenocrysts are glomerocrysts in which plagioclase crystals form single-phase glomerocrysts (Fig. F13C) or mixed-phase glomerocrysts with olivine or clinopyroxene (Fig. F13D). Olivine phenocrysts are also present throughout as euhedral to subhedral crystals. Most are smaller than 0.5 mm, although crystals as large as 2.5 mm were observed. On the other hand, clinopyroxene phenocrysts are relatively rare (generally <1%) in the basalt samples, although groundmass clinopyroxene crystals in coarser grained samples show more or less seriate grain-size variation and a range of shapes from granular to short prismatic to more equant, making it difficult to distinguish phenocrysts from the groundmass.

The fine-grained groundmass texture is intersertal, except for two glassy to cryptocrystalline chilled margins (Sections 336-U1382A-9R-3 [Piece 3] and 10R-3 [Piece 11]) that show hyalophitic texture in the glassy margin. In the fine-grained basalts, groundmass consists of ~35% lath-shaped plagioclase (as large as 4 mm), ~30% anhedral to subhedral clinopyroxene (as large as 0.8 mm), ~3% euhedral olivine, and 2% equant or elongate opaque Fe-Ti oxide (<0.1 mm). The chilled margin sample (Section 336-U1382A-10R-2 [Piece 10]) exhibits a variety of quench crystallization textures, ranging from spherulitic to plagioclase sheaves with or without plumose clinopyroxene. Figure F13E shows typical plagioclase spherulites surrounded by clear glass, partially replaced by clay, where acicular plagioclase forms the cores of the spherulites. As is the case in pillow margin samples, the proportions of the groundmass phases in the chilled margin sample of massive flow cannot be accurately quantified because of the predominance of glassy to cryptocrystalline mesostasis.

Biogenic/pelagic sediments and sedimentary breccia

Sediments were recovered between lava flows in three sections of Core 336-U1382A-8R, representing a total thickness of 63 cm. Smear slide identification of calcareous nannofossil assemblages is presented in a separate section (see "Micropaleontology").

Interval 336-U1382A-8R-2, 0–15.5 cm, is composed of brownish-yellow nannofossil ooze featuring highly disturbed internal structures induced by the drilling process. It contains clasts of volcanic rocks with grain sizes ranging from very fine to fine sand. The clasts are angular and poorly sorted and could have been introduced in the course of the drilling process.

Interval 336-U1382A-8R-3, 0–14.5 cm, comprises two parts. The upper part is similar to Section 8R-2, has a color of 7.5Y 5/6, and is highly disturbed. It seems to be a bit less consolidated than the lower part, which consists of yellowish (7.5Y 4/6) nannofossil ooze. The lower part contains volcanic clasts of very fine sand (black in color). This interval does not appear to be disturbed by drilling; however, no primary sedimentary structures were observed.

Interval 336-U1382A-8R-4, 6–27 cm, is composed of light brown (10Y 8/3) nannofossil ooze. It appears to be disturbed by drilling and contains volcanic clasts that are very fine to fine in grain size.

Interval 336-U1382A-8R-4, 32–42 cm (Piece 4) (Fig. **F9**), is a breccia composed of several types of clasts (volcanic and sedimentary in origin). The clasts are very poorly sorted and range in size from fine sand to pebble. The coarse clasts are very angular. The matrix seems to be composed of nannofossils and may contain very fine to fine sandy clasts. This breccia does not show any sedimentary structures such as grading or cross-bedding.

Plutonic and ultramafic rocks

Overview of gabbros, serpentinized harzburgites, and lherzolites in the sedimentary breccia unit

Clasts of gabbros and serpentinized harzburgites and lherzolites were recovered from the sedimentary breccia unit (Unit 5; 161.30–173.24 mbsf) in Hole U1382A. These rocks in the sedimentary breccia are variable in size and randomly distributed. The sedimentary breccia (Section 336-U1382A-8R-4 [Piece 4]) also includes small fragments of serpentinized peridotites and plagioclase grains from gabbroic rocks. Several serpentinized harzburgites and lherzolites feature carbonate (aragonite) veins and are intruded by gabbroic veins (Fig. **F14A, F14B**).

Gabbros

We obtained four gabbroic rocks from the sedimentary breccia unit. The lithology of the gabbroic rocks is mainly olivine gabbro of cobble size. The olivine gabbro cobbles display subangular, subrounded, and rounded shapes. On the basis of macroscopic observation, the olivine gabbros are generally altered (background alteration varies from 20% to 70%; see **"Core descriptions"**). Two olivine gabbros exhibit foliation or lineation, defined by plagioclase and olivine layers or elongation of mineral grains (Fig. **F15A**), indicating that the rock underwent crystal-plastic deformation. Other olivine gabbros reveal a granular texture of coarse-grained plagioclase and subhedral olivine and clinopyroxene.

In meso- and microscopic observation, three olivine gabbros (Sections 336-U1382A-8R-1 [Piece 4], 8R-4 [Piece 3], and 9R-1 [Piece 5]) (Fig. **F15**) consist of plagioclase (50%–80%), olivine (10%–20%), and clinopyroxene (5%–20%) with minor FeTi oxide. The gabbroic rocks have either porphyroclastic or mylonitic textures depending on the percentage of matrix versus porphyroclasts (e.g., Passchier and Trouw, 2005).

Two porphyroclastic olivine gabbros (Sections 336-U1382A-8R-1 [Piece 4] and 8R-4 [Piece 3]) (Fig. **F14C, F14D**) consist of plagioclase, olivine, and clinopyroxene with secondary albite, serpentine, and chlorite. Plagioclase occurs as coarse-grained porphyroclasts and in the fine-grained matrix. Olivine gabbros display foliation defined by the tails of plagioclase porphyroclasts and clinopyroxene and elongated olivine. Although no foliation in Section 336-U1382A-8R-4 (Piece 3) was seen during macroscopic observation, subordinate crystal-plastic deformation was observed in thin section (Sample 336-U1382A-8R-4 [Piece 3], Thin Section 19; Fig. **F15B**). Grain boundaries of plagioclase are often seriated from bulging (migration) of the grain boundaries. Fine neoblastic plagioclase grains in the matrix are polygonal and occur dominantly around the plagioclase porphyroclasts. They also display intracrystalline deformation such as undulose extinction and deformation twinning (Fig. **F15B**). The grain size of plagioclase in the matrix varies between 30 and 200 µm. The granular shape is typical of clinopyroxene grains (5–15 mm). Plagioclase is partly replaced by chlorite, prehnite, clinozoisite, and laumontite (Fig. **F15C**). Olivine is partly replaced by serpentine and tremolite. The boundary between olivine and plagioclase exhibits an unidentified clay mineral and a mixture of tremolite and chlorite.

The mylonitic texture of a single olivine gabbro (Section 336-U1382A-9R-1 [Piece 5]) (Fig. **F15A**) consists of plagioclase, clinopyroxene, and olivine with minor ilmenite. This sample shows well-developed foliation defined by both plagioclase-dominant and clinopyroxene-olivine layers. Plagioclase porphyroclasts (1–3 mm) show features of intracrystalline deformation such as undulose extinction, subgrain boundaries, subgrains, and deformation twinning (Fig. **F15A**). Plagioclase grains in the matrix range in size from 50 to 150 µm and are polygonal in shape. Matrix grains also have features of intracrystalline deformation such as undulose extinction and deformation twinning. Clinopyroxenes also have features of intracrystalline deformation including undulose extinction. The grain sizes of clinopyroxene and olivine vary between 200 and 500 µm. Olivine grains are equigranular in shape and do not reveal intracrystalline deformation.

The intensity of crystal-plastic deformation in each olivine gabbro was identified on the basis of macroscopic and microscopic observations: undeformed (0), weakly foliated (0.5–1), and mylonitic (4.5), respectively (see "Magmatic and crystal-plastic structures" in the "Methods" chapter [Expedition 336 Scientists, 2012]).

Serpentinized harzburgites and lherzolites

Nine partly serpentinized peridotites were retrieved from the sedimentary breccia unit, including seven harzburgites (Sections 336-U1382A-8R-4 [Piece 6], 8R-4 [Piece 9], 9R-1 [Piece 3], 9R-1 [Piece 13], 9R-1 [Piece 14A], 9R-1 [Piece 14B], 9R-1 [Piece 15], and 9R-1 [Piece 17]) and two lherzolites (Sections 8R-4 [Piece 8] and 9R-1 [Piece 12]). Most serpentinized peridotites are green, whereas others are dominated by tangerine color, largely the product of various degrees of serpentinization and weathering (background alteration varies from 30% to 90% based on macroscopic estimation). The serpentinized peridotites do not exhibit macroscopic evidence for deformation, although some display weak foliation defined by the slightly elongated pyroxene and spinel grains. Carbonate (mostly aragonite) veins of variable thickness cut the serpentinized peridotites (Fig. **F14A**). These carbonate veins show strings of rounded or elongate manganese oxide/oxyhydroxide grains in the center. One serpentinized peridotite was intruded by a gabbroic vein (Fig. **F14B**).

Thin section observations indicate that the protolith harzburgites consist of olivine (55%–70%), orthopyroxene (30%–44%), clinopyroxene (1%–5%), and spinel (1%) with minor plagioclase. Microstructures are characterized by coarse granular texture constituted by coarse olivine (1 to >5 mm) and medium-grained orthopyroxene (2–15 mm). Olivine grains show intracrystalline deformation, including subgrain boundaries and wavy extinction (Fig. **F16A**). Orthopyroxene grains are slightly bent and show wavy extinction. They also show exsolution lamellae of clinopyroxene. Serpentine replaced olivine and developed as networks of pale brown, dark brown, or black spinel grains with irregular shapes (Fig. **F16B**). Two serpentinized harzburgites are cut by narrow (<0.5 mm) and thick (1–4 mm) carbonate veins (Figs. **F16A, F16B, F16C, F14A;** Sections 336-U1382A-8R-4 [Piece 6] and 9R-1 [Piece 14B]). One serpentinized harzburgite shows two stages of carbonate veining: (1) cross-fibers sharply cutting through olivine and orthopyroxene grains, with some olivine and orthopyroxene shards preserved in the cross-fiber vein, and (2) reopening of the vein and precipitation of cracks and polygonal carbonate with manganese oxide. The polygonal carbonate grains include olivine and orthopyroxene shards originated from olivine and orthopyroxene in the adjacent harzburgite. Plagioclase grains are also present in the carbonate vein at the boundary between the cross-fiber and polygonal part of the vein (Fig. **F16D**).

The serpentinized lherzolite is characterized by coarse granular texture that consists dominantly of olivine (60%–68%), orthopyroxene (9%–20%), clinopyroxene (10%), spinel (1%), and plagioclase (1%) with serpentine, magnetite, and plagioclase as secondary minerals (Fig. **F14B**). A pervasive serpentine mesh network occupies 20%–30% of the rock. The microstructure of the serpentinized lherzolite is characterized by coarse granular olivine (0.4–10 mm) and orthopyroxene (2–8 mm). Olivine grains show features of intracrystalline deformation including subgrain boundaries. Some orthopyroxene grains are slightly bent and show wavy extinction with banding (Fig. **F16E**). The orthopyroxene also has exsolution lamellae of clinopyroxene (Fig. **F16E**). Pale brown and dark brown spinel grains have irregular shapes. Plagioclase not only occurs at the boundary between olivine grains (Fig. **F16F**) but also surrounding spinel grains. One serpentinized lherzolite is intruded by a gabbroic vein (~5 mm) that consists mainly of granular plagioclase (Fig. **F14**).

The intensity of crystal-plastic deformation in each serpentinized peridotite is mainly undeformed protogranular (0–0.5) based on macroscopic and microscopic observations (see "Magmatic and crystal-plastic structures" in the "Methods" chapter [Expedition 336 Scientists, 2012]).

Volcanic rock alteration

The basement volcanic rocks recovered from Hole U1382A are affected only by low-temperature alteration by seawater. Dark gray rocks are the most abundant and occur throughout the basaltic section. These rocks are the least altered, generally containing <3% by volume of secondary minerals such as dark green clays (saponite and celadonite), mixed clay and Fe oxyhydroxides (iddingsite), and minor zeolite (phillipsite) and carbonate (calcite) replacing olivine and filling pore space. Alteration of the basalts is variable and ranges from fresh to moderate, manifesting as replacement of groundmass and phenocrysts, vesicle filling, glassy margin replacement, and vein formation with adjacent alteration halos. Thin section estimation of groundmass alteration is generally consistent with results from visual core description, except in chilled pillow margins where microscopic observations suggest a lower extent of alteration, with both cryptocrystalline and olivine microphenocrysts often remaining unaltered (Table **T6**).

Throughout the following sections we refer to volume percentages of alteration types, breccias, vesicles, and veins. We assume that the surface areas of these features on the cut faces of the core, when converted to area percent, are equivalent to volume percent of the core, similar to modal analyses of a thin section. Veins, halos, and breccias observed in the archive half of the core were recorded in the respective vein/halo and breccia logs (see **"Alteration and metamorphism"** in the "Methods" chapter [Expedition 336 Scientists, 2012]). Figures **F17** and **F18** provide a summary of the calculated average (per core) of the abundance, volume, width, and mineralogy of vesicles, veins, and halos.

Secondary minerals

In the basaltic rocks from Hole U1382A, secondary minerals have developed as replacement of primary phenocrysts, disseminated in the groundmass, and as vesicle and vein filling. Identification of secondary minerals was primarily made in hand specimen on the basis of color, habit, and texture, with subsequent verification by thin section observations and XRD (Table **T6**). The most abundant secondary minerals in Hole U1382A are clay minerals, which are present in all types of alteration. Specific secondary clay minerals (e.g., saponite, nontronite, and celadonite) were characterized for a few examples during the logging of alteration and veins, but these minerals were generally referred to as "smectite" or "dark green clay." A distinction was made between minerals (carbonate and clay) associated with interflow sediments and minerals (carbonate, smectite, and iddingsite) that formed during basalt weathering. The identification of clay minerals remains tentative, however, pending further shore-based study.

Saponite is the dominant clay mineral and is present in all cores. In hand specimen, saponite occurs in black, dark green, or greenish-brown colors. When a reddish-brown to green color was observed, the mineral composition was recorded as mixed smectite–Fe oxyhydroxide. In thin section, saponite is characterized by pale brown to pale green color and mottled or fibrous form with variable pleochroism. Saponite generally evenly replaces groundmass and olivine (micro)phenocrysts, preserving the primary igneous textures. In the case of highly to extensively altered samples of pillow margin, saponite replacement is pervasive across mesostasis and groundmass microliths to form continuous mottled replacement or as blotches, revealing the original variolitic textures (Fig. **F6**). Commonly, saponite lines or fills vesicles (in association with other secondary minerals such as Fe oxyhydroxide, carbonate, and zeolite) and forms a lining along thin (0.1 mm) veins.

Celadonite is the only other clay mineral identified in hand specimen and thin section observations and occurs as bright green/blue in hand specimen. Celadonite is also present in all four types of alteration but is less abundant than saponite. In hand specimen, celadonite (mainly in vesicles) is green-blue, whereas in thin section it is bright green (see **"Vesicle filling"**). Celadonite was identified by XRD in a small fragment from pillow margin (Sample 336-U1382A-5R-1, 123–129 cm [Piece 7]) and in other slightly to moderately altered basalts (Table **T6**).

Fe oxyhydroxide is the next most abundant secondary phase, and it occurs either as a discrete phase or mixed with saponite and other smectitic clay phases. Fe oxyhydroxides are identified by their bright orange to red color and often stain other phases (e.g., plagioclase laths in groundmass). In many cases, the mixed assemblage of Fe oxyhydroxide and clays was described as "iddingsite," which has been previously reported in Hole 395A (Juteau et al., 1979). When present as replacement of microphenocrysts (mainly olivine) and groundmass, Fe oxyhydroxides (± iddingsite) are mixed with saponite and form intersertal hyalophitic texture. In veins and vesicles, Fe oxyhydroxides are bright orange to reddish brown and occur with or without intergrown clays. Staining of plagioclase phenocrysts and replacement of olivine with Fe oxyhydroxides are common features in the grayish-brown halos throughout all units recovered (Fig. **F19**).

Zeolite was found as a relatively common accessory mineral in vesicles, vugs, and vein filling, often associated with other secondary minerals (Fig. **F19**). Phillipsite and possibly chabazite were identified by XRD analysis in bulk sample powder (Table **T6**), although only phillipsite and minor stilbite were identified in altered basalts from Hole 395A (Juteau et al., 1979). In general, zeolite-filled vesicles and veins are more common in brown alteration halos of aphyric fine-grained and cryptocrystalline basalt encountered deeper in the section in Cores 336-U1382A-10R and 12R.

Carbonate is present as vug, vesicle, and vein filling and sometimes within olivine pseudomorphs (Fig. **F20**). Pure carbonate veins are rare in all basaltic units (e.g., Sample 336-U1382A-3R-4 [Piece 12]), but thin haloed veins often have a carbonate coating on the broken rock surfaces. As for zeolite-filled vesicles, carbonate (mostly calcite) was found essentially in grayish-brown alteration halos or pervasively altered sparsely vesicular basalts. XRD analysis of bulk rock powder did not unambiguously identify carbonate minerals. In brecciated Unit 5, large (up to 3 mm) carbonate (aragonite) veins were observed in altered serpentinized harzburgites (Fig. **F8**). Carbonate veins may form networks with clear crosscutting relationships, indicating different vein generations (see **"Plutonic and ultramafic rocks"**). In some cases, veins show spectacular aragonite druses in open voids. On the basis of thin section observation, the carbonate vein in Section 336-U1382A-9R-1 (Piece 14B), Thin Section 17, is associated with large opaque aggregates of Mn oxides (Fig. **F8**).

Ultratraces of secondary sulfide (pyrite) were identified only in thin section or under the binocular microscope. They occur as <10 µm crystals along cracks in plagioclase or disseminated in the groundmass of the fine-grained aphyric basalt of Unit 1. They also occur in vesicles and voids associated with other secondary minerals such as Fe oxyhydroxides (e.g., Section 336-U1382A-7R-1 [Piece 10], Thin Section 10) or zeolite (e.g., Section 12R-1 [Piece 21], Thin Section 26). Spherules of partially oxidized pyrite were also found in altered mesostasis (Section 336-U1382A-10R-2 [Piece 10], Thin Section 23) probably as replacement of primary magmatic sulfides. In Core 336-U1382A-12R, spherical secondary pyrite (<10 µm grain size) was identified along a thin saponite vein (Fig. **F21**).

Phenocryst alteration

Plagioclase

Plagioclase phenocrysts (Unit 6) are fresh. In the only transformations observed, plagioclases of aphyric basalt samples in the immediate vicinity of veinlets filled with smectite have been partially replaced by clay or tainted by Fe oxyhydroxides (Fig. **F21**).

Pyroxene

The augitic clinopyroxene remains essentially unaltered. When pyroxene occurs as microliths in microcrystalline groundmass, the extensive alteration (palagonitization) suggests pyroxene alteration (although the primary texture has been destroyed). Only small quantities of tiny smectite/celadonite lamellae have formed along grain boundaries around the pyroxenes of the porphyritic basalts.

Olivine

Olivine phenocrysts and microcrysts are the minerals most sensitive to alteration. In porphyritic and aphyric basalts, olivine is partially or completely replaced by reddish-brown iddingsite (a mixture of smectite and Fe oxyhydroxide) in the alteration halos (Fig. **F13**). In pervasively altered fine-grained basalts, olivine pseudomorphs are revealed as a result of their replacement by iddingsite (Fig. **F19**). In some cases, the initial shape of the mineral (skeletal or euhedral) is preserved as voids that can be partially filled by late-stage carbonate. In fresh dark gray basalts, olivine is partly replaced by saponite and possibly by celadonite.

Groundmass alteration

In the groundmass, plagioclase and clinopyroxene are quite fresh. Slight (5%) alteration of plagioclase and clinopyroxene was observed in the pervasively altered fine-grained basalt of Unit 1. In this alteration type, olivine is totally pseudomorphosed by iddingsite. Microscopic observation of fine-grained aphyric avesicular basalt of Unit 2 (e.g., Sample 336-U1382A-4R-3W, 39–42 cm, Thin Section 6) shows an overall alteration of 6%–8%, which is due to alteration of interstitial glass and olivine. Microscopic and XRD observations of microcrystalline sparsely plagioclase-olivine-phyric basalt (Unit 2) were undertaken to examine mineralogical changes with varying extents of alteration, from a fresh end-member (Sample 336-U1382A-5R-3W, 29–32 cm, Thin Section 8 [1.5% alteration]) to the most altered end-member (Sample 5R-1W, 32–36 cm, Thin Section 7 [10% alteration]). Results suggest that olivine is extensively altered and replaced by iddingsite (i.e., olivine was barely identified by XRD), whereas zeolite fills vesicles (also tentatively identified as chabazite by XRD). Plagioclase remains unaltered in both end-members.

Glass and chilled margins

Volcanic glass is generally devitrified in the groundmass of basalt. Chilled margins often show advanced palagonitization, which develops as a blotchy alteration texture following the primary variolitic texture of the mesostasis. The more altered end-members are brownish and contain vugs and veins filled with clay minerals and carbonate. Microscopic investigation of blotchy alteration texture in Unit 2 (Fig. **F6**) allows identification of several domains (see **"Aphyric cryptocrystalline pillowed basalt (Units 2, 4, and 7)"**) that are generally similar to the alteration of variolitic texture reported in Hole 395A (Natland, 1979).

In several glassy pillow margins, olivine is remarkably fresh. In Sample 336-U1382A-7R-2W, 70–73 cm, Thin Section 11, olivine occurs as euhedral to elongated skeletal microcrysts (referred to as "linked-chain morphology"; Donaldson, 1976) in cryptocrystalline groundmass. Glassy margins developing into spherulitic, mottled mesostasis also remain fresh. Note that the single thin section available for fresh glass alteration texture observation lacks microtubule textures that are considered to have formed through biological process (Fisk et al., 1998). XRD measurement of one altered pillow margin (Section 336-U1382A-5R-1 [Piece 22]) reveals significant replacement of the groundmass by zeolite (phillipsite) and celadonitic clay (Table T6).

Vesicle filling

The following filling associations were found in the vesicles: (1) Fe-rich dark green smectite (nontronite and smectite); (2) reddish-brown iddingsite generally logged as mixed Fe oxyhydroxides and smectite assemblages; (3) zeolite, mainly phillipsite; and (4) carbonate, in association with other major minerals. No trend with depth was found, but dark green clay (saponite and celadonite) mixed with variable proportions of Fe oxyhydroxides forms the vast majority of vesicle filling materials. Zeolite and carbonate may also fill vesicles, in particular within dark brown halos. Many pervasively altered basalts have (remarkably) unfilled vesicles or lack saponite enrichment, which suggests different stages of vesicle filling during rock alteration. In rare cases, pyrite was found coating the interior of vesicles or as euhedral crystals with other secondary minerals. An example of composite mineral filling of vesicles is illustrated in Figure F20, which shows (1) a mixed carbonate-iddingsite vesicle (Section 336-U1382A-7R-1 [Piece 14], Thin Section 10), (2) a pure carbonate vesicle (Section 9R-3 [Piece 3], Thin Section 22), (3) a mixed iddingsite-smectite vesicle (Section 4R-3 [Piece 9], Thin Section 6), and (4) mixed Fe oxyhydroxide and smectite vesicles (Section 4R-3 [Piece 9], Thin Section 6).

Veins and halos

The following filling associations were found in the veins: (1) Fe-rich dark green smectite (nontronite and smectite); (2) reddish-brown iddingsite, generally logged as mixed Fe oxyhydroxides and smectite assemblages; (3) zeolite, mainly phillipsite; (4) carbonate, in association with other major minerals; and (5) clays, possibly from interpillow sediment filling. Approximately 250 veins, including 90 haloed veins, were logged during core description of Hole U1382A, and veins make up 0.3% by volume of core (Fig. F18). The volume percent of veins for each core was estimated by calculating the volume of veins relative to the volume of the core recovered. We also logged ~170 halos in both pillow lava and massive flows that have highly variable thicknesses and are not always clearly associated with a vein. For this reason, we logged nonveined halos as having 0 mm vein thickness. Both veins (with or without halos) and nonveined halos were logged for the total vein count, which gives an estimation of the minimum and maximum vein abundance per core. Using this approach, we estimated that the recovered section in Hole U1382A has between 13 and 20 veins/m. The upper estimate for this hole is lower than for sections of upper volcanic basement from other holes (e.g., 27 veins/m in Ocean Drilling Program [ODP] Hole 896A, 24 veins/m in ODP Hole 801C, and 31 veins/m in Hole DSDP 504B; Alt et al., 1996; Plank, Ludden, Escutia et al., 2000). Veins range in thickness from ~0.1 to ~1 mm, but vein thickness <0.2 mm is by far the most common. The orientations of the veins are often subhorizontal to oblique in the cut face of the core, but vertical veins are not uncommon. Mixed smectite and iddingsite (Fe oxyhydroxide) veins are the most abundant, with carbonate and zeolite being less abundant. A thin (0.1 mm) iddingsite vein in an aphyric avesicular fresh basalt from Unit 2 (Sample 336-U1382A-5R-3W, 29–32 cm, Thin Section 8) and a medium-grained aphyric basalt from Unit 8 (Sample 12R-3W, 35–38 cm, Thin Section 2) are illustrated in Figure F21. In most cases, only iddingsite veins are associated with dark brown alteration halos, although most thin veins lack alteration halos.

Grayish-brown alteration halos were identified in all units in Hole U1382A (Fig. F4). Brown halos are characterized by abundant Fe oxyhydroxides disseminated in the groundmass, staining smectite-filled pores, and replacing olivine. Celadonite-nontronite may also be present. A representative piece of microcrystalline aphyric avesicular basalt with alteration halos was investigated by thin section (Sample 336-U1382A-4R-3W, 34–37 cm, Thin Section 5). The margins are more altered (~20%) with abundant clay (smectite) replacement of olivine (60% alteration) and more rarely after clinopyroxene and plagioclase (<10%). Fe oxyhydroxides are also enriched throughout the groundmass (interstitial filling) and olivine pseudomorphs. Voids and vesicles are also extensively filled with iddingsite. The less altered gray core is devoid of iddingsite, and only olivine (10% alteration) is replaced by dark green smectite. These grayish-brown alteration halos are developed throughout the entire section recovered in Hole U1382A and reflect significant oxidative weathering conditions due to alteration by oxygenated seawater. Many aphyric cryptocrystalline basalts to glassy pillow margins have very thin (<1 mm) and irregular alteration halos (Fig. F21), reflecting the formation of an oxidizing alteration front extending from the open cracks into the rock.

Breccia/hyaloclastite

The glassy fragments in hyaloclastic breccias have concentric alteration rims surrounding fresh glass preserved in the central part of the fragments (Fig. F7). The breccia cement is mainly clay (± zeolite) and carbonate. Mixed sedimentary clay and Fe iddingsite/smectite assemblages as matrix filling are apparent in Section 336-U1382A-5R-1 (Piece 21). In all hyaloclastite recovered, glass from glassy pillow rims and glass shards are variably altered to smectite, forming concentric alteration fronts with external rims of Fe oxyhydroxide. The cement is commonly smectite, carbonate, and zeolite. XRD analysis of a glassy margin in Section 336-U1382A-5R-1 (Piece 22) confirms that zeolite is common in altered glass of hyaloclastite, which is typically a result of "palagonitization" (i.e., low-temperature alteration of basaltic glass by seawater; Honnorez, 1972).

Hard rock geochemistry

Concentrations of major element oxides and several trace elements were obtained by inductively coupled plasma–atomic emission spectroscopy (ICP-AES) for a total of 19 whole-rock samples from Hole U1382A, together with total carbon and nitrogen contents by carbon-hydrogen-nitrogen-sulfur (CHNS) analyzer and LOI (see **"Hard rock geochemistry"** in the "Methods" chapter [Expedition 336 Scientists, 2012] for analytical procedures and precisions). Analytical values of ICP-AES were normalized to 100%, with total Fe recalculated as Fe_2O_3 ($Fe_2O_3^T$). Results of the ICP-AES analysis, as well as LOI and total carbon and nitrogen content data, are presented in Table T7.

Effect of plagioclase accumulation

Downhole variations of selected major element concentrations and LOI are shown in Figure F22. Although many elements show no systematic downhole trends, significant variations in concentration were observed for some elements. The downhole changes in composition include an increase in Al_2O_3, CaO, and Sr and a decrease in $Fe_2O_3^T$, TiO_2, Cr, Sc, V, and Y, which are associated with the presence or absence of plagioclase phenocrysts (Table T7). The significant increase of CaO and Al_2O_3 in the highly plagioclase-phyric basalts from Units 5 and 6 can be explained by the accumulation of plagioclase (Fig. F23). Likewise, the enrichment of Sr in the porphyritic basalts can very likely be attributed to accumulation of calcic plagioclase (Fig. F23). In addition, the depletions of MgO, $Fe_2O_3^T$ and TiO_2 can reasonably be assumed to reflect dilution by plagioclase accumulation in the porphyritic basalts (Fig. F24). Because depletions of Cr, Sc, and V concentrations in the porphyritic basalts generally correlate with the depletion in $Fe_2O_3^T$ (Fig. F25), we suggest that the decrease in concentration of these elements is also likely related to the accumulation of plagioclase.

Differences in magmatic geochemical signatures

Zr/Y and Zr/Ti ratios are not affected by crystal fractionation and accumulation of minerals in magmatic rocks. Instead, these ratios are sensitive to variations in mantle composition or melting processes during the formation of primitive magmas. The concentrations of Zr and Y are plotted in Figure F26. In this figure, two separate trends, indicating different Zr/Y ratios, are recognizable and clearly correspond to Units 1–4 (units shallower than the sedimentary breccia unit) and 6–8 (units deeper than the sedimentary breccia unit). A similar separation into two trends can also be picked in a Zr versus TiO_2 plot (Fig. F26). These results imply that the shallower and deeper units were derived from different parental magmas. On the other hand, these elements correlate well within both the shallow and deep units, suggesting that each of the two units originated from the same parental magmas. The sedimentary breccia unit (Unit 5) separates the shallow from the deep units indicating a hiatus in the volcanic activity.

The geochemical features of Hole U1382A basalts described above are similar to those reported for Hole 395A basalts at corresponding depths. For example, the difference in chemistry between aphyric and porphyritic basalts, as well as shallower and deeper units, is also shown in the Hole 395A basalts (e.g., Bougault et al., 1979). The compositional ranges of each lithology and unit also generally overlap (Figs. F23, F24, F25). These results clearly show that, although the proportion of massive and pillowed basalt flows is slightly different between the two holes, basaltic lavas recovered from Holes U1382A and 395A are essentially the same. This finding is not unexpected because Hole U1382A is only 50 m from Hole 395A.

Geochemical changes during alteration

Downhole variations of LOI and total carbon content are shown for the different lithologic units in Figure F22. Interestingly, altered samples having relatively high LOI contents (up to 2.69 wt%) occur only in the shallower units, and LOI contents of the samples from the deeper units are <1.03 wt%. Almost all basalt samples have low total carbon contents of <0.5%, except the sample from the shallowest depth, which has a total carbon content of 0.62 wt%.

In order to evaluate the geochemical exchange during alteration, the average compositions of altered samples were compared with those of fresh (i.e., least altered) samples (Fig. F27). In this calculation, basalt samples having LOI contents of <1% were defined as the least altered samples and those having LOI contents of >1% were regarded as more extensively altered ones. Compared to the fresh samples, the altered basalts are slightly enriched in K_2O, Ba, and total carbon contents (Fig. F27). The enrichment in total carbon clearly reflects the presence of secondary carbonate minerals in the altered samples. The K_2O concentrations slightly correlate with LOI values (Fig. **F28**), suggesting that the presence of K-rich secondary minerals (probably celadonite and phillipsite) in the altered basalt samples is responsible for the K_2O enrichment. In addition to K_2O, Ba is correlated slightly with LOI, and there is also a weak correlation between Ba and K_2O (Fig. **F28**). It is thus likely that Ba is also contained in K-rich minerals as a trace component.

Slight depletion of Mg was also observed in the altered basalts (Fig. **F27**), but the MgO depletion is very small and thus less certain. It is, however, noteworthy that olivine microphenocrysts were selectively altered to Fe oxyhydroxide in several altered basalt samples. This finding may suggest selective dissolution of Mg from altered basalts. Thus, it is likely that selective alteration of olivine causes the depletion of Mg in bulk rock chemistry of altered basalt samples.

Sediment geochemistry

Sediment was recovered in Sections 336-U1382A-8R-2, 8R-3, and 8R-4. Carbonate concentration measurements by coulometry were conducted for a total of eight samples from these sections (Table **T8**). Samples were taken from the split working half of the core and from two interstitial water squeeze cakes.

Calcium carbonate contents range from 20.8 to 43.9 wt%. Inorganic carbon contents range from 2.49 to 5.27 wt%.

Micropaleontology

Several layers of interbasalt sediments were encountered in Core 336-U1382A-8R. Sediments comprise all of Sections 336-U1382A-8R-2 and 8R-3 and are calcareous nannofossil ooze. In Section 336-U1382A-8R-4, consolidated ooze occurs from 6 to 27 cm, and a polymictic breccia extends from 31 to 42 cm. Smear slides show abundant calcareous nannofossils throughout these sediments (Table **T9;** Figs. **F29, F30**).

The common to abundant species in the sediment sections are short-ranged *Discoaster quinqueramus* (NN11), in addition to longer ranging *Discoaster brouweri* (NN9–NN18) and *Discoaster variabilis* (NN9–NN16). The conjunction of *D. quinqueramus* and *D. brouweri* is assigned to the upper Miocene *Discoaster quinqueramus* Zone (NN11). The absence of *Amaurolithus* spp. or *Amaurolithus primus* may indicate Subzone NN11A, which has an approximate age bracket between 7.2 and 8.5 Ma, according to the Neogene nannofossil biostratigraphic zonation of Bown (1998; fig. 8.1, p. 227). More or less similar age data were assigned to basement at Site 395 (Melson, Rabinowitz, et al., 1979), which is located only 50 m east of Hole U1382A. Site 395 is in oceanic crust magnetized during magnetic Anomaly 4 (Shipboard Scientific Party, 1979), estimated to be ~8 Ma on the basis of the revised geologic timescale of Walker and Geissman (2009). The $^{40}Ar/^{39}Ar$ age dating from feldspars of one crustal core sample at Site 395 shows an age of 9.8 Ma ± 2.9 m.y. (Turner et al., 1979). The basal sediment at Site 395 belongs to the upper Miocene *Amaurolithus primus* Subzone (NN11B, Messinian) of the *Discoaster quinqueramus* Zone (Bukry, 1979; Bown, 1998).

The discoasters, which are the most abundant nannofossils in the sediments, are subtropical species and may indicate the climate of this region during deposition in the late Miocene.

Other microfossil groups, like foraminifers and radiolarians, are very rare (Table **T9**). All of the foraminifers observed are planktonic (*Globorotalia* spp. and others), and they are altered or mineralized (Fig. **F30**). The radiolarians are too fragmented or dissolved to identify species (Fig. **F30C**). Only a single dinoflagellate specimen was identified in one sample (Sample 336-U1382A-8R-4, 24–25 cm; Fig. **F30D**).

Microbiology

Microbiological hard rock and sediment samples were collected from every interval cored with the RCB in Hole U1382A. Roughly 11% (3.8 m total) of core recovered from Hole U1382A was taken as whole-round samples from the core splitting room and dedicated to microbiological analysis. The 46 hard rock microbiology samples and 2 sediment samples span a range of lithologic units, alteration states, and presence of chilled margins, and some contain at least one vein or fracture. Table **T10** provides a description of the collected samples, and Appendix Figures AF1–AF47 provide photographs of the whole-round samples taken (see the **"Appendix"**). Additionally, a few background contamination samples were collected for shore-based DNA analysis, including recovered plastic bags that held the fluorescent microsphere solutions in the core catcher, samples of the drilling mud from the mud pumps, scrapings of drilling mud from a recovered drill bit, and surface seawater injected into the drill pipe.

In accordance with protocols described in **"Microbiology"** in the "Methods" chapter (Expedition 336 Scientists, 2012), samples were selected in the core splitting room as quickly as possible after core recovery, following initial discussion with petrologists on sample representation and photographing the sample before it was removed from the core liner. When sample volume permitted, samples were preserved for shore-based DNA and RNA analysis, shore-based FISH and cell counting analysis, ship-based culturing and enrichment, shore-based isotopic analysis, and ship-based fluorescent microsphere analysis. Microspheres were used during all coring operations to help evaluate core contamination. Microsphere density was evaluated in all samples following iterative washing of the exterior of the whole-round samples with sterile seawater. Table **T10** summarizes the results of the microsphere contamination survey, listing whether microspheres were detected in the first or last of 3–4 total washes with sterilized seawater. Of the 46 hard rock samples collected from Hole U1382A, 14 had microspheres in the first wash but none in the final wash, 26 did not have any detectable microspheres in any wash, and 6 had microspheres in all washes. In the latter case, only one microsphere was observed on the filter in the final wash. For all samples with observed microspheres, the microspheres were always in an abundance of <10. Of the two sediment samples collected, neither had microspheres on the interior of the core, and only one had detectable microspheres in the exterior.

Several enrichment and cultivation experiments were started with rock samples collected from Hole U1382A (see **"Microbiology"** in the "Methods" chapter [Expedition 336 Scientists, 2012]). Carbon-fixation incubations were initiated with one sample of massive oxidized basalt from Sample 336-U1382A-3R-4-MBIOA and one sample of a glassy pillow basalt from Sample 336-U1382A-7R-2-MBIOB. Enrichments for carbon- and nitrogen-cycling (carbon fixation, methane oxidation, and nitrate reduction) microorganisms were conducted with basalt from Samples 336-U1382A-2R-1-MBIOC, 3R-1-MBIOA, 3R-3-MBIOA, 3R-4-MBIOA, 3R-4-MBIOB, 5R-2-MBIOF, 6R-1-MBIOC, 8R-4-MBIOD, and 11R-1-MBIOA. Enrichments for methanogens, sulfate reducers, sulfide oxidizers, and nitrate-reducing iron-oxidizing bacteria were conducted with rocks from several horizons: Samples 336-U1382A-3R-4-MBIOA, 5R-2-MBIOF, 7R-2-MBIOB, 8R-2-MBIOF, 8R-3-MBIOG, and 10R-1-MBIOA. Enrichments for heterotrophic metabolisms were conducted with materials from Samples 336-U1382A-3R-4-MBIOA, 7R-2-MBIOB, 8R-2-MBIOF, and 8R-3-MBIOG.

Deep UV (<250 nm) native fluorescence scanning of hard rock materials with the Deep Exploration Biosphere Investigative portable tool (DEBI-pt) did not yield usable data for most of the Hole U1382A materials because of technical issues associated with operating in a shipboard environment with a new instrument. The heave experienced by the ship translated to rocking of the sample, which was corrected by using a heavier sample stage that was more stable. A second issue was encountered when part of the *x*-axis motor control failed, requiring a new component to be fabricated in the shipboard machine shop. Following these modifications, one sample from Hole U1382A was successfully scanned to assess the distribution of microorganisms on the surface of the sample (Fig. **F31**). Scanning of a subsample of Sample 336-U1382A-10R-3-MBIOD (Fig. **AF43**) indicated that microorganisms were heterogeneously distributed across the surface. Based on published fluorescence cross sections for bacteria (Seaver et al., 1998), the bacterial biomass for this sample is estimated to be ~10^4 cells/cm^2. Signal intensities indicative of bacteria were generally associated with patches of iron oxides. DEBI-pt scanning also identified regions of the sample in which aluminosilicates contained higher quantities of calcium and potassium, suggesting alteration.

Physical properties

The igneous rock and sediment recovered from Hole U1382A were characterized for physical properties as described in the **"Methods"** chapter (Expedition 336 Scientists, 2012). All recovered cores were processed with the Whole-Round Multisensor Logger (WRMSL) for measurements of gamma ray attenuation (GRA) density and magnetic susceptibility. All basement rocks were analyzed for NGR total counts and potassium weight percentage. The short sections of sediment recovered in Core 336-U1382A-8R were not processed with the Natural Gamma Radiation Logger (NGRL) because the samples remaining after water and microbiological sampling were too small to produce representative data. All archive core halves were analyzed for color reflectance and point magnetic susceptibility (MSP) on the Section Half Multisensor Logger (SHMSL).

Twenty-three discrete cube-shaped samples were cut from the working core halves for *P*-wave compressional velocity and moisture and density (MAD) measurements. When the piece was oriented, *P*-wave measurements were taken along each axis.

Gamma ray attenuation bulk density

The WRMSL was used to measure magnetic susceptibility and bulk density on the whole-round cores. The GRA measurements are sensitive to gaps and cracks in the material, as well as to underfilled liners and unsaturated samples. The raw data from this instrument were filtered to remove underestimated data, as described in the **"Methods"** chapter (Expedition 336 Scientists, 2012). Hard rock cores generally have a smaller diameter (~58 mm) than the internal diameter of the core liner (66 mm). This discrepancy can be corrected by multiplying the system output by

$^{66}/_{58}$ = 1.138 (Jarrard and Kerneklian, 2007). MAD and GRA density measurements give similar values once this correction is done for hard rock sections (Fig. F32). The sediment core sections (336-U1382A-8R-2 and 8R-3), located between 162.59 and 163.08 mbsf, have lower GRA density (1.76 ± 0.05 g/cm^3) than the igneous sections (2.85 ± 0.17 g/cm^3). Data from sediment in Section 336-U1382B-8R-4 were not considered because the sediment did not adequately fill the liner.

Magnetic susceptibility

Magnetic susceptibility (MS) measurements of whole-round and archive core halves are summarized in Figure F33. The raw data obtained from the WRMSL were filtered using the same criteria as those for GRA filtering because both sensors are installed on the same track and have a similar range of detection. Magnetic susceptibility data were also corrected for the diameter of the core (58 mm for hard rock and 66 mm for sediment) based on the equation given by the manufacturer (see MS2 Magnetic Susceptibility System operation manual, **www.bartington.com/operation-manuals.html**). The correction factor applied was 1.012 for igneous sections and 0.687 for sediment sections. However, this measurement assumes that the core liner is filled and does not take into consideration the gaps between samples; because this assumption is rarely correct for hard rock cores, the values measured need to be considered as minimums.

The MSP sensor is installed on the SHMSL along with the color reflectance spectroscopy sensor, and MSP data were filtered using the same criteria as those for color reflectance, as explained in the "Methods" chapter (Expedition 336 Scientists, 2012). No correction is needed for MSP measurements. Both whole-round and point magnetic susceptibility measurements present similar peaks, with a maximum (MSP = 3257 × 10^{-5} SI; MS = 2388 × 10^{-5} SI) located in the first piece of Section 336-U1382A-6R-3 at ~144.6 mbsf in lithologic Unit 3, which corresponds to a massive lava flow. This aphyric medium-grained basalt piece is the longest piece recovered in Hole U1382A. A secondary maximum (MS = 2010 × 10^{-5} SI; MSP = 1939 × 10^{-5} SI) was found at ~117.4 mbsf, corresponding to Section 336-U1382A-3R-3, which presented the same main lithology in lithologic Subunit 1-4.

Natural gamma radiation

NGR and potassium concentration data obtained from the NGRL are summarized in Figure F34. The count time for each core section (2 h) was maximized to increase the resolution of the data obtained. The total counts per second (cps) represent all of the radioactive elements. Spectral data were recorded, and the counts per second for each channel indicate the abundance of a particular element. When these values are related to a standard with known composition, the concentration of the element in the core section can be calculated. The total counts from the whole rounds range from 0.18 to 3.22 cps once the background is subtracted (Fig. F34). The concentration of potassium was calculated by using GRA bulk density as the effective density for the corrections.

Shipboard ICP-AES potassium data have values similar to those from NGR data (Fig. F34), with only three outliers (located at 126.20, 153.85, and 172.52 mbsf). The difference between the registries is due to the NGR data being from an average of >46 cm of sample versus the discrete samples for ICP-AES data. The ICP-AES potassium concentration values are in the range of 0.07–0.26 wt%, with an average of 0.17 ± 0.05 wt%. Potassium concentrations range from <0.01 to 0.35 wt%, with an average of 0.16 ± 0.05 wt%. In general, the concentration of uranium in basalt detected by NGR is very small, and ^{40}K is the main contributor to the total counts. However, a strong enrichment in uranium was detected in Sections 336-U1382A-8R-4 and 9R-1, which have low concentrations of potassium (<0.1 wt%). The unusual composition in these sections is related to harzburgite (lithologic Subunit 5-5) that has undergone oxidative seawater alteration of olivine, resulting in U enrichment (e.g., Niu, 2004).

In most of the cases where there was core recovery, NGR potassium concentrations are similar to the values obtained by the HNGS logging tool (see Fig. F35). The trend of increasing gamma ray intensities found near the bottom of the hole by the logging tool is not reflected by the NGR data, probably because of the lack of core recovery from the deepest section of the hole.

Moisture and density

Results of measurements of bulk density, dry density, grain density, void ratio, and porosity on 23 discrete samples are presented in Table T11. These values were determined using Method C (see "Physical properties" in the "Methods" chapter [Expedition 336 Scientists, 2012]). Samples were chosen to be representative of the different lithologic units and, when possible, were taken in areas adjacent to thin section samples in order to identify possible correlations. The alteration percentages for the adjacent thin sections are indicated in Table T11; when not available, the alteration percentage values of the piece are indicated. These samples generally had smaller volumes because they were not taken from the center of the core but from the side opposite the thin section sample. No samples were taken from the sediment core sections because of drilling disturbance observed on these sections. The average bulk density from discrete samples is 2.87 ± 0.05 g/cm^3 (Fig. **F32**). This value is similar to the average GRA bulk density (2.85 ± 0.17 g/cm^3). Dry density values average 2.78 ± 0.06 g/cm^3, and grain densities average 2.95 ± 0.05 g/cm^3. The mean porosity is 4.05% ± 1.27%, and the void ratio averages 0.04 ± 0.01. Porosity values do not linearly correlate with the percentage of vesicles or alteration estimated visually in core and thin section descriptions (see **"Petrology, hard rock and sediment geochemistry, and structural geology"** for more detail).

Compressional *P*-wave velocity

Twenty-three discrete samples were used to determine the compressional *P*-wave velocity of the main lithologic units. *P*-wave velocities were measured along the three axes (x, y, and z) in oriented cube-shaped samples. In nonoriented samples, only x-axis velocities were measured. All samples were measured three times. Measurements were done as quickly as possible for each saturated sample to avoid desiccation, which can affect the measured *P*-wave velocity. A summary of these measurements is presented in Figure **F36.** *P*-wave velocity correlates well with bulk density determined by MAD measurements (Fig. **F37**).

The mean value for all of the samples and directions is 6199 ± 447 m/s. The mean *P*-wave velocity values do not show any major trend related to the percentage of alteration or vesicles present in the sample. *P*-wave velocities inversely correlate with porosity (Fig. **F37**). *P*-wave velocity measurements range from 5733 to 7380 m/s along the x-axis, with a mean of 6206 ± 442 m/s. Along the y-axis, measurements range from 5675 to 7436 m/s, with a mean value of 6182 ± 458 m/s. Along the z-axis, *P*-wave measurements range from 5756 to 7288 m/s, with a mean of 6207 ± 462 m/s. A summary of all averaged values for each sample is presented in Table **T11.**

Only the harzburgite sample from lithologic Subunit 5-5 (Sample 336-U1382A-9R-1W, 102–104 cm) seemed to present some anisotropy (standard deviation = 176 m/s) when *P*-wave tests were done on its three axes. The basalt with the highest *P*-wave velocity is Sample 336-U1382A-5R-3W, 29–30 cm, which corresponds to aphyric cryptocrystalline basalt from a pillow flow. Sample 336-U1382A-7R-1W, 123–125 cm, from the same lithology also has an elevated *P*-wave velocity.

Thermal conductivity

Twenty-three measurements were taken on archive pieces representative of each section longer than 6 cm (Table **T12;** Fig. **F38**). Most of the basalt samples have similar values (1.728 ± 0.077 W/[m·K]). Two samples, located at ~163.91 and ~171.73 mbsf, are peridotites and have markedly different thermal conductivity values (3.384 ± 0.3162 W/[m·K] and 3.386 ± 0.079 W/[m·K], respectively). The higher thermal conductivities of the peridotites are consistent with the olivine-rich nature of these rocks because olivine has a much higher thermal conductivity (5.1 W/[m·K]) (Clauser and Huenges, 1995) than plagioclase (a main constituent of basalt). The uneven distribution of samples in the recovered section is the result of the limited availability of samples of the right size. The thermal conductivity values recorded for Hole U1382A do not present an apparent trend with depth (Fig. **F38**).

Color reflectance spectroscopy

Color reflectance L* for Hole U1382A varies between 10.80% and 60.90%, with a mean of 36.06% ± 4.72% (Table **T13;** Fig. **F39**). In general, basalt reflectance values are homogeneous, without pronounced differences between cores (Fig. **F39**). The values of a* and b* close to zero reflect the dark color of the basalt. No obvious trends were detected downhole. Color reflectance was not measured in small pieces and fragments because of the lack of flat surfaces (see **"Physical properties"** in the "Methods" chapter [Expedition 336 Scientists, 2012]). The main variations in color parameters were observed in lithologic Unit 5 (161.30–173.24 mbsf) because of the more diverse nature of this unit. These variations are particularly easy to see in the tristimulus parameters (Fig. **F39**).

Downhole logging

Downhole logging measurements obtained from Hole U1382A include natural total and spectral gamma ray, temperature, density, electrical resistivity, electrical images, and deep UV (<250 nm)–induced fluorescence. An open-hole section of 105.61 m was logged with two tool strings (Figs. **F40, F41**) over a period of ~19.5 h. The borehole remained in good condition throughout logging, and no obvious tight spots were encountered in open hole.

Logging operations

Downhole logging of Hole U1382A started on 9 October 2011 at 0215 h (all times are ship local, UTC – 3 h) after RCB coring ended at a total depth of 210 m core depth below seafloor (CSF). A summary of logging operations is presented in Table **T14;** see **"Operations"** for full operational details on hole preparation for logging.

Two tool strings were deployed in Hole U1382A: (1) the AMC I and (2) the FMS-HNGS. The AMC I tool string included the logging equipment head-mud temperature (LEH-MT) tool (cablehead with temperature measurement), the Enhanced Digital Telemetry Cartridge (EDTC with total gamma ray measurement), the Hostile Environment Litho-Density Sonde (HLDS), the High-Resolution Laterolog Array (HRLA), the Lamont Multifunction Telemetry Module (MFTM), and the DEBI-t (see **"Downhole logging"** in the "Methods" chapter [Expedition 336 Scientists, 2012, for tool string details) (Fig. **F40**). The AMC I tool string was lowered into the borehole at 0317 h on 9 October. The wireline heave compensator (WHC) was optimized with the AMC I in casing at 4590.1 m wireline log depth below rig floor (WRF). The AMC I completed a downlog to a total depth of 4700 m WRF (~4 m above the bottom of the hole; note that we deliberately did not tag the bottom with the DEBI-t) and an uplog to 4620 m WRF (~20 m below the bottom of casing), where the tool string experienced a power short. Power was lost to the tool string, and the AMC I was brought back up to the surface. The AMC I tool string was rigged down by 1110 h.

The second tool string deployed was the adapted FMS tool string composed of the HNGS and FMS (Fig. **F41**). The FMS-HNGS tool string was lowered into the hole at 1221 h on 9 October and reached the bottom of the borehole (4703.1 m WRF) at 1517 h, following logging down from the seafloor. The FMS-HNGS tool string performed two successful passes of the hole, and following a short period of difficulty (2 h) in reentering the pipe, the tool string was returned to the surface and rigged down at 2153 h on 9 October, at which time logging operations in Hole U1382A were completed.

Data processing and quality assessment

The logging data were recorded on board the R/V *JOIDES Resolution* by Schlumberger and archived in Digital Log Interchange Standard (DLIS) format. Data were sent via satellite transfer to shore, processed, and transferred back to the ship for archiving in the shipboard database. Processing and data quality notes are given below. The DEBI-t data recorded to SD memory card (video and full systems and fluorescence data in binary format) were also sent via satellite for archiving; however, data conversion and depth matching of the DEBI-t to the other final depth-matched log data was done on board (see **"Downhole logging"** in the "Methods" chapter [Expedition 336 Scientists, 2012]).

Depth shifts were applied to the logging data by selecting a reference (base) log (usually the total gamma ray log from the run with the greatest vertical extent and no sudden changes in cable speed) and aligning features in equivalent logs from other tool string passes by eye. In the case of Hole U1382A, the base log was the gamma ray profile from Pass 2 of the FMS-HNGS tool string. The original logs were first shifted to the seafloor (4497 m WRF), which was determined by the step in gamma ray values. This depth did not differ greatly from the seafloor depth given by the drillers (3 m difference).

Proper depth shifting of wireline logging depths relative to core depths was essential to correlate the downhole logging data with all other measurements and observations made on core recovered from Hole U1382A. The seafloor was the only target that offered a potential wireline logging depth reference. However, note that data acquired through the seafloor resulted from logging through the BHA and casing, so data from this interval are of poor quality and highly attenuated and should only be used qualitatively. However, they are adequate to pick out the seafloor. The quality of wireline logging data was assessed by evaluating whether logged values are reasonable for the lithologies encountered and by checking consistency between different passes of the same tool. Specific details of the depth adjustments required to match logging runs/data are available in the logging processing notes in the log database for Hole U1382A (**iodp.ldeo.columbia.edu/DATA/**).

A wide (>30.5 cm) or irregular borehole affects most recordings, particularly tools like the HLDS (bulk density) that require decentralization and good contact with the borehole wall. The density log correlates well with the resistivity logs but is largely affected by hole conditions. Hole diameter was recorded by the hydraulic caliper on the HLDS tool (LCAL) and by the FMS calipers (C1 and C2). Both calipers show a highly variable hole with a diameter ranging from 26.6 to 47.95 cm (LCAL data). The main breakouts were observed at ~142–145, ~153–155, and ~162–163 m wireline log matched depth below seafloor (WMSF); however, only the uppermost breakout was out of the range of the FMS caliper arms (38.1 cm diameter). Good repeatability was observed between the downlog and uplog of the AMC I and the two passes of the FMS-HNGS, particularly for measurements of electrical resistivity, gamma ray, and density.

Bulk density (HLDS) data were recorded with a sampling rate of 197 measurements per minute (2.54 cm at 300 m/h), in addition to the standard sampling rate of 32 measurements per minute (15.24 cm at 300 m/h). The enhanced bulk density curve is the result of the Schlumberger enhanced processing technique performed on the MAXIS system on board the *JOIDES Resolution*. In normal processing, short-spaced data are smoothed to match long-spaced data (depth and resolution matched). In enhanced processing, the raw detail obtained from the short-spaced data is added to the standard compensated density (Flaum et al., 1987). In a situation where there is good contact between the HLDS pad and the borehole wall (low density correction), the results are improved because the short spacing has better vertical resolution (i.e., it has the capability to resolve thinner beds/units).

The FMS images are of good quality over the majority of the hole; the only images that should be treated with caution are those taken where the main borehole breakouts are located (see above), because the pad may not have maintained good contact with the borehole wall.

Preliminary results

Downhole logging measurements obtained from Hole U1382A include natural total and spectral gamma ray, temperature, density, electrical resistivity, and deep UV–induced fluorescence. The results are summarized below.

Electrical resistivity measurements

Five main electrical resistivity curves were obtained with the HRLA: RLA1–5 (shallower through deeper penetrating measurements). The HRLA reached a total depth of 194.99 m WMSF in the logged interval because it was situated immediately above the DEBI-t (Fig. **F40**). The RLA3, RLA4, and RLA5 measurements are the most reliable for lithologic interpretation because of their deeper investigation depths and are hence less influenced by drilling-induced features.

Hole U1382A is composed of several lithologic units, so the resistivity values are variable. RLA3 values range between 1.48 and 479.54 Ωm (averaging 38.36 Ωm), RLA4 values range between 1.68 and 731.18 Ωm (averaging 38.77 Ωm), and RLA5 values range between 2.26 and 774.97 Ωm (averaging 43.86 Ωm) (Fig. **F42**). Some of the highest resistivity values correlate to more massive units (e.g., at ~147 and ~165 m WMSF, which correspond to a massive fine-grained basalt horizon [lithologic Unit 4] and peridotite interval [lithologic Unit 5] in log Units IV and VIII, respectively). All resistivity curves show considerable variability throughout the hole (Fig. **F42**). However, there is a notable downhole contrast in resistivity, consistent across all resistivity curves, at ~143 and 163 m WMSF (log Units III and VII; see **"Log units"**) in lithologic Units 3 and 5, which relates to a more visibly conductive (from FMS images) sedimentary breccia that can be considered a rubble zone.

Density

Density ranges from 1.09 to 3.19 g/cm^3 (average value = 2.33 g/cm^3) in Hole U1382A (Fig. **F42**). A comparison between discrete physical properties samples and the downhole density log shows relatively good agreement (values measured on core average 2.87 ± 0.05 g/cm^3). Low density values correspond to intervals with larger borehole dimensions and sections that exhibit much lower resistivities (Fig. **F42**). Pronounced high density values correspond to two distinct horizons (log Units IV and VIII; see **"Log units"**) that relate to massive fine- to medium-grained aphyric basalt in lithologic Unit 3 and a peridotite interval in lithologic Unit 5.

Gamma ray measurements

Standard, computed, and individual spectral contributions from ^{40}K, ^{238}U, and ^{232}Th were part of the gamma ray measurements obtained in Hole U1382A with the HNGS and the EDTC (total gamma ray only) (see Table **T6** in the "Methods" chapter [Expedition 336 Scientists, 2012]). The total gamma ray measurements through the BHA (pipe down to ~60 mbsf) and casing show two main anomalies from the seafloor to ~99 m WMSF (where casing was set) (Figs. **F42, F35**). The open-hole gamma ray measurements cover a total of 85.88 m (AMC I) and 92.98 m (FMS-HNGS) downhole. The slightly shorter overall coverage of the gamma ray sondes compared with the DEBI-t and FMS is the result of the EDTC and HNGS being ~20 and ~14 m higher in the tool string, respectively (Figs. **F40, F41**).

Gamma ray measurements in basaltic oceanic crust are typically low (e.g., Bartetzko et al., 2001; Barr et al., 2002), and the lithologic units penetrated and logged in Hole U1382A follow this trend. Total spectral gamma ray (HSGR) values obtained in Hole U1382A average 5.87 gAPI, with a maximum of 23.83 gAPI. Potassium values are relatively low, with an average value of 0.21 wt% and a maximum of 0.53 wt% (Fig. **F42**). These values agree very well with NGR measured on the whole-round cores (0–0.35 wt%, average = 0.16 wt%; see **"Physical properties"**) and values obtained using geochemical analysis (0.07–0.26 wt%) (see **"Petrology, hard rock and sediment geochemistry, and structural geology"**). Uranium concentrations average 0.16 ppm and have a maximum value of 1.71 ppm. An elevation in uranium abundance together with a low concentration of potassium was observed at ~165 m WMSF, relating to an interval of peridotite (slightly serpentinized). The same trend was observed in the NGR data on Section 336-U1382-8R-4 (see **"Physical properties"**).

Thorium concentrations average 0.39 ppm and reach a maximum value of 2.47 ppm. The potassium, thorium, and uranium concentrations are all very low and sometimes negative, a phenomenon that is common in formations with low radioactivity (Bartetzko et al., 2001).

Comparison of gamma ray data collected in Holes U1382A (Expedition 336) and 395A (ODP Leg 174B) allows correlation between particular features in the data set (Fig. **F43**). Because Hole U1382A is 50 m west of Hole 395A, there are some lateral differences in the extent of some units and their depths below seafloor. However, very similar downhole variations in gamma ray intensity were observed.

Temperature

Temperature measurements taken using the LEH-MT cablehead temperature sensor have very little variability downhole (Fig. **F42**). These data should be used qualitatively because the cablehead was shown to measure temperature 2.75°C higher than the Modular Temperature tool (MTT) (and following tests, the MTT was shown to be the more accurate of the tools). The data presented here were corrected using this factor, but observed values are lower than expected (~2°C). However, it is possible that these data are not entirely reliable given the subsequent failure (power short) that we experienced in the cablehead during logging.

Fluorescence

There was no observable trend in fluorescence in the downlog (Fig. **F44**); the relative ratio of fluorescence from all bands appeared the same. Video taken during the AMC I logging operation indicated that this hole was much cleaner than the previous hole, corroborating the difference in spectral features observed in Hole U1382A. There were no observable flocs, and the wall appeared to be relatively dark, in contrast to the more oxidized nature of the borehole wall in Hole 395A.

The fluorescence data from Hole U1382A were markedly different from those of Hole 395A. The overall intensity of fluorescence in Hole U1382A was greater than that seen in Hole 395A, with the largest increase being observed in the 360 nm band. Additionally, the signal intensity is more uniform throughout Hole U1382A, with the exception of the 455 nm band, which shows an increase in intensity with depth. A "bump" in intensity of the 455 nm band was observed between 160 and 170 m WMSF (Fig. **F45**), which may be related to calcareous ooze described near this horizon. This band also appears to respond to borehole size variations based on caliper data because the regions with the noisiest information occur at depths where the borehole diameter varies most. The other significant difference is that the overall structure of the fluorescence spectra differs between the two holes. Furthermore, the 340 and 360 nm bands are more intense as a function of the spectra in Hole U1382A compared to Hole 395A.

Similar to Hole 395A, the fluorescence from the 300 and 320 nm channels shows no large-scale variation (Fig. **F46**). Additionally, the spectral structure does not correlate with the presence of large quantity of biomass. Because the hole was pumped/circulated for extended periods with surface seawater and periodic sepiolite mud sweeps, it is unclear at this time what portion of the detected signal is from the formation or from the surface water. Calibration work done on board the ship with drilling mud and surface seawater indicates that some of the signal may be related to the seawater, although there does not appear to be a large influence from the drilling mud.

Log units

Preliminary interpretation of the downhole log data divided Hole U1382A into a number of log units (Fig. **F42**). Log units were defined only below the casing (~99 m WMSF) in the open-hole section and were characterized using gamma ray, resistivity, and density.

Eleven log units were qualitatively identified in the open-hole section of Hole U1382A (Fig. **F42**):

- Log Unit I (~99–118 m WMSF) was defined using only gamma ray and resistivity. This unit shows relatively stable gamma ray values between 3 and 5 gAPI. There is a mild decreasing trend in gamma ray intensity from ~99 to 110 m WMSF, below which values become rather uniform. Resistivity values are variable at the top of this log unit; however, below ~110 m WMSF, a steady increasing trend was observed that is likely related to the borehole shape (and the transition from the end of the rathole into cored hole). This log unit correlates to lithologic Unit 1 and relates to massive, nonvesicular, aphyric fine- to medium-grained basalt with fractures.
- Log Unit II (~118–143 m WMSF) exhibits relatively constant gamma ray values, with values clustering around 6 gAPI. With the exception of a steep decrease in resistivity values at the very top of this log unit, resistivity very slightly increases with depth through this log unit. Density values are highly variable and relate to the highly fractured nature of this lithology. Log Unit II corresponds to lithologic Unit 2, a pile of aphyric cryptocrystalline pillow basalt with numerous glassy and fractured flow contacts.
- Log Unit III (~143–146 m WMSF) has considerably lower gamma ray intensities compared to log Unit

II. This unit also features the lowest density values measured in this hole and some of the lowest resistivity values. This interval likely represents a section of sediments and brecciated material (related to lithologic Unit 3 but not recovered). Additionally, the borehole is extremely enlarged in this region, and therefore this log unit could be viewed as a rubble zone. This interpretation is corroborated by the very high rate of penetration (3 m in 10 min) during drilling of lithologic Unit 3.

- Log Unit IV (~146–148 m WMSF) has consistently high density and resistivity values. Additionally, gamma ray intensities are marginally higher than in log Unit III. This log unit is correlated to a fine- to medium-grained aphyric basalt unit (lithologic Unit 3) recovered in Core 336-U1382A-6R.
- Log Unit V (~148–153 m WMSF) exhibits significantly lower resistivity values than those from log Unit IV; however, they are by no means low values. Gamma ray values increase downhole in this unit, which may relate to an increase in alteration. Density and resistivity values fluctuate greatly, but they follow the same trend (i.e., high resistivities correlate with high densities). The interval with lower densities and resistivities likely relates to fractures in the aphyric cryptocrystalline basalt pillow lava to which this log unit is correlated (lithologic Unit 4).
- Log Unit VI (153–163 m WMSF) shows a steady increase in resistivity downhole after very low values at the top. Density values vary highly, but a general increasing trend with depth was observed. Gamma ray intensities exhibit a decrease down to the middle section of this log unit. Values then start to increase slightly toward the base. The variable density values reflect both the fractured nature of the formation (pillow lava from lithologic Unit 4) and sections of enlarged borehole, where it is possible that good contact with the borehole was not always maintained.
- Log Unit VII (~163–165 m WMSF) exhibits a small increase in gamma ray intensity and a sharp decrease in density and resistivity. This zone relates to a very dark, conductive section (in the FMS images) and may relate to some interpillow sediments that were not recovered. Consistent with this interpretation is the fact that the interval was drilled in several minutes, without torquing of the drill string.
- Log Unit VIII (~165–167 m WMSF) displays the highest density values measured in Hole U1382A, along with some of the highest resistivity values. Gamma ray values are slightly higher than in log Unit VII, and higher uranium values and lower potassium values in this interval relate to a piece of mildly serpentinized peridotite in lithologic Unit 5. The high uranium-to-potassium ratios and densities of this rock type were also detected in the course of shipboard studies (see **"Physical properties"**).
- Log Unit IX (~167–169 m WMSF) has very similar gamma ray, resistivity, and density values as log Unit VII and likely relates to another section of sediments or matrix-supported breccia.
- Log Unit X (~169–189 m WMSF) exhibits consistently high density and resistivity values in the top two-thirds of the unit. Toward the base, resistivity values decrease and density values fluctuate more widely. Gamma ray generally increases with depth. From FMS images it is possible to see a gradual change from the highly resistive material containing fractures at the top of the unit to a more conductive, fractured, blocky formation toward the base. This log unit primarily relates to a massive flow of highly plagioclase-olivine-phyric fine-grained basalt (lithologic Unit 6).
- Log Unit XI (~189–195 m WMSF) is defined primarily by a considerable drop in resistivity at the top. Gamma ray values increase downhole from the top of this unit, with total gamma ray values reaching ~9 gAPI. This log unit, and the sudden drop in resistivity, marks the change from a more massive flow to pillow lavas (the transition from lithologic Unit 6 to Unit 7).

Electrical images

In Hole U1382A, we also acquired FMS electrical resistivity images (Figs. **F47**, **F48**). The quality of electrical resistivity image measurements depends on close contact between the measuring pads on the tool and the borehole wall. The FMS borehole images collected in Hole U1382A are of good quality; however, sections of the borehole were not in gauge, and image quality is diminished in these sections (~142–145, ~153–155, and ~162–163 m WMSF).

FMS imagery is an essential data set and becomes invaluable when core recovery is low. In Hole U1382A, overall core recovery was 32%. Using FMS imagery and other standard log data, we can make a competent attempt at filling the data gap in order to have a continuous record downhole. Figure **F43** shows unit divisions based on FMS images over the entire section. It is not possible to determine the petrology of the lithology, but the structural and textural makeup is clear.

The FMS images highlight some of the key units observed in the core recovered from Hole U1382A (Fig. **F47**), including more massive flow units, brecciated sections, and potential sedimentary horizons.

However, perhaps more importantly, the FMS images help refine lithologic boundaries when contacts are not recovered in the core. Another strength of FMS imagery is the fact that the images are oriented to geographic north (using the General Purpose Inclinometry Tool [GPIT]), and by picking sinusoidal traces on the images one can obtain important oriented structural information for key boundaries, fractures, and other features of interest. It is possible to differentiate between picked fractures (be they conductive or resistive) and boundaries or pronounced fractures in the lava flows. Structural studies are a key part of postexpedition research. Such structural picks can aid overall interpretation of the lithologic sequence observed in the core and be used to orient observed structures and produce a stress regime model for the drilled formation.

One of our key scientific aims is to integrate core and log measurements, observations, and interpretations. The FMS data permit integration of core observations and images by constraining the location of recovered core pieces when recovery is low; depth uncertainty for core pieces in low recovery can be as high as 9.6 m. Before the cores were split, images of the external surfaces of the whole-round cores were taken on the line-scan imager. These images were then mosaicked together so that we could attempt to find the piece in the FMS images. Figure **F48** shows the successful result of integrating external surface whole-round core images with FMS data. This is the very first time such work has been done during an IODP expedition, and it may prove to be extraordinarily useful in repositioning core pieces. Additional time will be spent postexpedition trying to line up some of the other core images from rocks recovered from Hole U1382A.

Packer experiments

Drill string packer experiments were attempted in Hole U1382A with the intent of assessing the transmissivity and average permeability of the open-hole zone deeper than the casing shoe. The plan was to inflate the single-element packer centered at ~60 m into casing and then conduct two constant-rate injection tests of 1 h duration each. However, although the packer inflated properly, we were unable to maintain packer inflation, most likely owing to the effect of large swells (up to 3 m) produced by Tropical Storm Philippe. The packer has a single moving part, a sleeve that slides down ~25 cm after setting weight down from the rig to keep the packer inflated. This part has been reliable in past operations but is vulnerable to large swells that, if not perfectly compensated for, can pull the sleeve open and allow the pressurized fluids within the packer element to vent. This apparently occurred during four different attempts to set the packer at inflation pressures ranging from 1000 to 1500 psi and applied set-down weights of 10,000–15,000 lb (Fig. **F49**). Each time, the inflation held for roughly 10 min before unplanned deflation, which is barely enough time to register a borehole pressure reference, let alone conduct a useful test of formation hydrologic properties. After the fourth swell-induced deflation, we decided the swells were too much to handle and terminated the attempted packer experiments.

References

Alt, J.C., Teagle, D.A.H., Laverne, C., Vanko, D.A., Bach, W., Honnorez, J., Becker, K., Ayadi, M., and Pezard, P.A., 1996. Ridge-flank alteration of upper ocean crust in the eastern Pacific: synthesis of results for volcanic rocks of Holes 504B and 896A. *In* Alt, J.C., Kinoshita, H., Stokking, L.B., and Michael, P.J. (Eds.), *Proc. ODP, Sci. Results,* 148: College Station, TX (Ocean Drilling Program), 435–450. **doi:10.2973/odp.proc.sr.148.150.1996**

Barr, S.R., Révillon, S., Brewer, T.S., Harvey, P.K., and Tarney, J., 2002. Determining the inputs to the Mariana Subduction Factory: using core-log integration to reconstruct basement lithology at ODP Hole 801C. *Geochem., Geophys., Geosyst.,* 3(11):8901–8925. **doi:10.1029/2001GC000255**

Bartetzko, A., Pezard, P., Goldberg, D., Sun, Y.-F., and Becker, K., 2001. Volcanic stratigraphy of DSDP/ODP Hole 395A: an interpretation using well-logging data. *Mar. Geophys. Res.,* 22(2):111–127. **doi:10.1023/A:1010359128574**

Bougault, H., Treuil, M., and Joron J.L., 1979. Trace elements in basalts from 23°N and 36°N in the Atlantic Ocean: fractional crystallization, partial melting, and heterogeneity of the upper mantle. *In* Melson, W.G., Rabinowitz, P.D., et al., *Init. Repts. DSDP,* 45: Washington, DC (U.S. Govt. Printing Office), 493–506. **doi:10.2973/dsdp.proc.45.122.1979**

Bown, P.R. (Ed.), 1998. *Calcareous Nannofossil Biostratigraphy:* Dordrecht, The Netherlands (Kluwer Academic Publ.).

Bukry, D., 1979. Neogene coccolith stratigraphy, Mid-Atlantic Ridge, Deep Sea Drilling Project Leg 45. *In* Melson, W.G., Rabinowitz, P.D., et al., *Init. Repts. DSDP,* 45: Washington, DC (U.S. Govt. Printing Office), 307–317. **doi:10.2973/dsdp.proc.45.109.1979**

Clauser, C., and Huenges, E., 1995. Thermal conductivity of rocks and minerals. *In* Ahrens, T.J. (Ed.), *Rock Physics and Phase Relations: A Handbook of Physical Constants.* Am. Geophys. Union Ref. Shelf, 3:105–126. **doi:10.1029/RF003p0105**

Donaldson, C.H., 1976. An experimental investigation of olivine morphology. *Contrib. Mineral. Petrol.,* 57(2):187–213. **doi:10.1007/BF00405225**

Edwards, K.J., Wheat, C.G., Orcutt, B.N., Hulme, S., Becker, K., Jannasch, H., Haddad, A., Pettigrew, T., Rhinehart, W., Grigar, K., Bach, W., Kirkwood, W., and Klaus, A., 2012. Design and deployment of borehole observatories and experiments during IODP Expedition 336, Mid-Atlantic Ridge flank at North Pond. *In* Edwards, K.J., Bach, W., Klaus, A., and the Expedition 336 Scientists, *Proc. IODP,* 336: Tokyo (Integrated Ocean Drilling Program Management International, Inc.). **doi:10.2204/iodp.proc.336.109.2012**

Expedition 336 Scientists, 2012. Methods. *In* Edwards, K.J., Bach, W., Klaus, A., and the Expedition 336 Scientists, *Proc. IODP,* 336: Tokyo (Integrated Ocean Drilling Program Management International, Inc.). **doi:10.2204/iodp.proc.336.102.2012**

Fisher, A.T., Wheat, C.G., Becker, K., Davis, E.E., Jannasch, H., Schroeder, D., Dixon, R., Pettigrew, T.L., Meldrum, R., McDonald, R., Nielsen, M., Fisk, M., Cowen, J., Bach, W., and Edwards, K., 2005. Scientific and technical design and deployment of long-term subseafloor observatories for hydrogeologic and related experiments, IODP Expedition 301, eastern flank of Juan de Fuca Ridge. *In* Fisher, A.T., Urabe, T., Klaus, A., and the Expedition 301 Scientists, *Proc. IODP,* 301: College Station, TX (Integrated Ocean Drilling Program Management International, Inc.). **doi:10.2204/iodp.proc.301.103.2005**

Fisk, M.R., Giovannoni, S.J., and Thorseth, I.H., 1998. Alteration of oceanic volcanic glass: textural evidence of microbial activity. *Science,* 281(5379):978–980. **doi:10.1126/science.281.5379.978**

Flaum, C., Galford, J.E., and Hastings, A., 1987. Enhanced vertical resolution processing of dual detector gamma-gamma density logs. *Trans. SPWLA Annu. Logging Symp.,* 28.

Honnorez, J., 1972. La palagonitisation: l'alteration sous-marine du verre volcanique basique de Palagonia (Sicile) [Palagonitization: the submarine alteration of basic volcanic glass in Palagonia, Sicily]. *Publ. Vulkaninst. Immanuel Friedlaender,* 9.

Jarrard, R.D., and Kerneklian, M.J., 2007. Data report: physical properties of the upper oceanic crust of ODP Site 1256: multisensor track and moisture and density measurements. *In* Teagle, D.A.H., Wilson, D.S., Acton, G.D., and Vanko, D.A. (Eds.), *Proc. ODP, Sci. Results,* 206: College Station, TX (Ocean Drilling Program), 1–11. **doi:10.2973/odp.proc.sr.206.011.2007**

Juteau, T., Bingöl, F., Noack, Y., Whitechurch, H., Hoffert, M., Wirrmann, D., and Courtois, C., 1979. Preliminary results: mineralogy and geochemistry of alteration products in Leg 45 basement samples. *In* Melson, W.G., Rabinowitz, P.D., et al., *Init. Repts. DSDP,* 45: Washington, DC (U.S. Govt. Printing Office), 613–645. **doi:10.2973/dsdp.proc.45.138.1979**

Melson, W.G., Rabinowitz, P.D., et al., 1979. *Init. Repts. DSDP,* 45: Washington, DC (U.S. Govt. Printing Office). **doi:10.2973/dsdp.proc.45.1979**

Natland, J.H., 1979. Crystal morphologies in basalts from DSDP Site 395, 23°N, 46°W, Mid-Atlantic Ridge. *In* Melson, W.G., Rabinowitz, P.D., et al., *Init. Repts. DSDP,* 45: Washington, DC (U.S. Govt. Printing Office), 423–445. **doi:10.2973/dsdp.proc.45.118.1979**

Niu, Y., 2004. Bulk-rock major and trace element compositions of abyssal peridotites: implications for mantle melting, melt extraction and post-melting processes beneath mid-ocean ridges. *J. Petrol.,* 45(12):2423–2458. **doi:10.1093/petrology/egh068**

Orcutt, B., Wheat, C.G., and Edwards, K.J., 2010. Subseafloor ocean crust microbial observatories: development of FLOCS (Flow-Through Osmo Colonization System) and evaluation of borehole construction materials. *Geomicrobiol. J.,* 27(2):143–157. **doi:10.1080/01490450903456772**

Orcutt, B.N., Bach, W., Becker, K., Fisher, A.T., Hentscher, M., Toner, B.M., Wheat, C.G., and Edwards, K.J., 2011. Colonization of subsurface microbial observatories deployed in young ocean crust. *ISME J.,* 5:692–703. **doi:10.1038/ismej.2010.157**

Orcutt, B.N., Barco, R.A., Joye, S.B., and Edwards, K.J., 2012. Summary of carbon, nitrogen, and iron leaching characteristics and fluorescence properties of materials considered for subseafloor observatory assembly. *In* Edwards, K.J., Bach, W., Klaus, A., and the Expedition 336 Scientists, *Proc. IODP,* 336: Tokyo (Integrated Ocean Drilling Program Management International, Inc.). **doi:10.2204/iodp.proc.336.108.2012**

Passchier, C.W., and Trouw, R.A.J., 2005. *Microtectonics* (2nd ed.): Berlin (Springer).

Plank, T., Ludden, J.N., Escutia, C., et al., 2000. *Proc. ODP, Init. Repts.,* 185: College Station, TX (Ocean Drilling Program). **doi:10.2973/odp.proc.ir.185.2000**

Rhodes, J.M., Blanchard, D.P., Dungan, M.A., Rodgers, K.V., and Brannon, J.C., 1979. Chemistry of Leg 45 basalts. *In* Melson, W.G., Rabinowitz, P.D., et al., *Init. Repts. DSDP,* 45: Washington, DC (U.S. Govt. Printing Office), 447–459. **doi:10.2973/dsdp.proc.45.119.1979**

Seaver, M., Roselle, D.C., Pinto, J.F., and Eversole, J.D., 1998. Absolute emission spectra from *Bacillus subtilis* and *Escherichia coli* vegetative cells in solution. *Appl. Opt.,* 37(22):5344–5347. **doi:10.1364/AO.37.005344**

Shipboard Scientific Party, 1979. Site 395: 23°N, Mid-Atlantic Ridge. *In* Melson, W.G., Rabinowitz, P.D., et al., *Init. Repts. DSDP,* 45: Washington, DC (U.S. Govt. Printing Office), 131–264. **doi:10.2973/dsdp.proc.45.107.1979**

Turner, G., Enright, M.C., Cadogan, P.H., and Graham, A.L., 1979. Preliminary ^{40}Ar/^{39}Ar studies on phyric basalts from Hole 395A, DSDP Leg 45. *In* Melson, W.G., Rabinowitz, P.D., et al., *Init. Repts. DSDP,* 45: Washington, DC (U.S. Govt. Printing Office), 539. **doi:10.2973/dsdp.proc.45.128.1979**

Walker, J.D., and Geissman, J.W., 2009. 2009 GSA geologic time scale. *GSA Today,* 19(4):60 **doi:10.1130/1052-5173-19.4-5.60**

Wheat, C.G., Jannasch, H.W., Kastner, M., Hulme, S., Cowen, J., Edwards, K.J., Orcutt, B.N., and Glazer, B., 2011. Fluid sampling from oceanic borehole observatories: design and methods for CORK activities (1990–2010). *In* Fisher, A.T., Tsuji, T., Petronotis, K., and the Expedition 327 Scientists, *Proc. IODP,* 327: Tokyo (Integrated Ocean Drilling Program Management International, Inc.). **doi:10.2204/iodp.proc.327.109.2011**

Publication: 16 November 2012
MS 336-104

Figure F1. Schematic of Hole U1382A subseafloor borehole observatory (CORK) configuration.

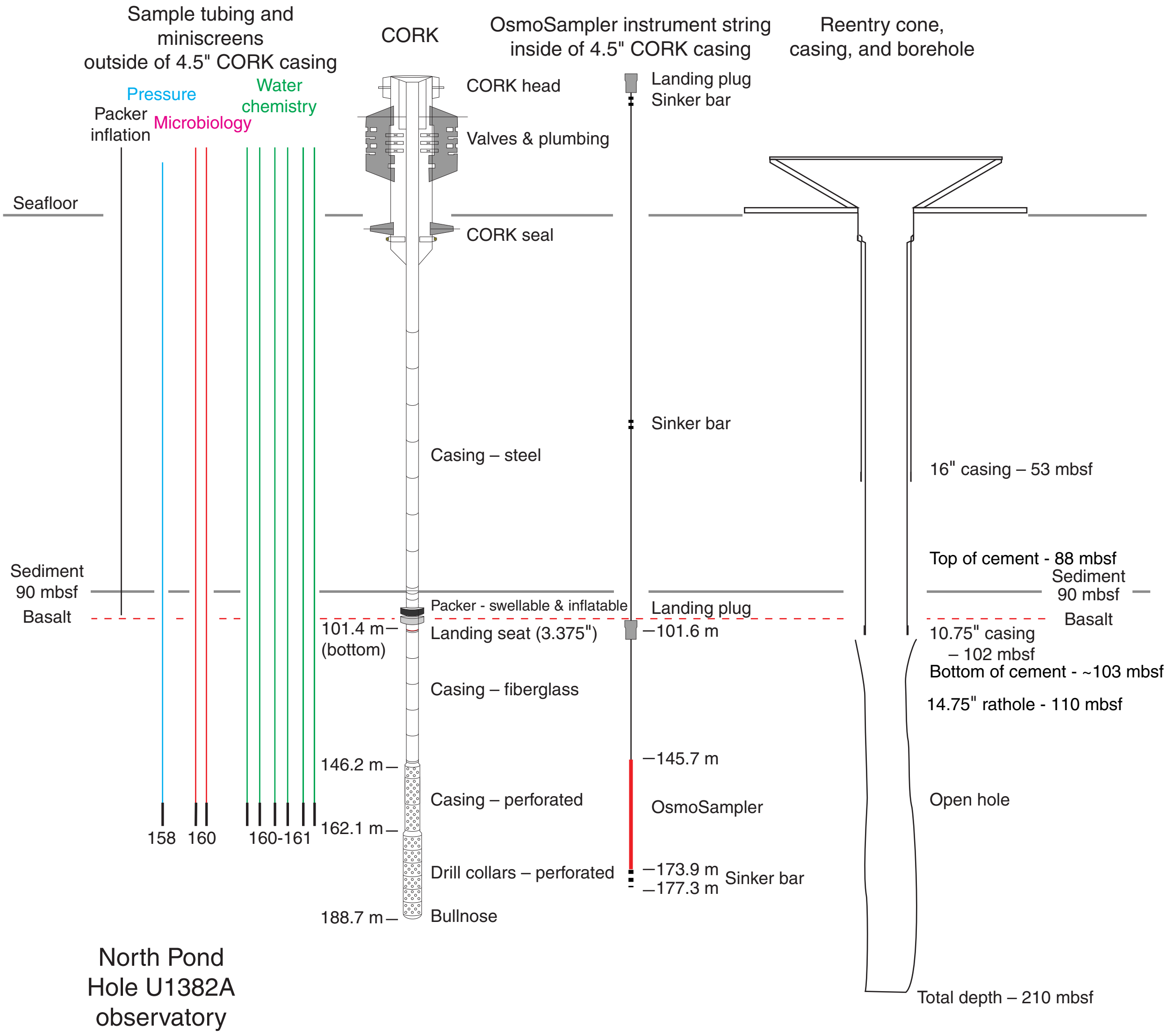

Figure F2. Engineering drawing showing configuration and space out of Hole U1382A reentry cone and casing, along with main subseafloor borehole observatory (CORK) structure. csg = casing, stl = steel. MBIO = microbiology.

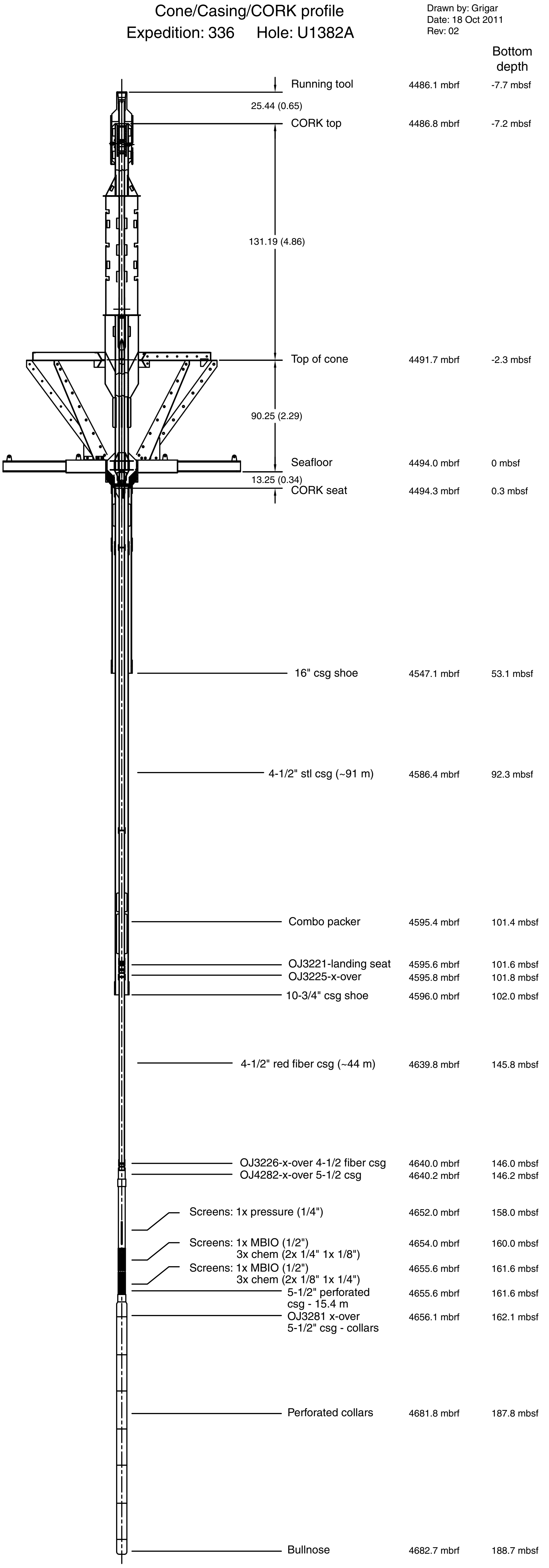

Figure F3. Hole U1382A lithologic summary. Broad changes in lithology or primary igneous structure are illustrated with different colors in the sequence column.

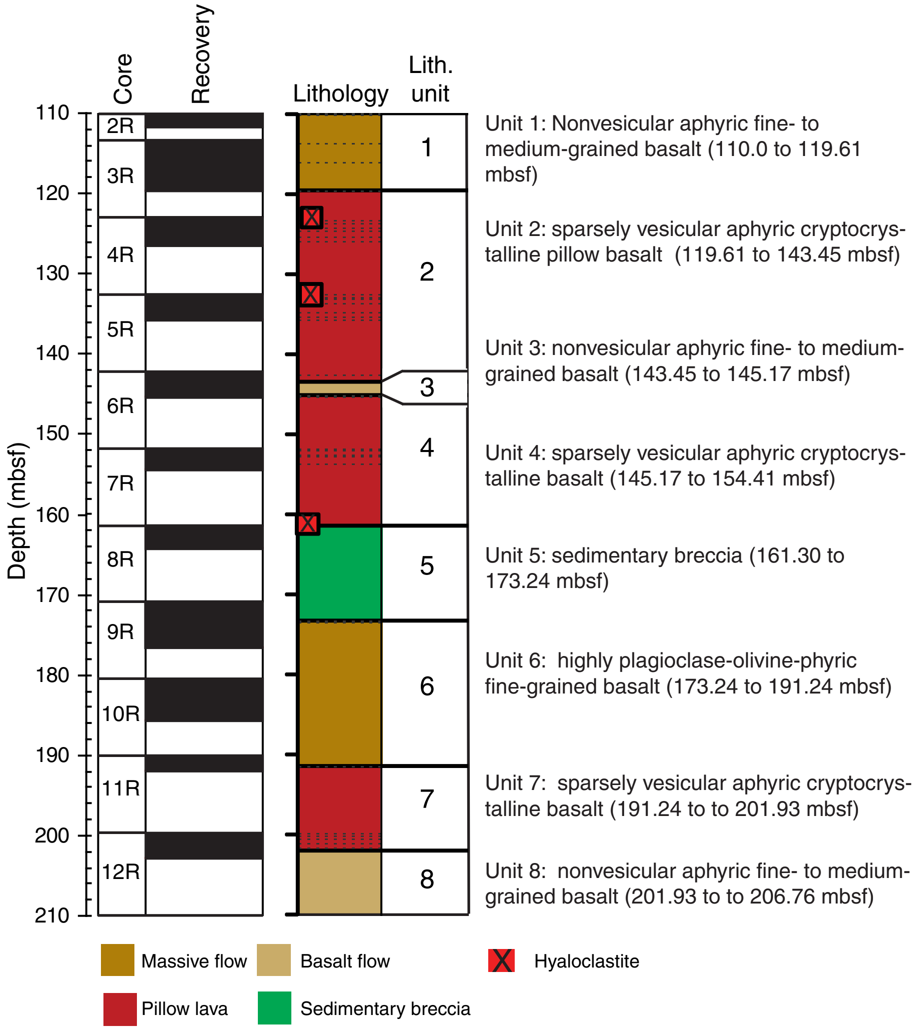

Figure F4. Close-up photographs (half-core and whole-round core images) of patchy alteration and halos encountered in different units, Hole U1382A. **A.** Aphyric basalt from Unit 1 (massive flow) showing darker gray (freshest) basalt surrounded by grayish-brown alteration halos (interval 336-U1382A-2R-1, 90–112 cm [Piece 11]). **B.** Highly porphyritic basalt from Unit 6 (massive flow) showing darker gray (freshest) basalt with white plagioclase phenocrysts surrounded by grayish-brown alteration halos (interval 336-U1382A-10R-1, 85–107 cm [Piece 10]). **C.** Harzburgite with granular texture from Unit 5 (sedimentary breccia) showing a brown to green pseudomorphic alteration halo along a 3 mm thick carbonate vein (interval 336-U1382A-8R-4, 51–63 cm [Piece 5]).

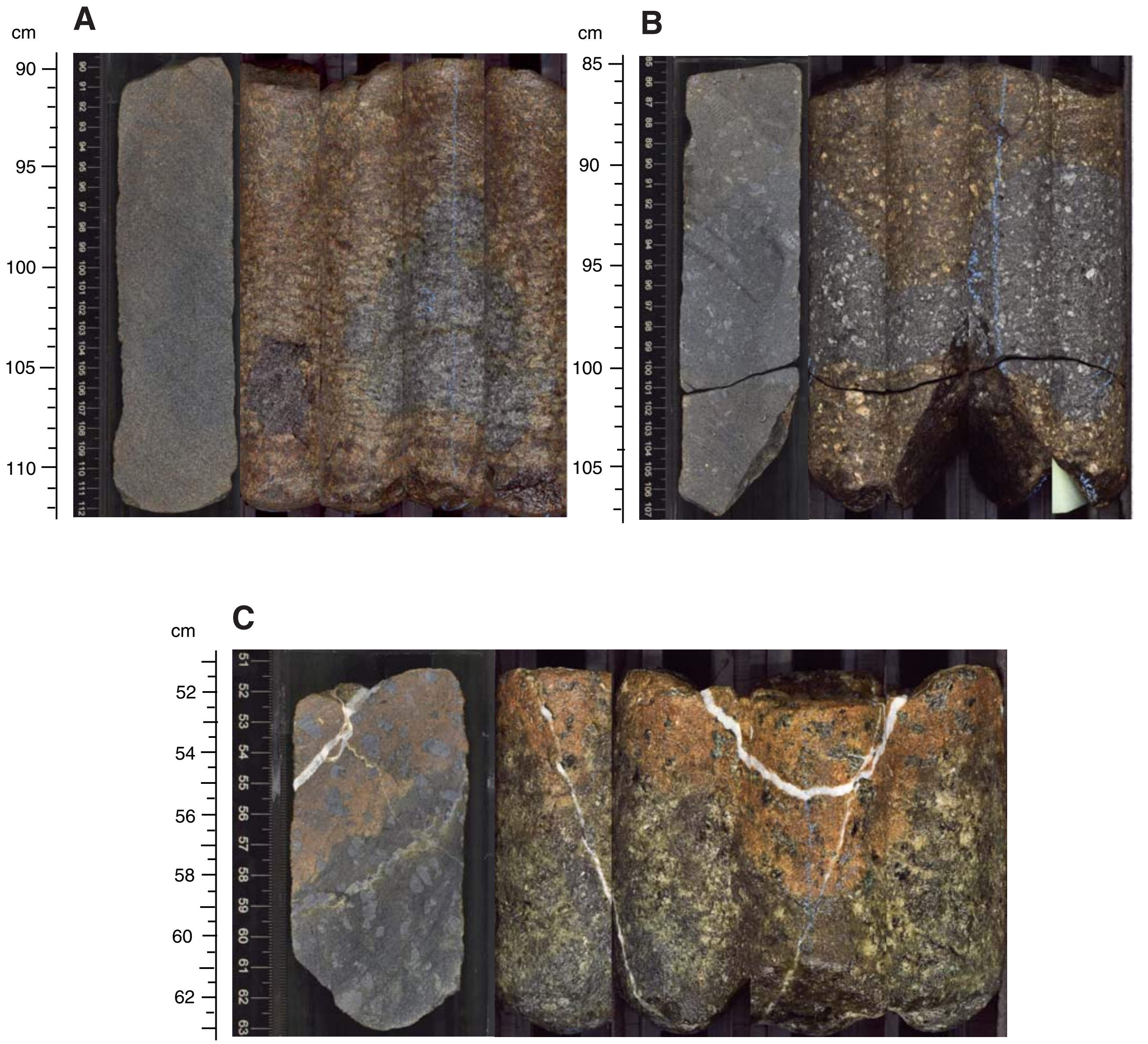

Figure F5. Aphyric nonvesicular medium-grained basalt from Unit 1 (massive flow) (interval 336-U1382A-3R-2, 99–103 cm [Piece 11]). Red boxes show location of thin section and photomicrographs. **A.** Photograph of basalt piece with typical patchy alteration. **B.** Photomicrograph of granular to intersertal texture (thin section = 25 mm wide; plane polarization). **C.** Same as B in cross-polarized light.

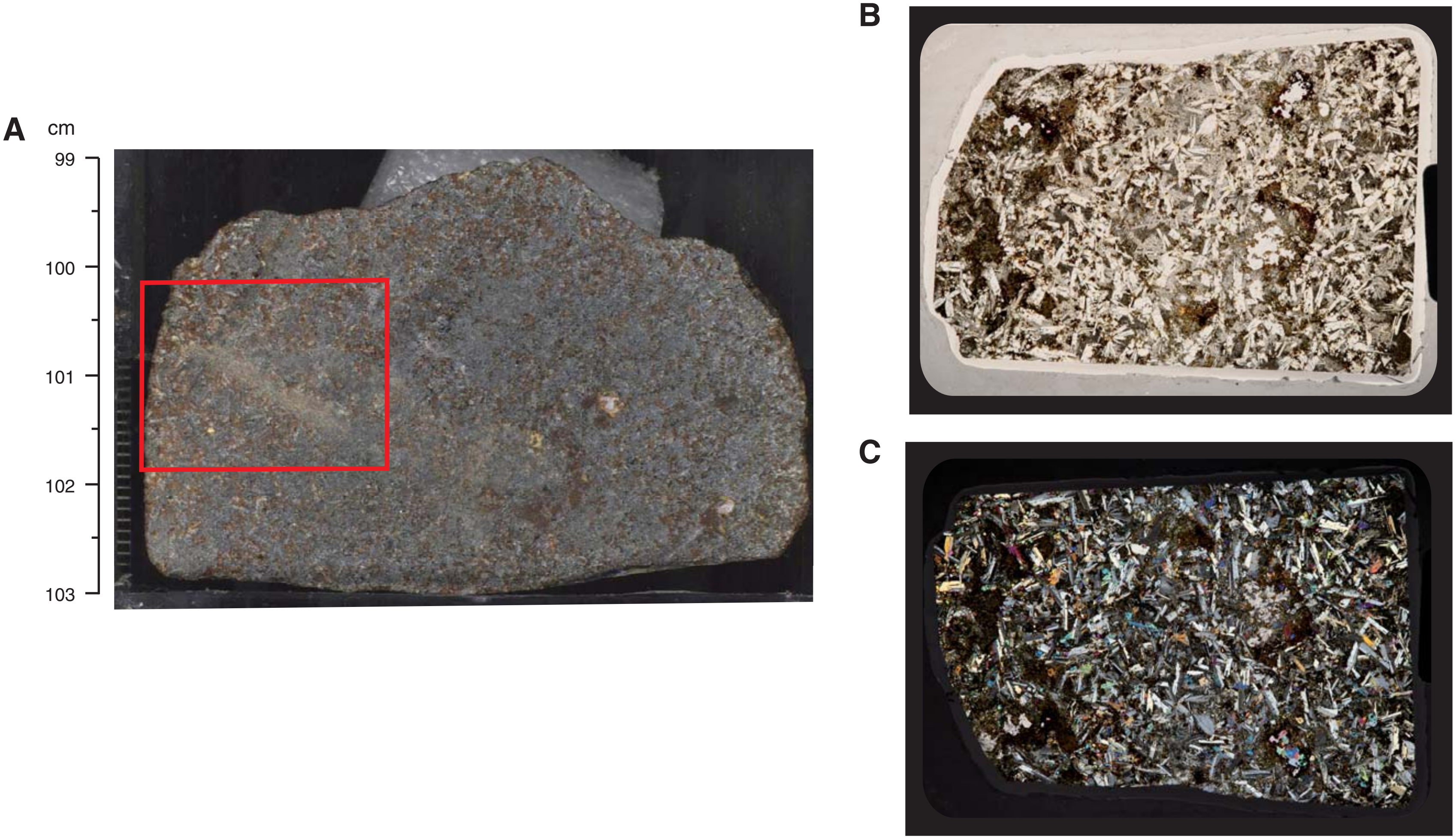

Figure F6. Aphyric basalt with blotchy alteration texture from Unit 2 (pillow lava) (Section 336-U1382A-4R-1). **A.** Close-up photograph of cryptocrystalline groundmass with variolitic domains (Section 4R-1, 70–76 cm [Piece 9]). **B.** Thin section photomicrograph showing three domains separated by red lines: (1) cryptocrystalline groundmass with rare varioles, (2) variolitic part in center with numerous varioles, and (3) microcrystalline part with faint variolitic texture (Section 4R-1, 76–81 cm [Piece 10]). Olivine microphenocryst contents are uniform. Thin section = 25 mm wide; plane polarization.

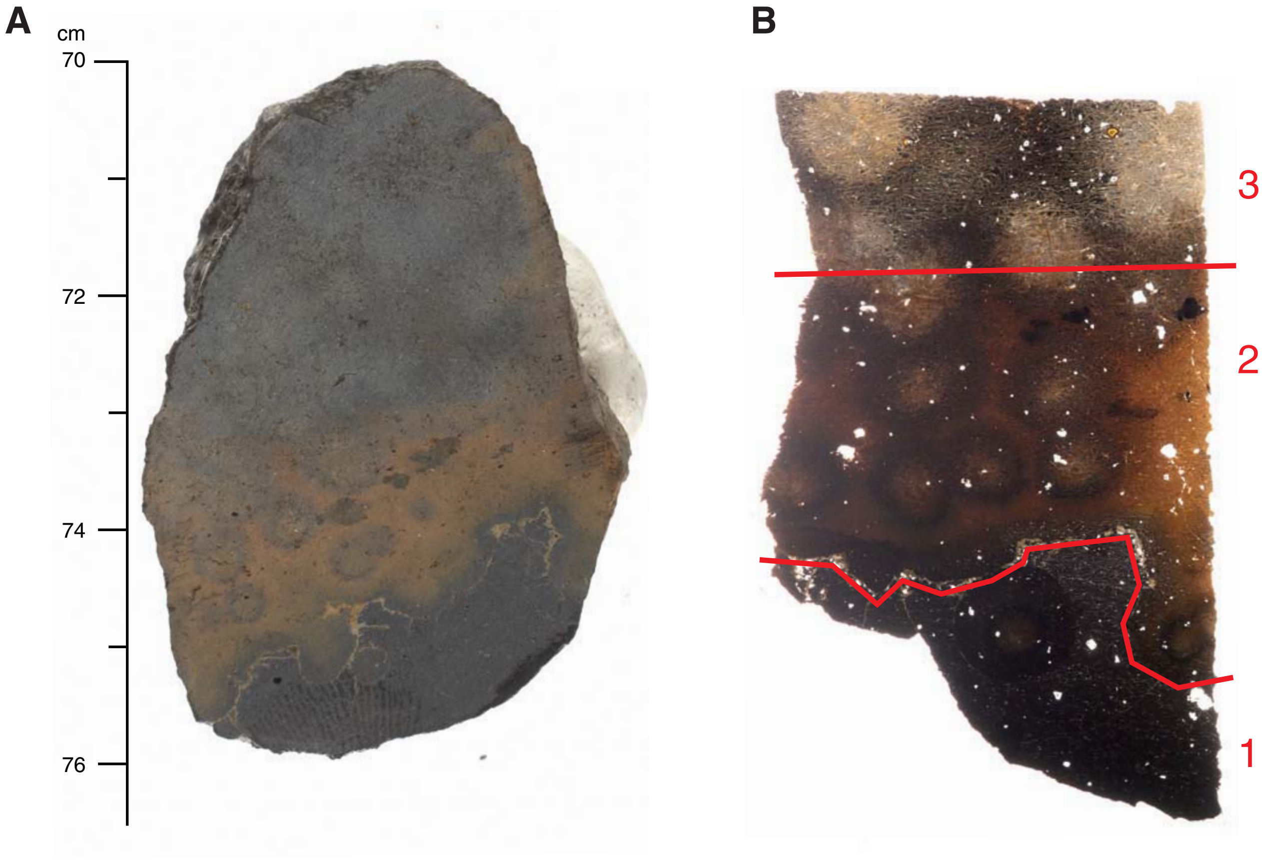

Figure F7. Close-up photograph of brecciated subunits from Unit 2 (pillow lava) (Section 336-U1382A-5R-1). **A.** Hyaloclastite with poorly sorted angular clasts of highly altered glass. Larger clasts develop red to light brown concentric alteration halos representing more smectitic or iddingsitic mineral replacement. The reddish-brown microcrystalline matrix is enriched in Fe oxyhydroxides and clay filling (Section 5R-1, 114–119 cm [Piece 21]). **B.** Close-up showing reddish-brown matrix and various degrees of glass alteration (binocular microscope ×0.6; wet surface). **C.** Close-up showing freshest dark gray cryptocrystalline basalt within hyaloclastite, with branching anastomosing veins composed of Fe-rich smectite and white zeolite (binocular microscope ×0.8; wet surface).

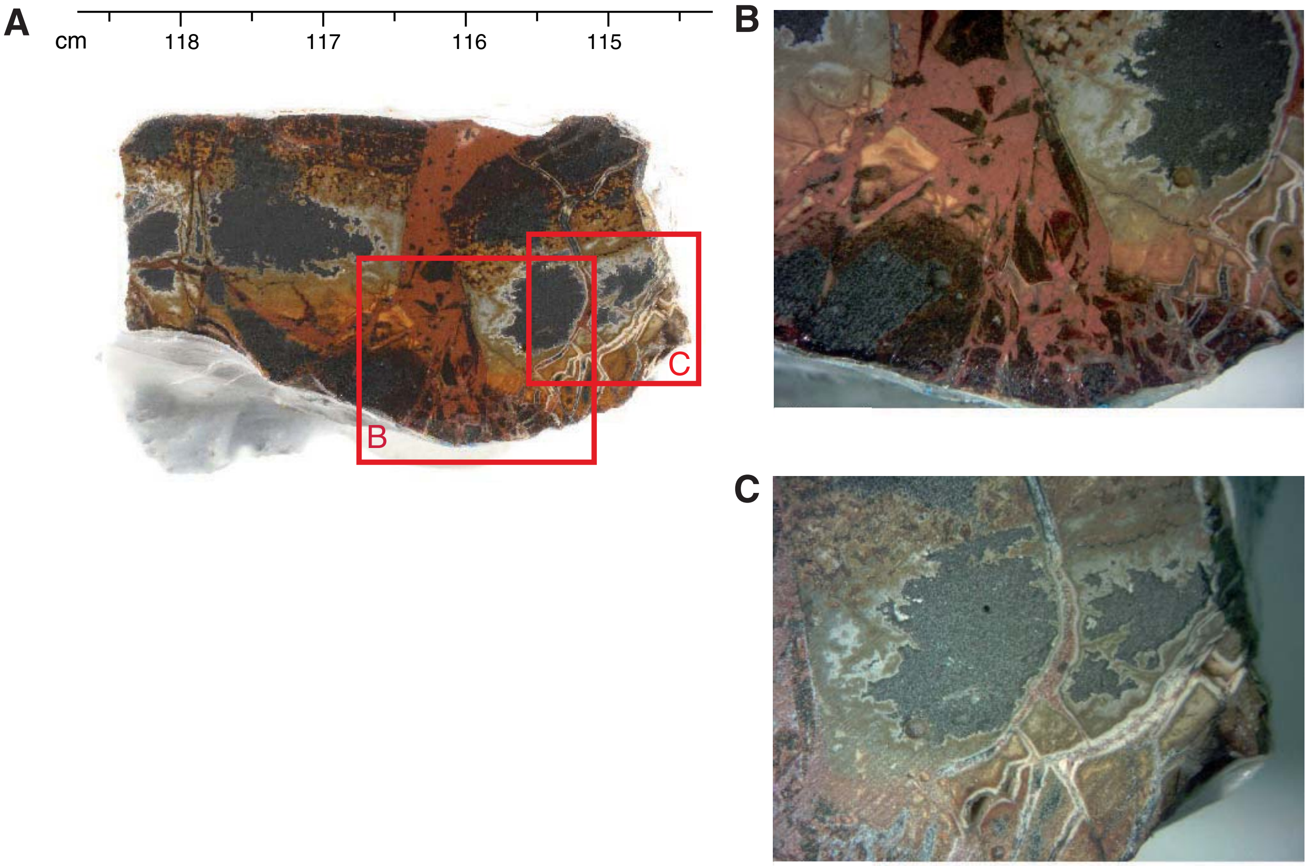

Figure F8. Close-up photograph (half-core and whole-round score scanner) and photomicrograph of harzburgite from Unit 5 (sedimentary breccia) (interval 336-U1382A-9R-1, 91–106 cm [Piece 14B]). Red boxes show location of thin section and photomicrographs. **A.** Serpentinized coarse-grained harzburgite with a network of carbonate veins. **B.** Same as A, showing whole-round core picture photomosaic. **C.** Thin section photomicrograph showing coarse-grained granular texture in crosscutting carbonate and manganese oxide–rich veins (thin section = 25 mm wide). **D.** Photomicrograph of granular olivine with subgrain boundaries and granular orthopyroxene (field of view= 5 mm; cross-polarized light).

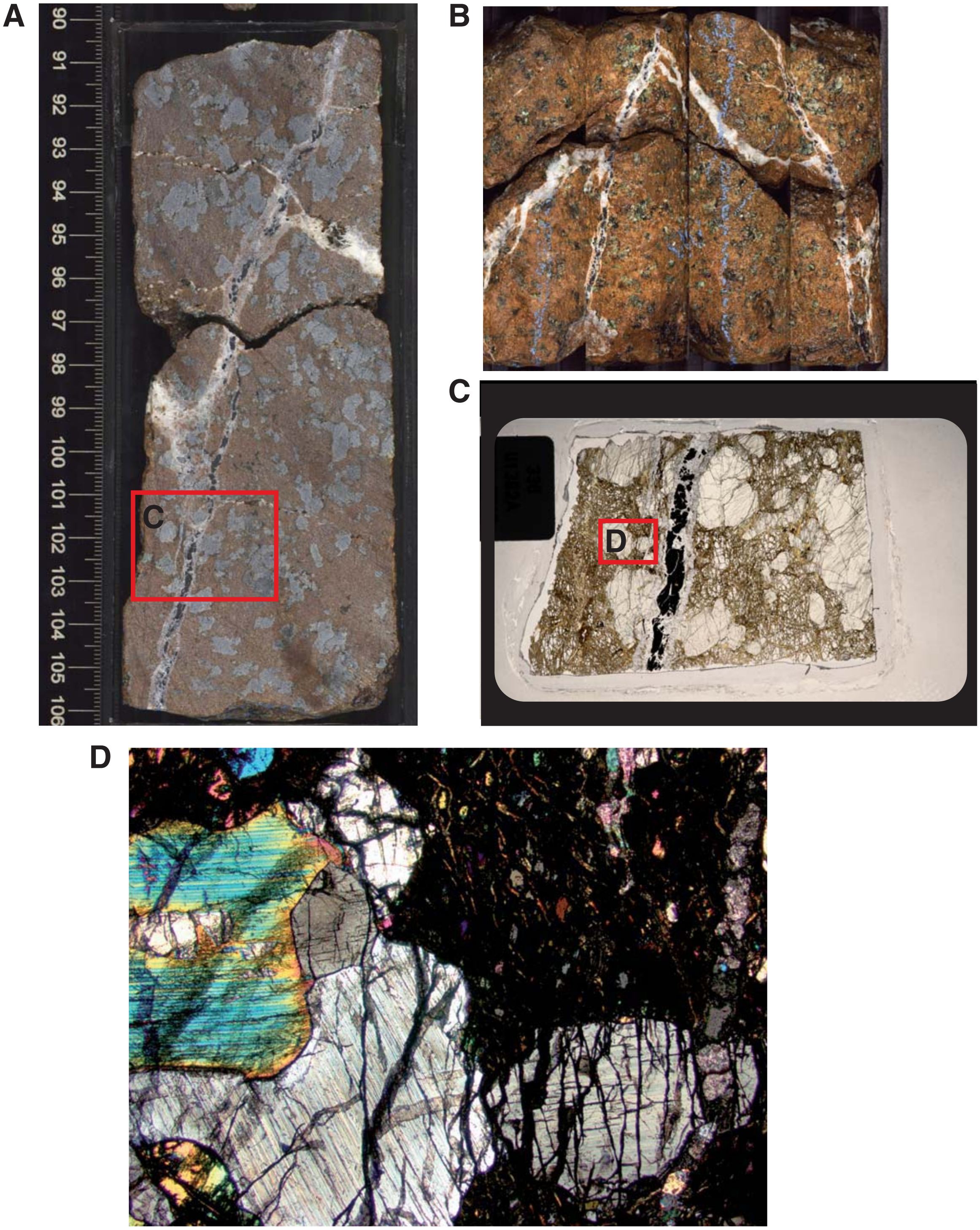

Figure F9. Close-up photograph of sedimentary breccia found in Unit 5 (interval 336-U1382A-8R-4, 32–42 cm [Piece 4]), composed of poorly sorted angular clasts (brown clasts of serpentinite are possibly foliated) in a light brown clayey to silty lithified matrix of sedimentary origin.

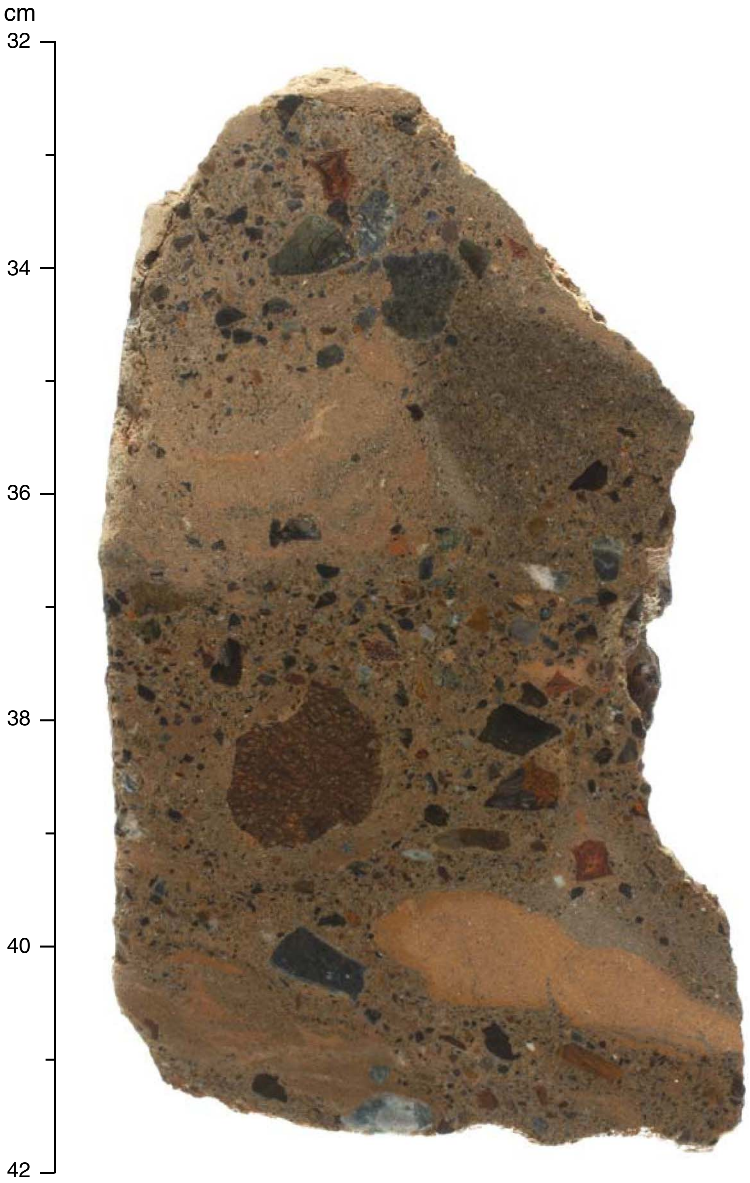

Figure F10. Close-up photograph and photomicrograph of highly porphyritic basalt from Unit 6. Red boxes show location of thin section and photomicrograph. **A.** Microcrystalline to fine-grained groundmass with plagioclase phenocrysts (<0.5 mm) (interval 336-U1382A-10R-2, 107–119 cm [Piece 10]). **B.** Thin section showing two domains separated by a dashed line, dividing a chilled margin domain on the right with hyalophitic and cryptocrystalline groundmass from another domain on the left with groundmass grain size increasing with distance from the glassy margin (red arrow) (thin section = 25 mm wide). **C.** Euhedral to subhedral glomerocryst of plagioclase and clinopyroxene (field of view = 5 mm; cross-polarized).

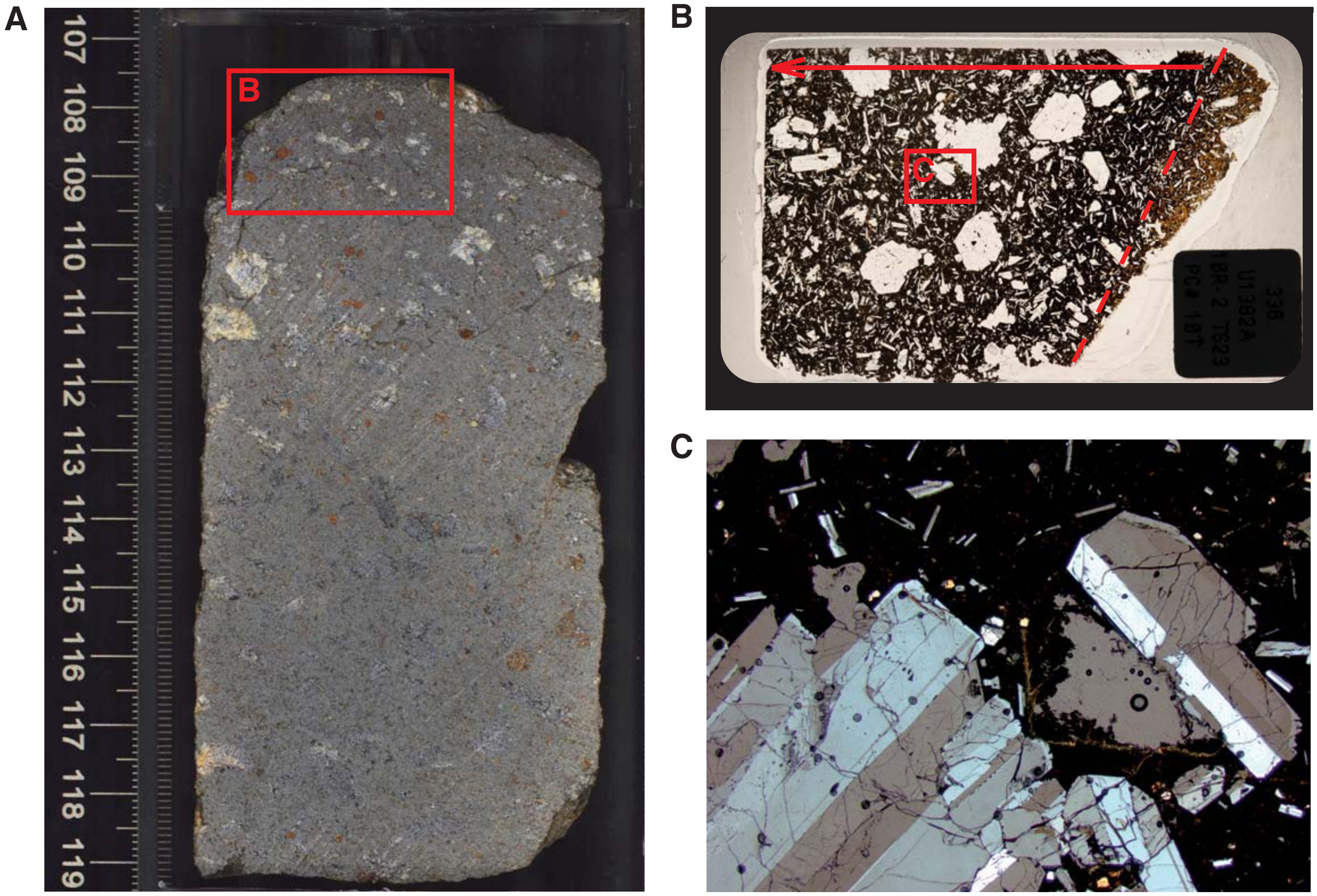

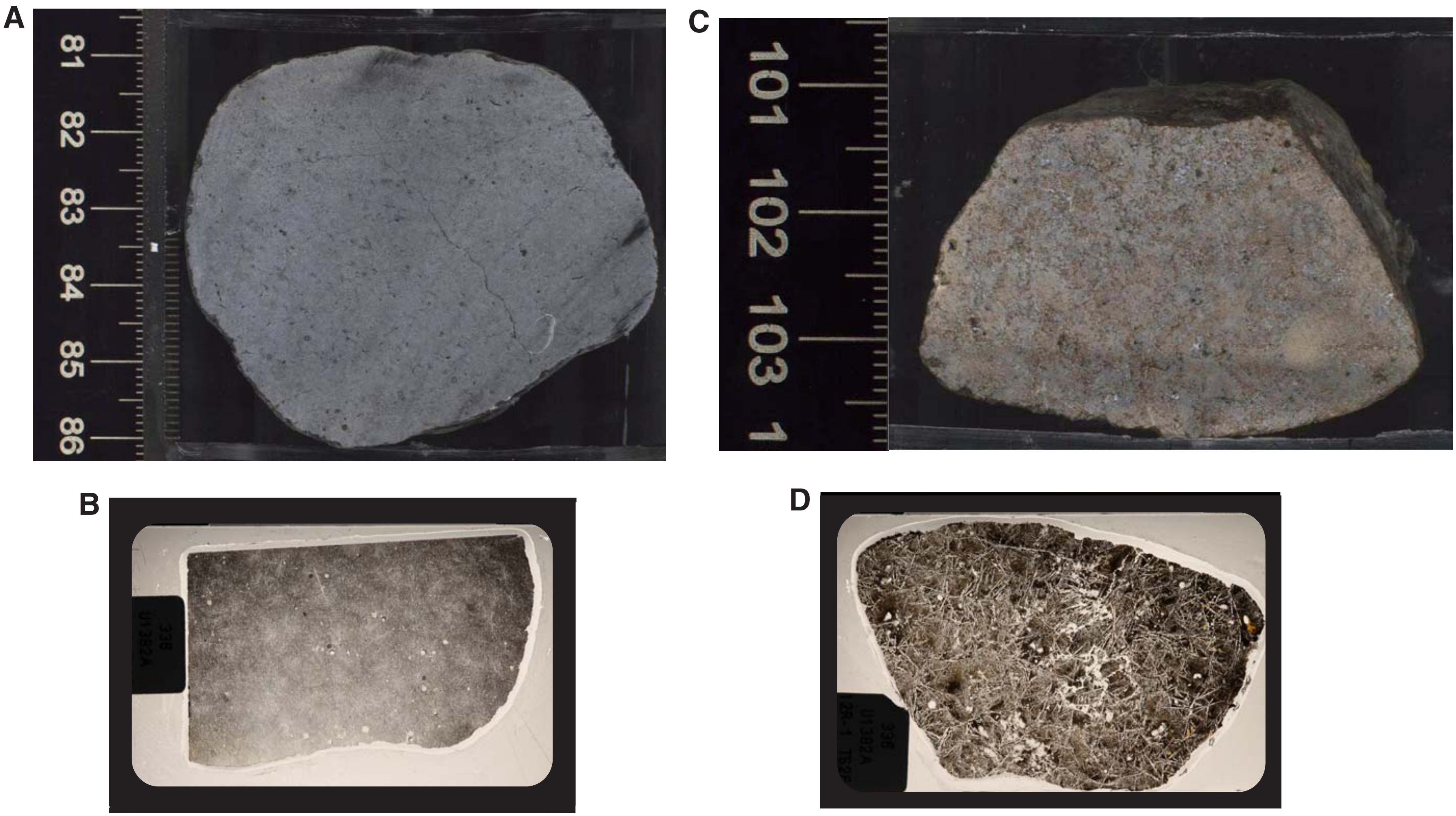

Figure F11. Close-up photograph and photomicrograph of aphyric basalt representative of Unit 7 (pillow lava). **A, B.** Interval 336-U1382A-12R-1, 81–86 cm (Piece 18): (A) sparsely vesicular aphyric basalt with cryptocrystalline to glassy groundmass with intersertal texture, (B) cryptocrystalline to glassy groundmass with intersertal texture that is sparsely vesicular (thin section = 25 mm wide; single polarization). **C, D.** Interval 336-U1382A-12R-1, 101–104 cm (Piece 21): (C) cryptocrystalline to glassy aphyric basalt with grayish-brown patchy alteration, (D) intersertal texture with euhedral olivine mostly replaced by brown clay, with tabular and needle plagioclase with intergrown anhedral clinopyroxene (thin section = 25 mm wide; cross polarization).

Figure F12. Close-up photograph and photomicrograph of aphyric fine- to medium-grained basalt from Unit 8 (basalt flow) (interval 336-U1382A-12R-3, 30–37 cm [Piece 4]). Red boxes show location of slide image and photomicrograph. **A.** Close-up from core scanner image. **B.** Thin section photograph. **C.** Photomicrograph showing granular to intersertal texture with fresh plagioclase and clinopyroxene and partly altered olivine (field of view = 2.5 mm; cross-polarized light).

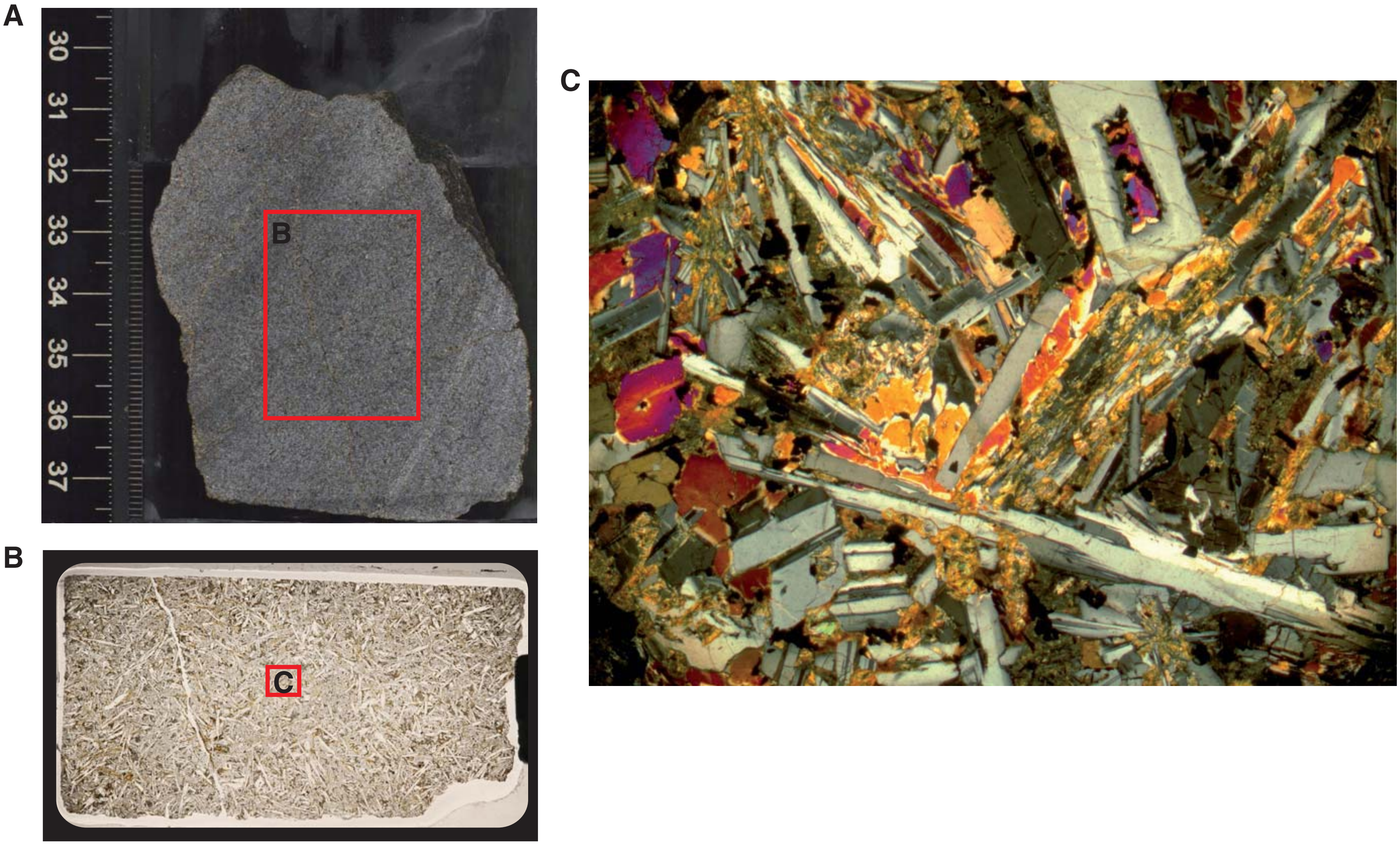

Figure F13. Photomicrographs of basaltic rocks, Hole U1382A. **A.** Euhedral olivine inclusions in tabular plagioclase crystals (interval 336-U1382A-3R-4, 82–99 cm, Thin Section 3). **B.** Olivine microphenocrysts pseudomorphed by yellowish clay minerals and brown Fe oxyhydroxide (interval 336-U1382A-5R-1, 31–36 cm, Thin Section 7). **C.** Tightly clustered tabular plagioclase forming a single glomerocryst (interval 336-U1382A-10R-2, 106–119 cm, Thin Section 23). **D, E.** Interval 336-U1382A-10R-2, 66–97.5 cm, Thin Section 24: (D) plagioclase-olivine-clinopyroxene mixed-phase glomerocryst, (E) spherulites and glass in a chilled margin of massive lava. A, C, and D are under cross-polarized light; B and E are under transmitted light.

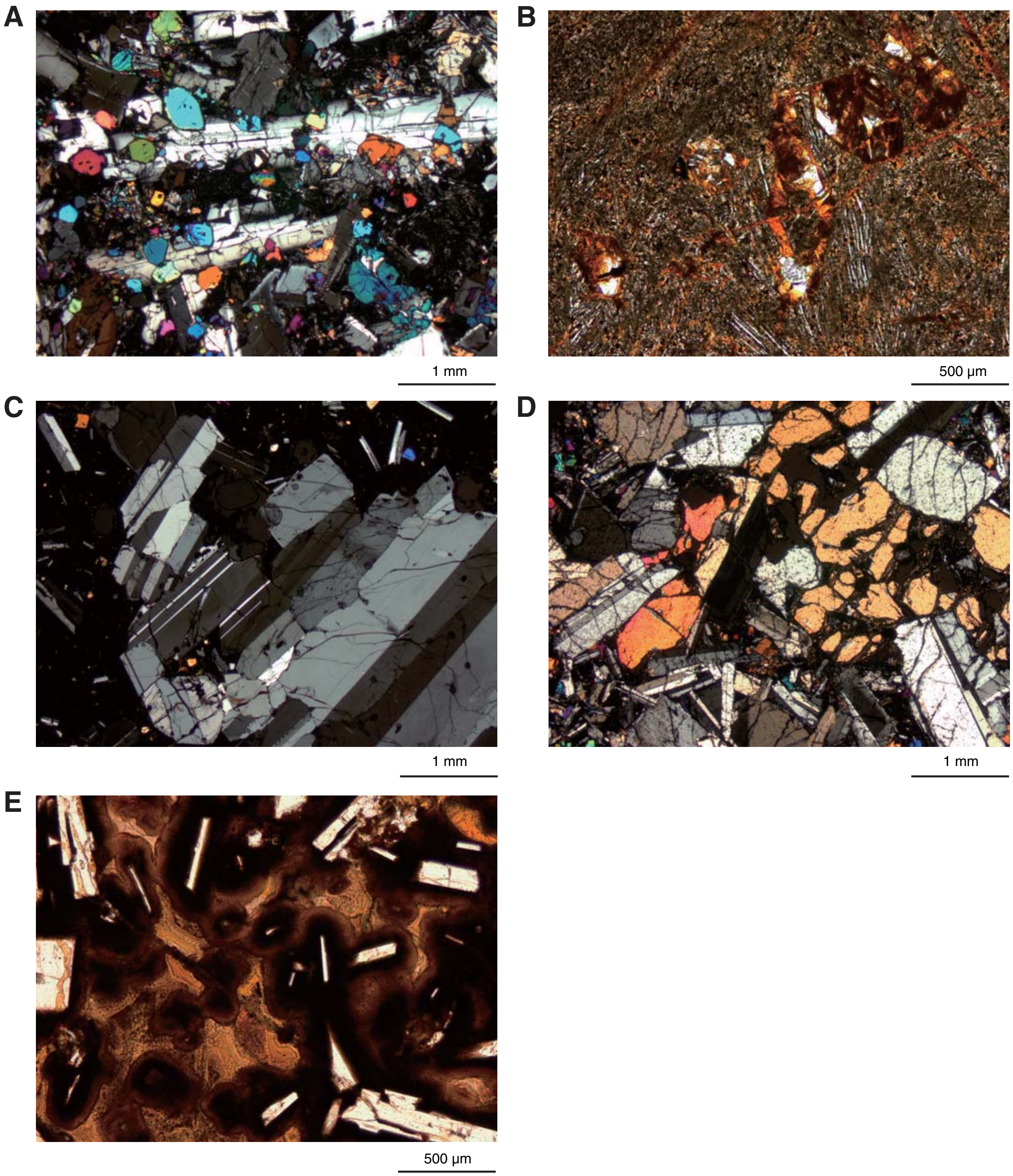

Figure F14. Whole thin section images of olivine gabbros and serpentinized peridotites (cross-polarized light). **A.** Sample 336-U1382A-9R-1 (Piece 14B), Thin Section 17. Thin section = 32 mm wide. **B.** Section 336-U1382A-9R-1 (Piece 12), Thin Section 16. Thin section = 30 mm wide. **C.** Section 336-U1382A-8R-1 (Piece 4), Thin Section 14. Thin section = 30 mm wide. **D.** Section 336-U1382A-8R-4 (Piece 3), Thin Section 19. Thin section = 48 mm wide.

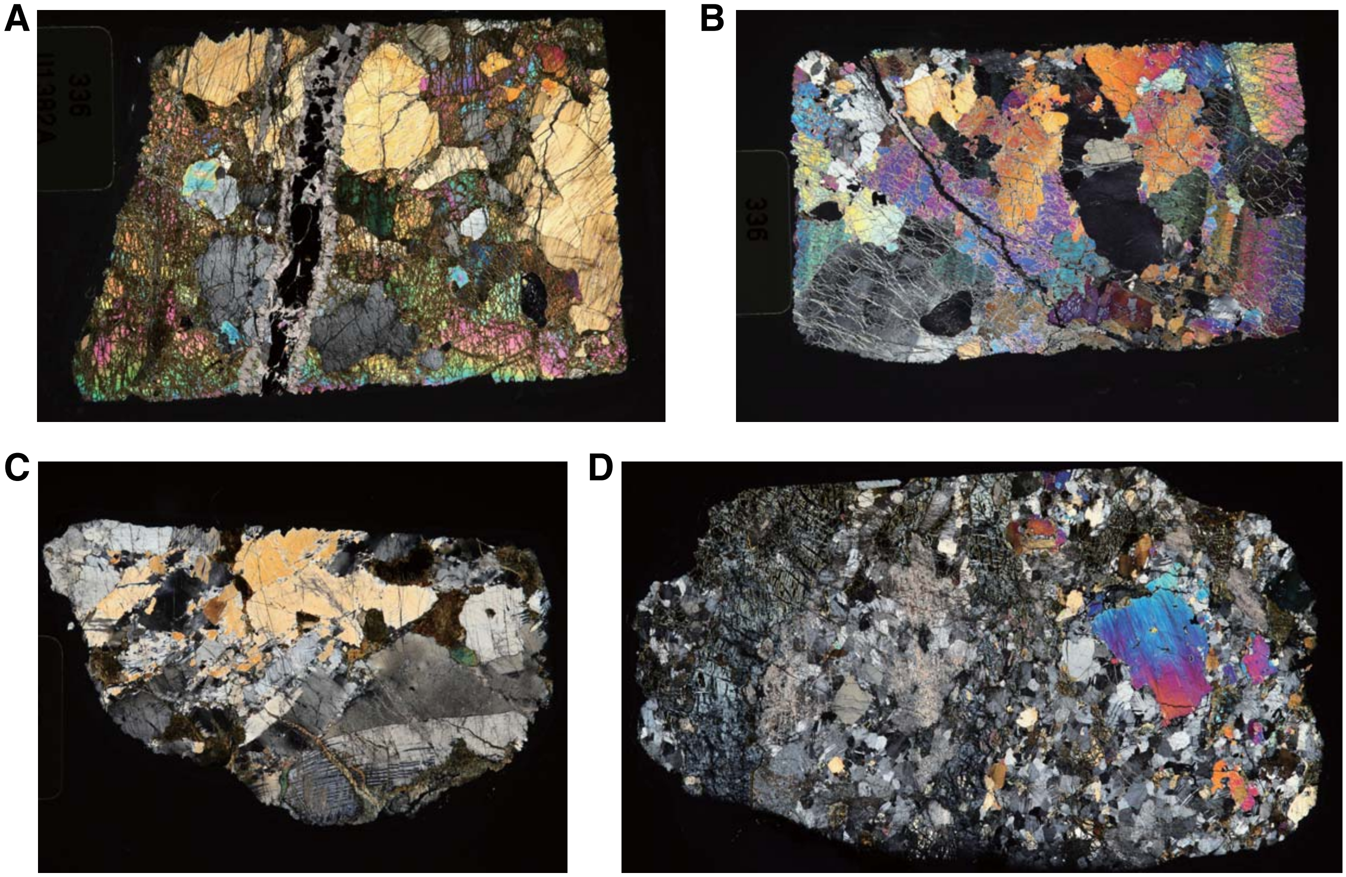

Figure F15. Photomicrographs of microstructures in olivine gabbros (cross-polarized light). **A.** Olivine gabbro mylonite indicating foliation defined by layers of plagioclase and clinopyroxene/olivine (Sample 336-U1382A-9R-1 [Piece 5], Thin Section 15). **B.** Plagioclase porphyroclast and matrix (Section 336-U1382A-8R-4 [Piece 3], Thin Section 19). **C.** Secondary prehnite and laumontite in plagioclase porphyroclast (Section 336-U1382A-8R-1 [Piece 4], Thin Section 14).

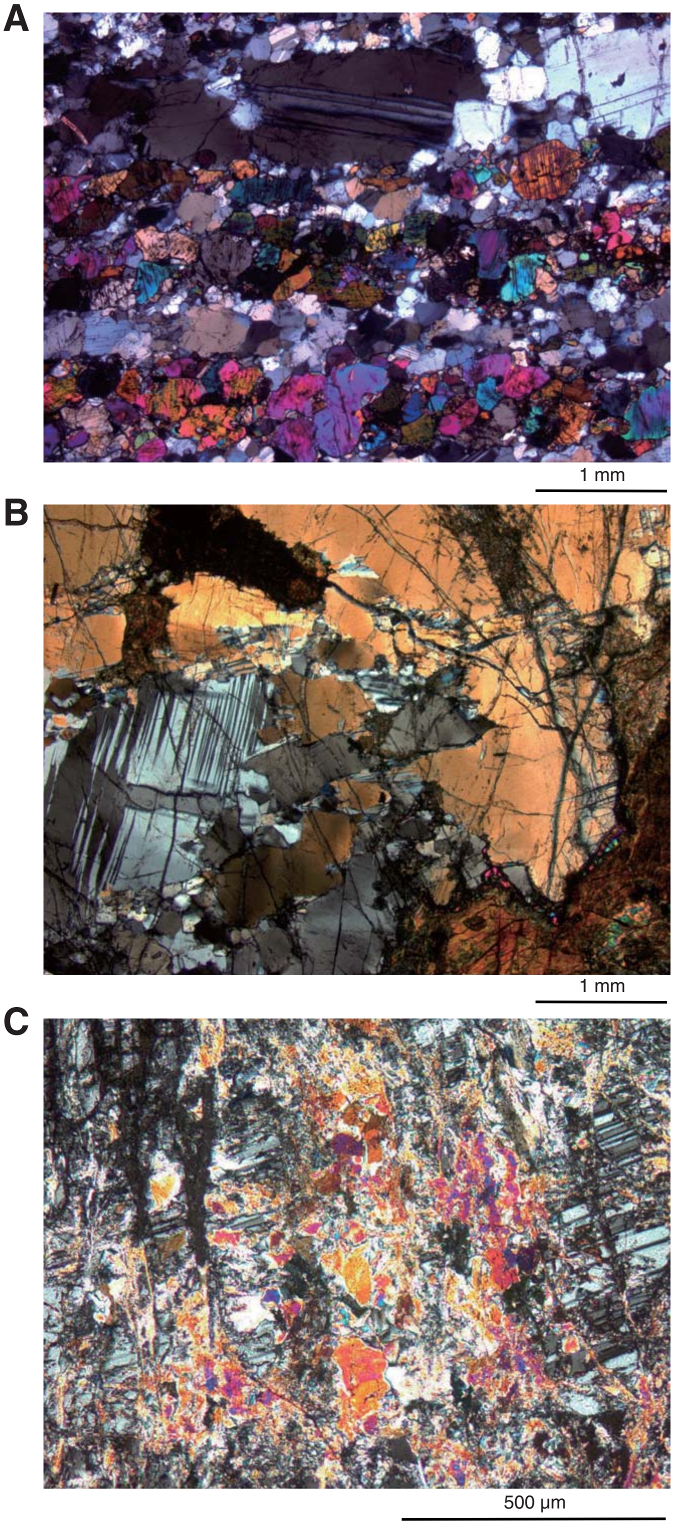

Figure F16. Photomicrographs of microstructures in serpentinized harzburgites and lherzolites (cross-polarized light). **A–C.** Section 336-U1382A-8R-4 (Piece 6), Thin Section 18: (A) olivine subgrain boundary in harzburgite, (B) spinel in harzburgite, (C) thin carbonate vein in harzburgite. **D.** Carbonate vein with manganese oxide and plagioclase in harzburgite (Section 336-U1382A-9R-1 [Piece 14B], Thin Section 17). **E, F.** Section 336-U1382A-9R-1 (Piece 12), Thin Section 16: (E) slightly bending orthopyroxene showing wavy extinction and exsolution lamella in lherzolite, (F) plagioclase occurring interstitially between olivine grains in lherzolite.

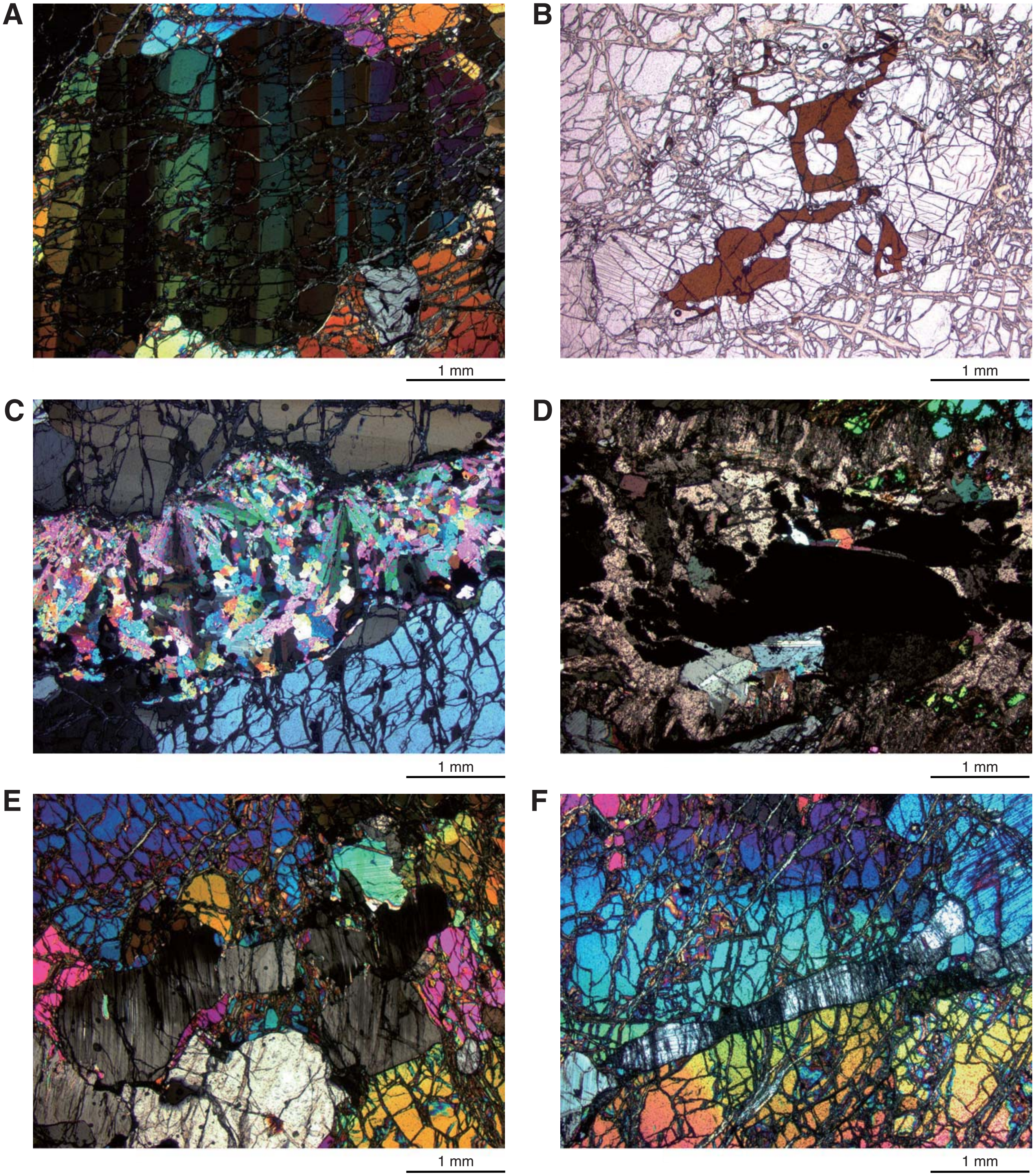

Figure F17. Abundance, composition, and distribution of vesicles (average per core), Hole U1382A.

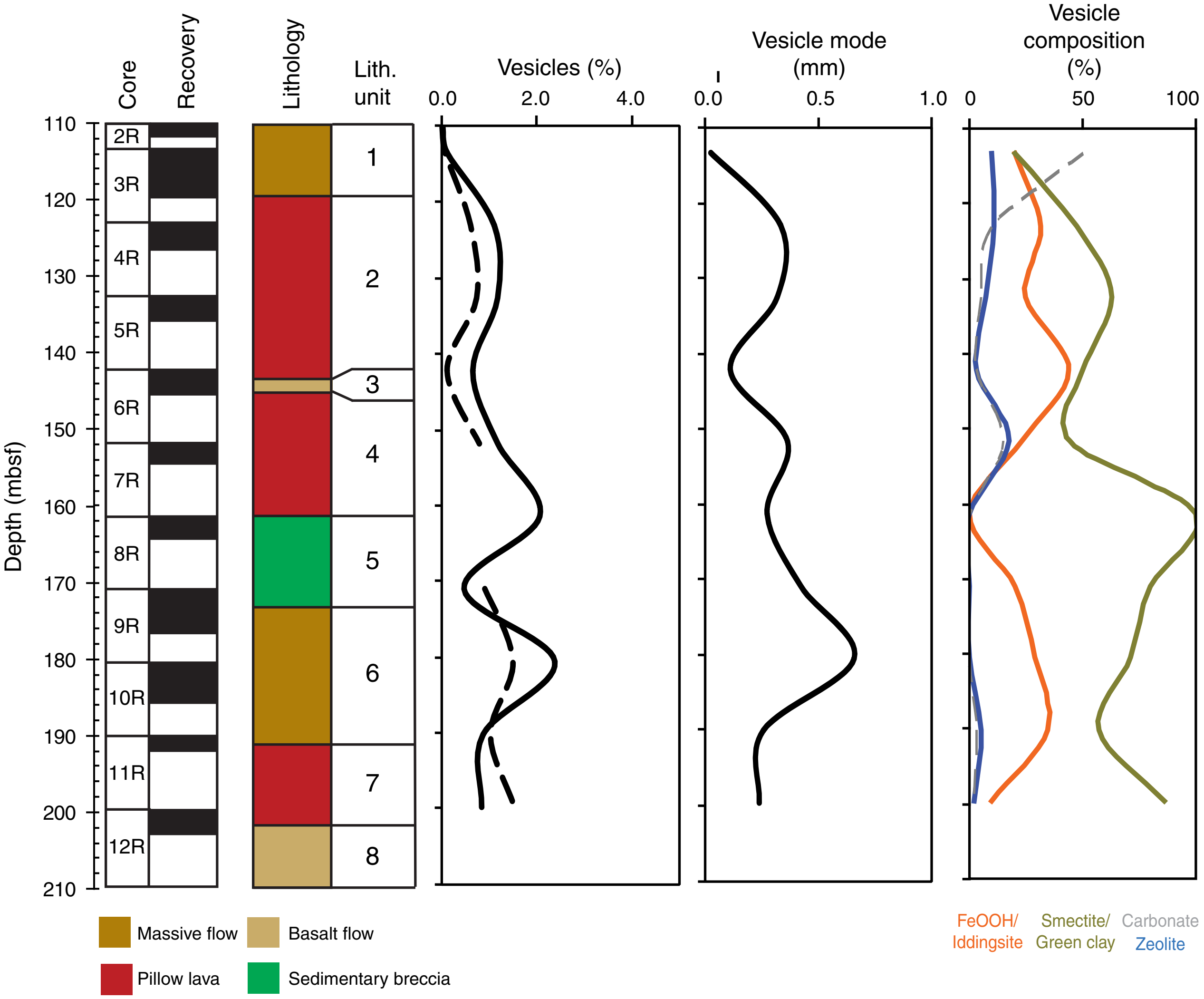

Figure F18. Abundance, composition, and distribution of veins and alteration (average per core), Hole U1382A.

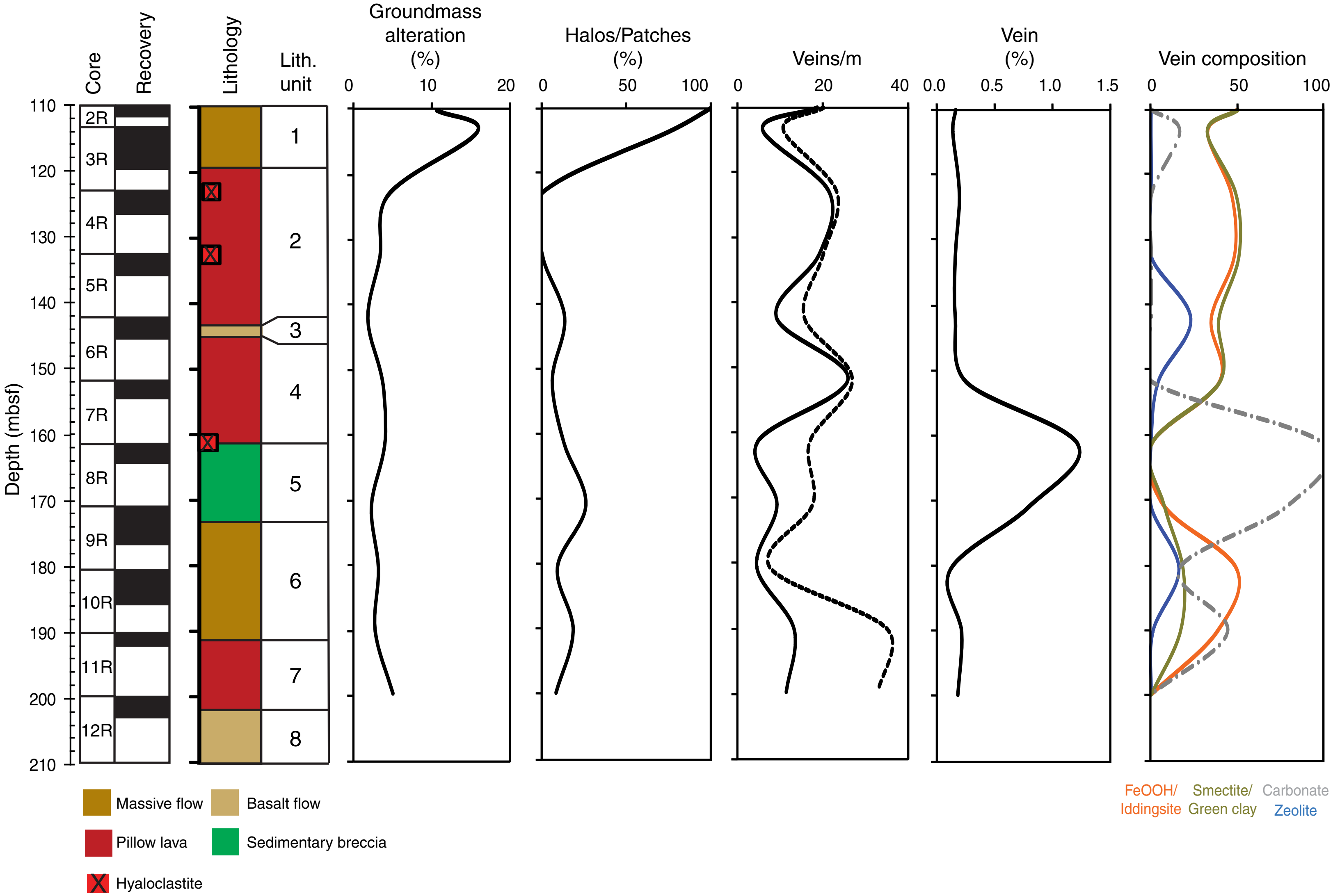

Figure F19. A, B. Binocular microscope photographs (Section 336-U1382A-3R-2 [Piece 12]): (A) open vugs filled by carbonate, (B) pervasively altered fine- to medium-grained basalt with fresh plagioclase laths and iddingsite replacement of olivine microphenocrysts. **C, D.** Photomicrographs of open vugs filled with fan-shaped radiating phillipsite (Sample 336-U1382A-12R-1, 100–104 cm: (C) plane-polarized light, (D) cross-polarized light.

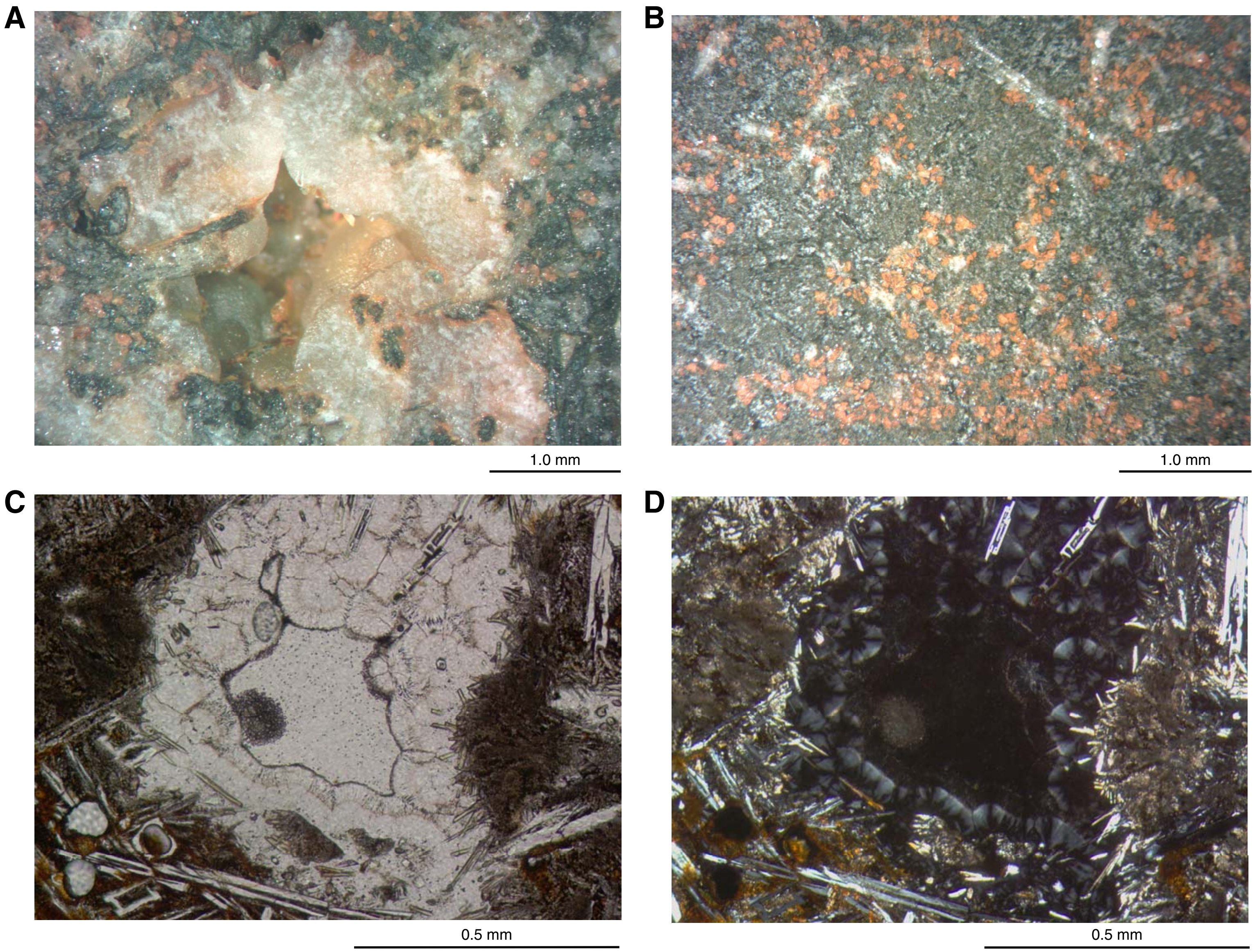

Figure F20. Photomicrographs of composite vesicles from Hole U1382A basalt. **A.** Vesicle (~1 mm in diameter) filled with fibrous carbonate and iddingsite as reddish outer ring (plane-polarized light) (Sample 336-U1382A-7R-1, 76–79 cm). **B.** Vesicle (~0.5 mm in diameter) filled with carbonate (cross-polarized light) (Sample 336-U1382A-9R-3, 20–23 cm). **C.** Multilayered partially filled vesicle, lined with bright orange Fe-rich smectite followed by a saponite band and deep red Fe oxyhydroxide core (plane-polarized light) (Sample 336-U1382A-4R-3, 39–42 cm). **D.** Multilayered partially filled vesicle lined with saponite followed by Fe oxyhydroxide (plane-polarized light) (Sample 336-U1382A-4R-3, 39–42 cm).

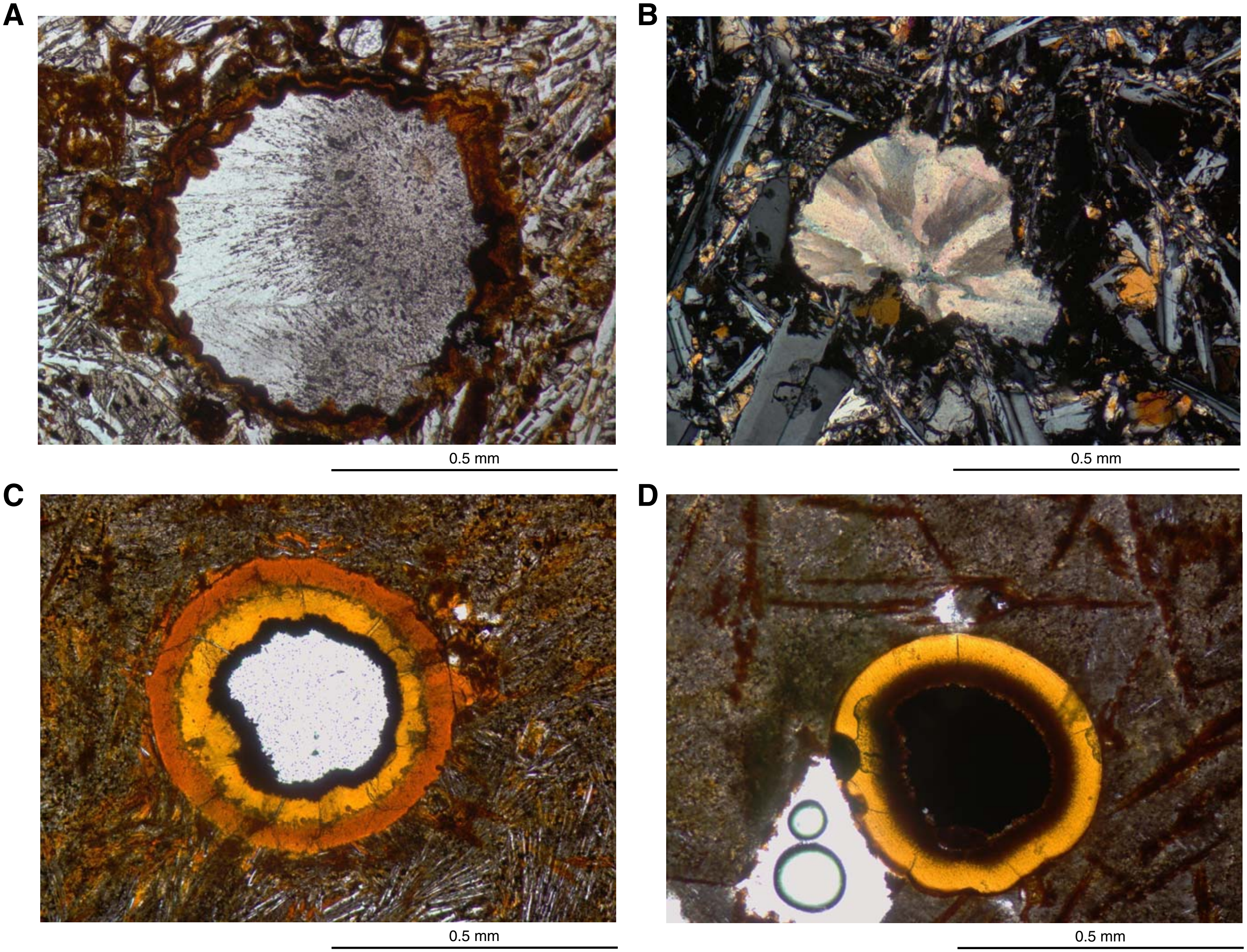

Figure F21. Photomicrographs of composite veins from Hole U1382A basalt. **A.** Irregular and branching vein (500 µm thick) filled with saponite and disseminated opaque spherical pyrite (<10 µm) (plane-polarized light) (Sample 336-U1382A-12R-1, 83–86 cm). **B.** Microvein (<10 µm across) with thin (100 µm) irregular alteration front extending in a subcryptocrystalline (devitrified) mesostasis (plane-polarized light) (Sample 336-U1382A-7R-2, 70–73 cm). **C.** Mixed Fe oxyhydroxide and smectite vein in microcrystalline groundmass, lacking alteration halos (plane-polarized light) (Sample 336-U1382A-5R-3, 29–32 cm). **D.** Smectite vein (0.2 mm thick) in medium-grained basalt composed of fresh plagioclase, clinopyroxene, and Ti-magnetite and partially altered olivine and interstitial mesostasis (plane-polarized light) (Sample 336-U1382A-12R-3, 35–38 cm).

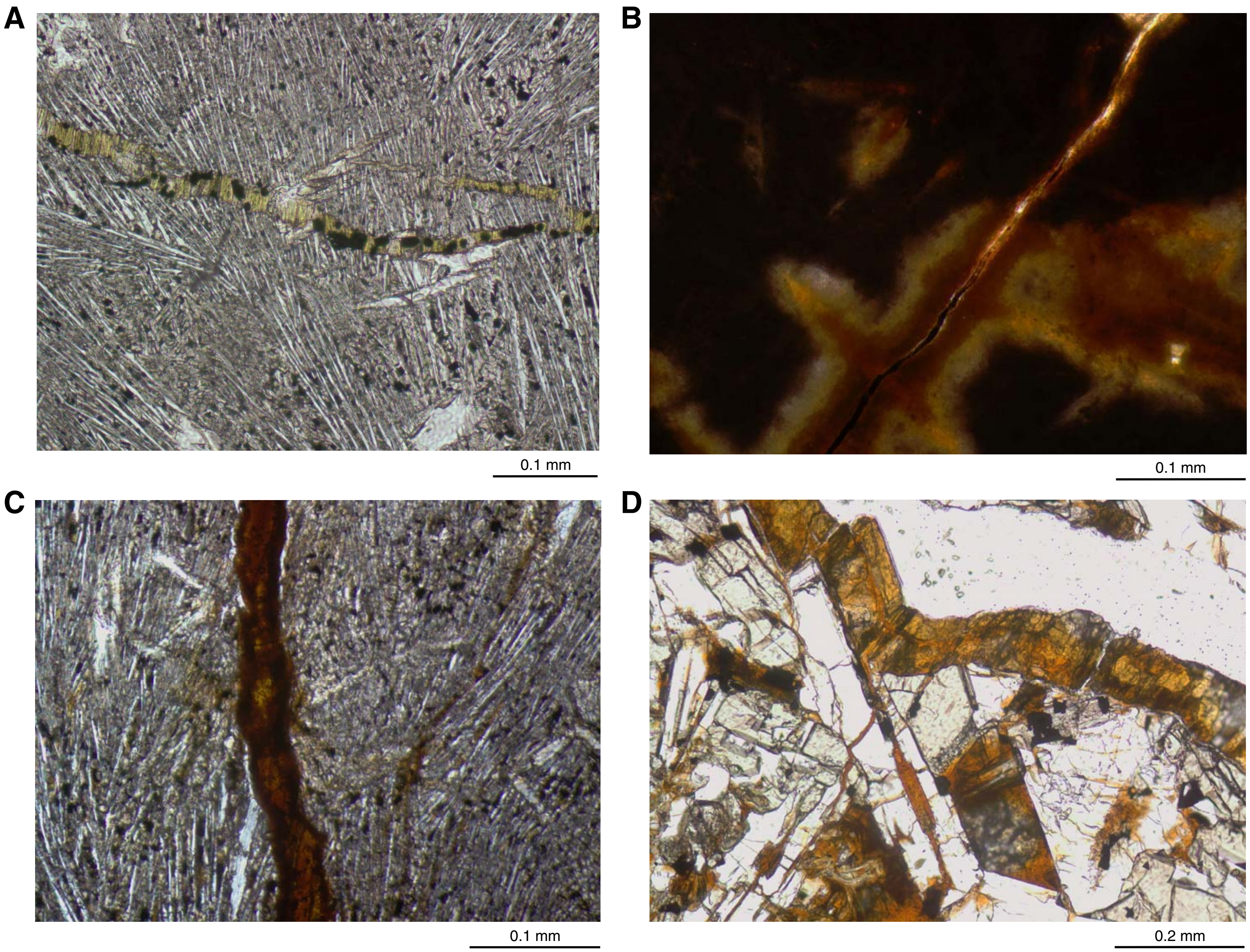

Figure F22. Downhole variations of Al_2O_3, $Fe_2O_3^T$, weight loss on ignition (LOI), and total carbon content, Hole U1382A. Dashed lines and shaded area represent unit boundaries and sedimentary breccia unit, respectively. $Fe_2O_3^T$ = total iron as Fe_2O_3.

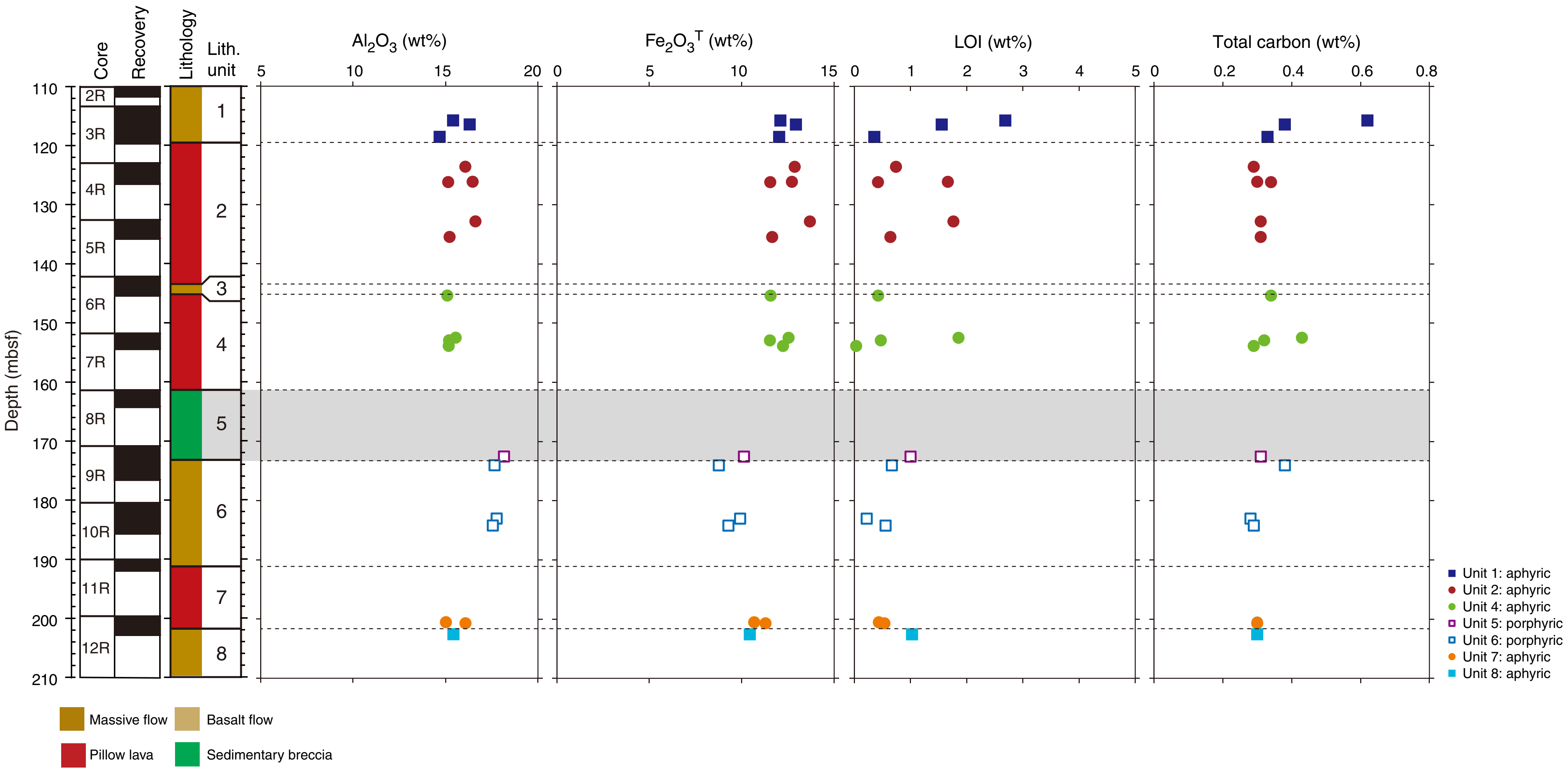

Figure F23. Plots of Al_2O_3 vs. MgO, CaO vs. Al_2O_3, and Sr vs. CaO for basaltic rock samples, Hole U1382A. Data for aphyric and porphyritic basalts from corresponding depths in Hole 395A (Rhodes et al., 1979; Bougault et al., 1979) are also shown for comparison. The possible olivine fractionation and plagioclase accumulation lines are for illustrative purposes only and are not intended as lines of best fit or to imply that the basalts are related simply by olivine and plagioclase fractionation.

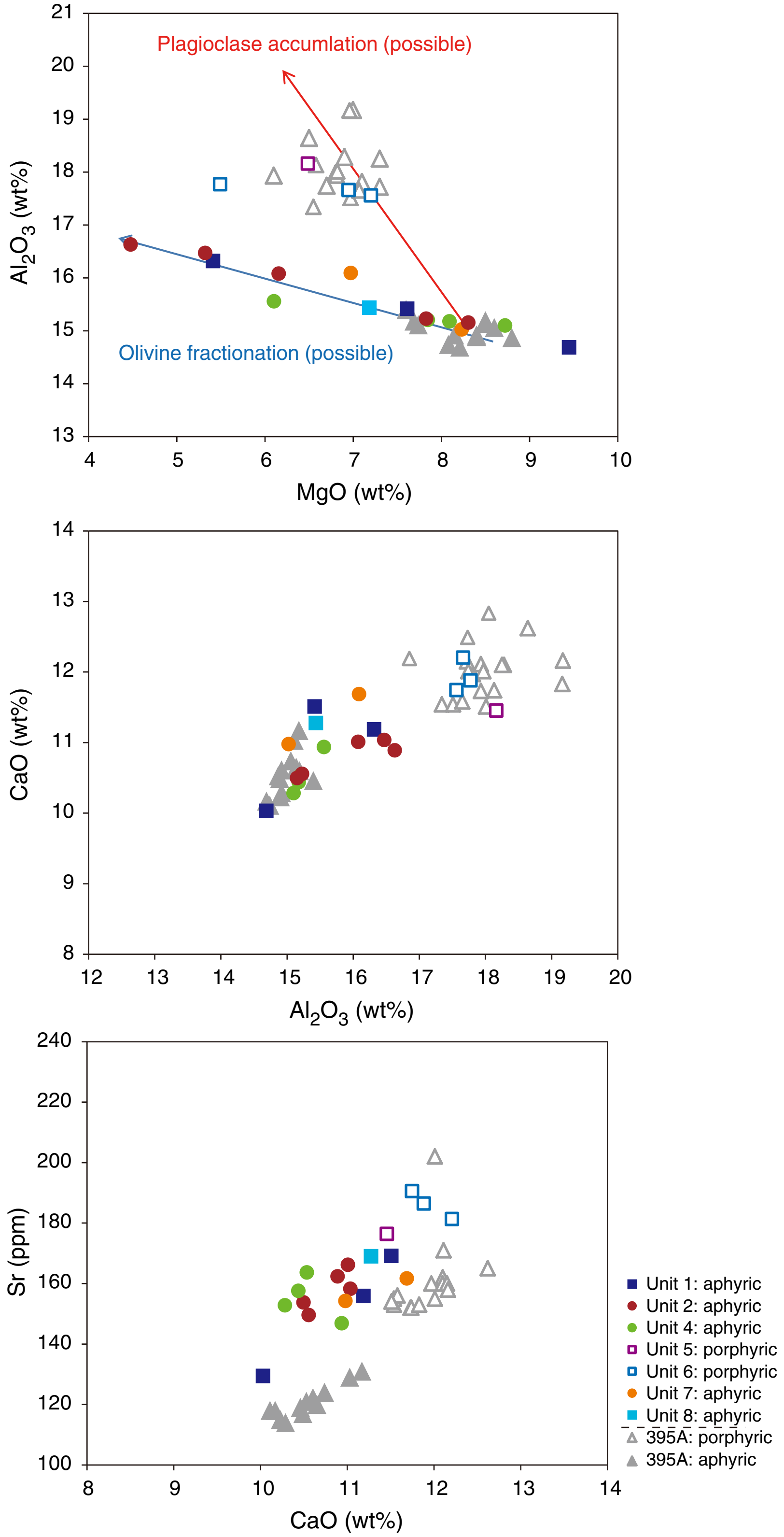

Figure F24. Plots of MgO vs. $Fe_2O_3^T$ and TiO_2 for basaltic rock samples, Hole U1382A. Data for aphyric and porphyritic basalts from corresponding depths in Hole 395A (Rhodes et al., 1979; Bougault et al., 1979) are also shown for comparison. The possible olivine fractionation and plagioclase accumulation lines are for illustrative purpose only and are not intended as lines of best fit or to imply that the basalts are related simply by olivine and plagioclase fractionation. $Fe_2O_3^T$ = total iron as Fe_2O_3.

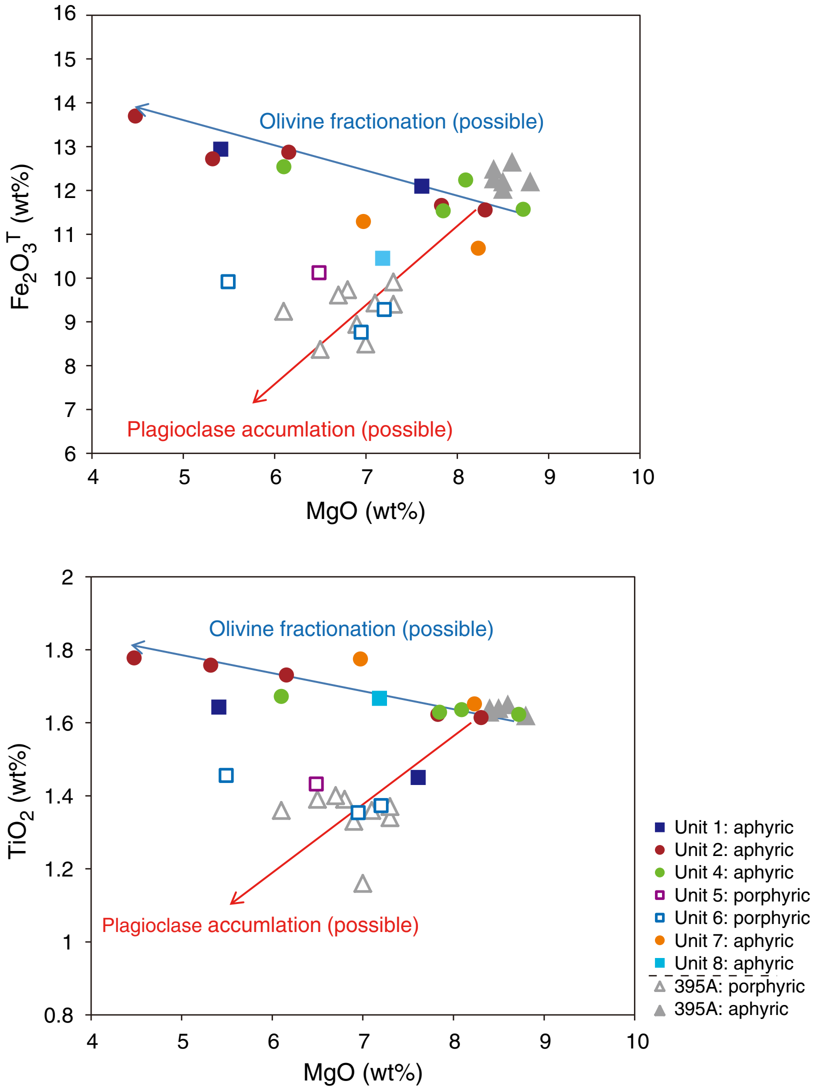

Figure F25. Plots of $Fe_2O_3^T$ vs. Cr, Sc, V, and Y for basaltic rock samples, Hole U1382A. Data for aphyric and porphyritic basalts from corresponding depths in Hole 395A (Rhodes et al., 1979; Bougault et al., 1979) are also shown for comparison. $Fe_2O_3^T$ = total iron as Fe_2O_3.

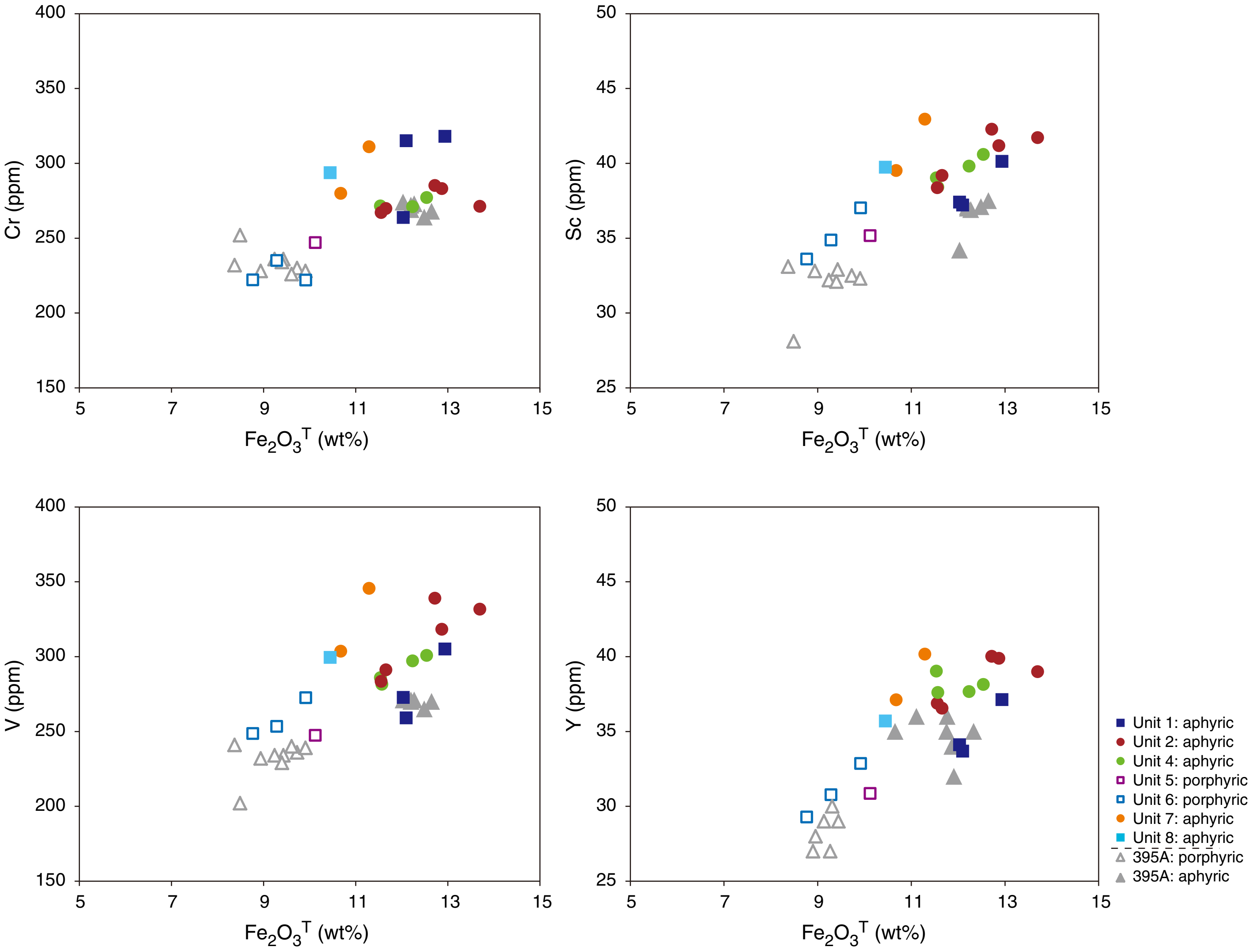

Figure F26. Plots of Zr vs. Y and TiO_2 for basaltic rock samples, Hole U1382A. Different trends for shallower and deeper units suggest the difference of parental magmas between these two units.

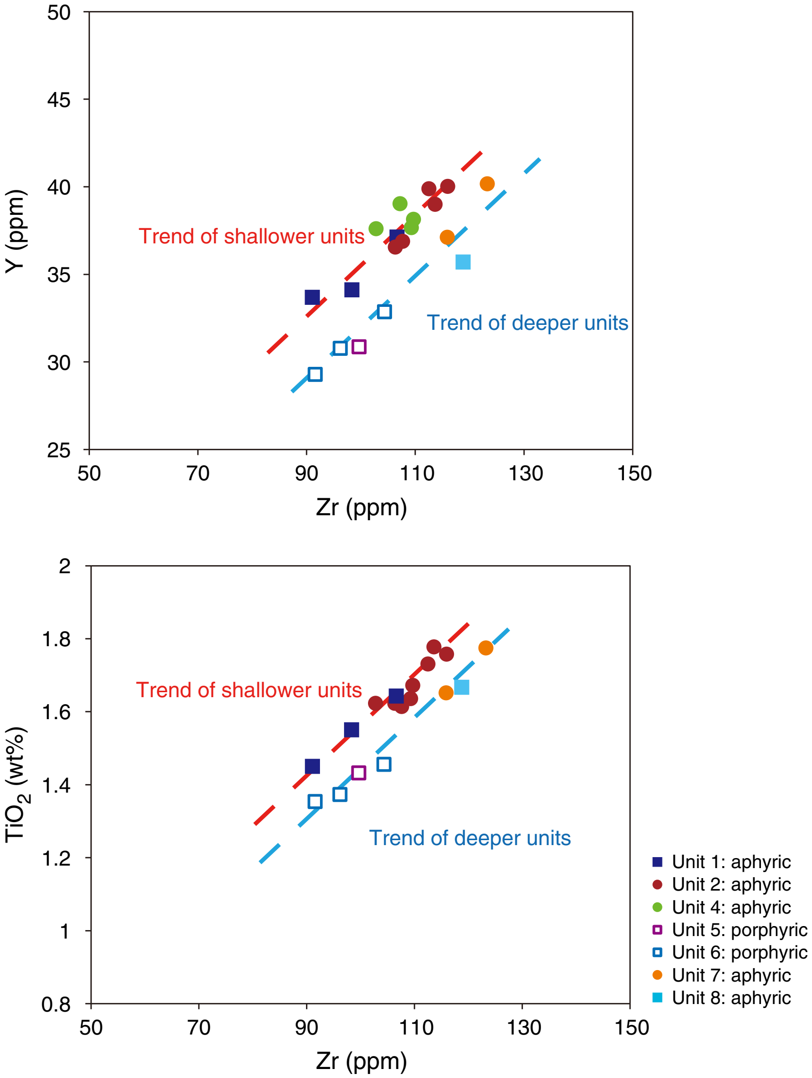

Figure F27. Bar chart showing average compositions of altered samples normalized by those of the least altered samples, Hole U1382A. Values < 1 indicate depletion and vice versa. Gray areas represent the compositional range (±1σ) of the least altered samples. $Fe_2O_3^T$ = total iron as Fe_2O_3. LOI = loss on ignition.

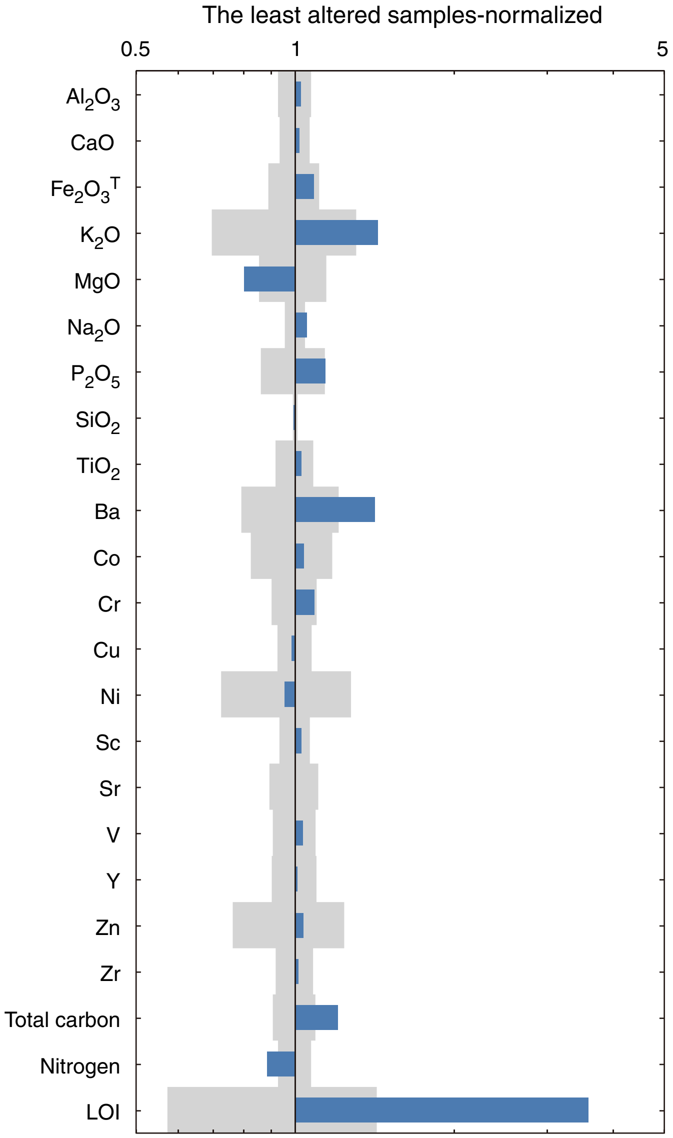

Figure F28. Plots of weight loss on ignition (LOI) vs. K_2O and Ba and Ba vs. K_2O for basaltic rock samples, Hole U1382A.

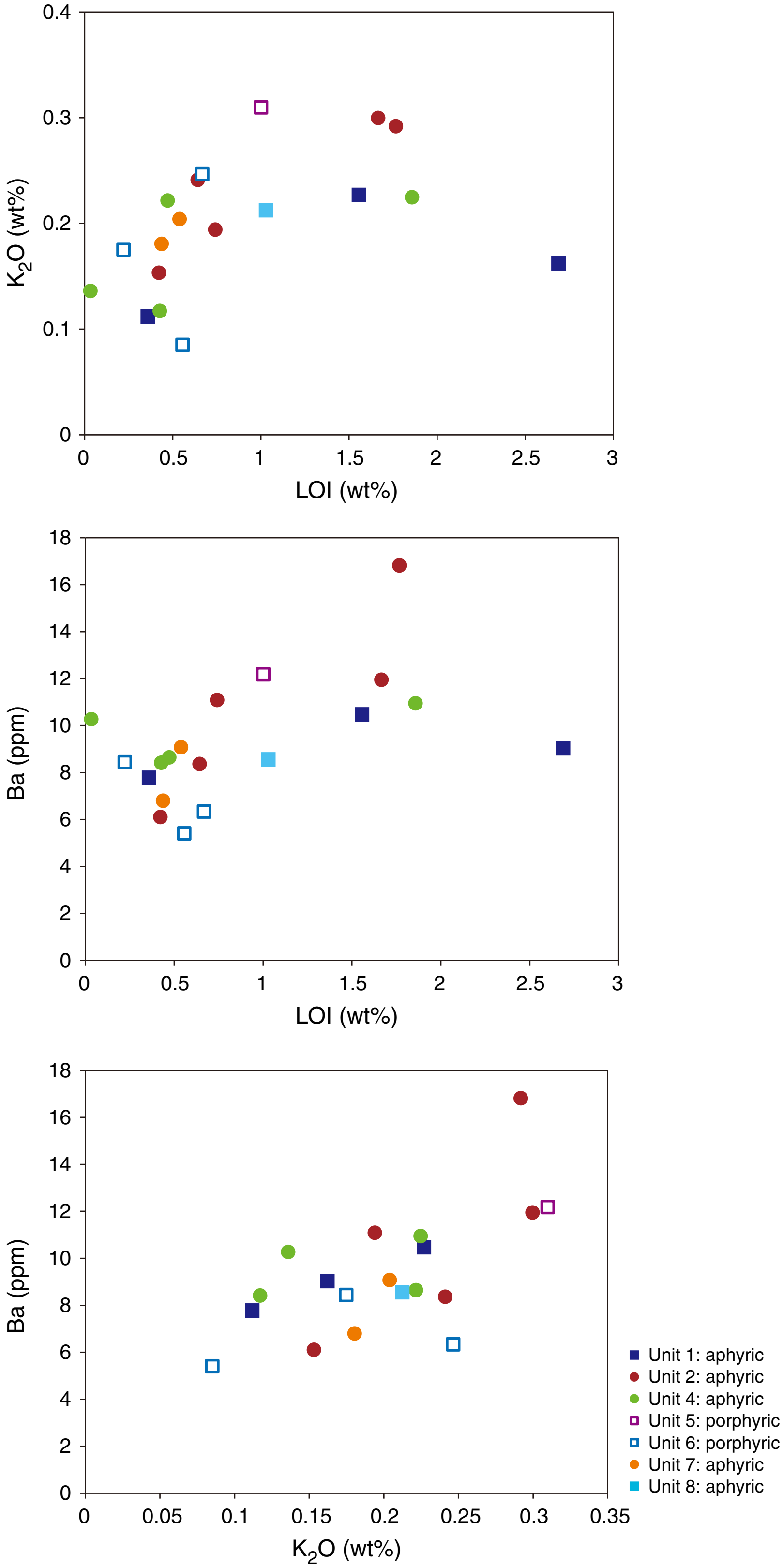

Figure F29. Nannofossil assemblages, Hole U1382A. **A.** Sample 336-U1382A-8R-2, 13–14 cm (ooze). **B.** Sample 336-U1382A-8R-3, 7–8 cm (ooze). **C.** Sample 336-U1382A-8R-4, 15–16 cm (ooze). **D.** Sample 336-U1382A-8R-4, 37–38 cm (polymict breccia).

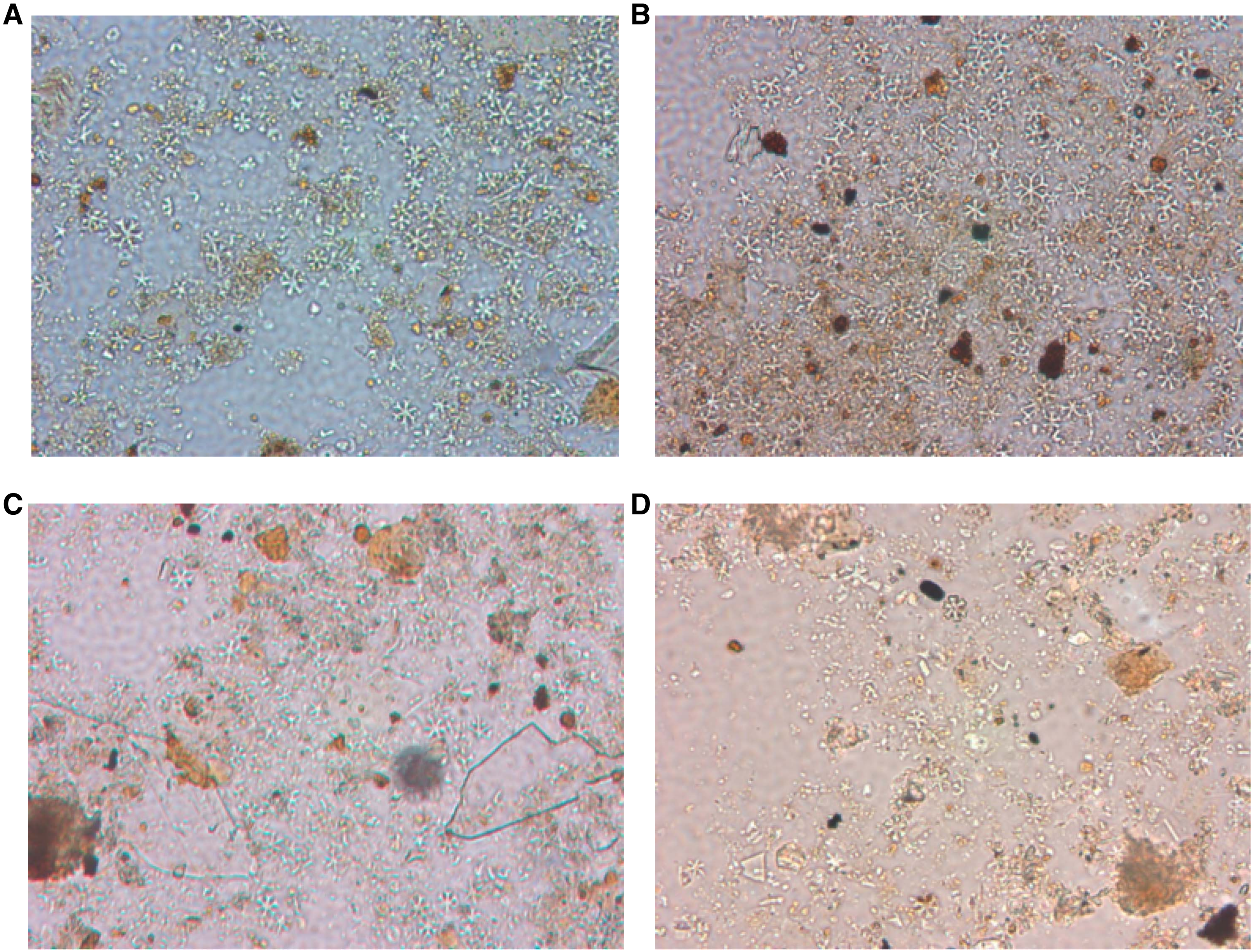

Figure F30. Other microfossils, Hole U1382A. **A.** Altered planktonic foraminifer (center) with background of nannofossils from Sample 336-U1382A-8R-2, 13–14 cm (ooze). **B.** Altered planktonic foraminifer (center) and amorphous matter with background of nannofossils from Sample 336-U1382A-8R-3, 7–8 cm (ooze). **C.** Partly dissolved radiolarian (center) and amorphous matter from Sample 336-U1382A-8R-4, 24–25 cm (ooze). **D.** Altered dinoflagellate (center) and amorphous matter with background of nannofossils from Sample 336-U1382A-8R-4, 24–25 cm (ooze).

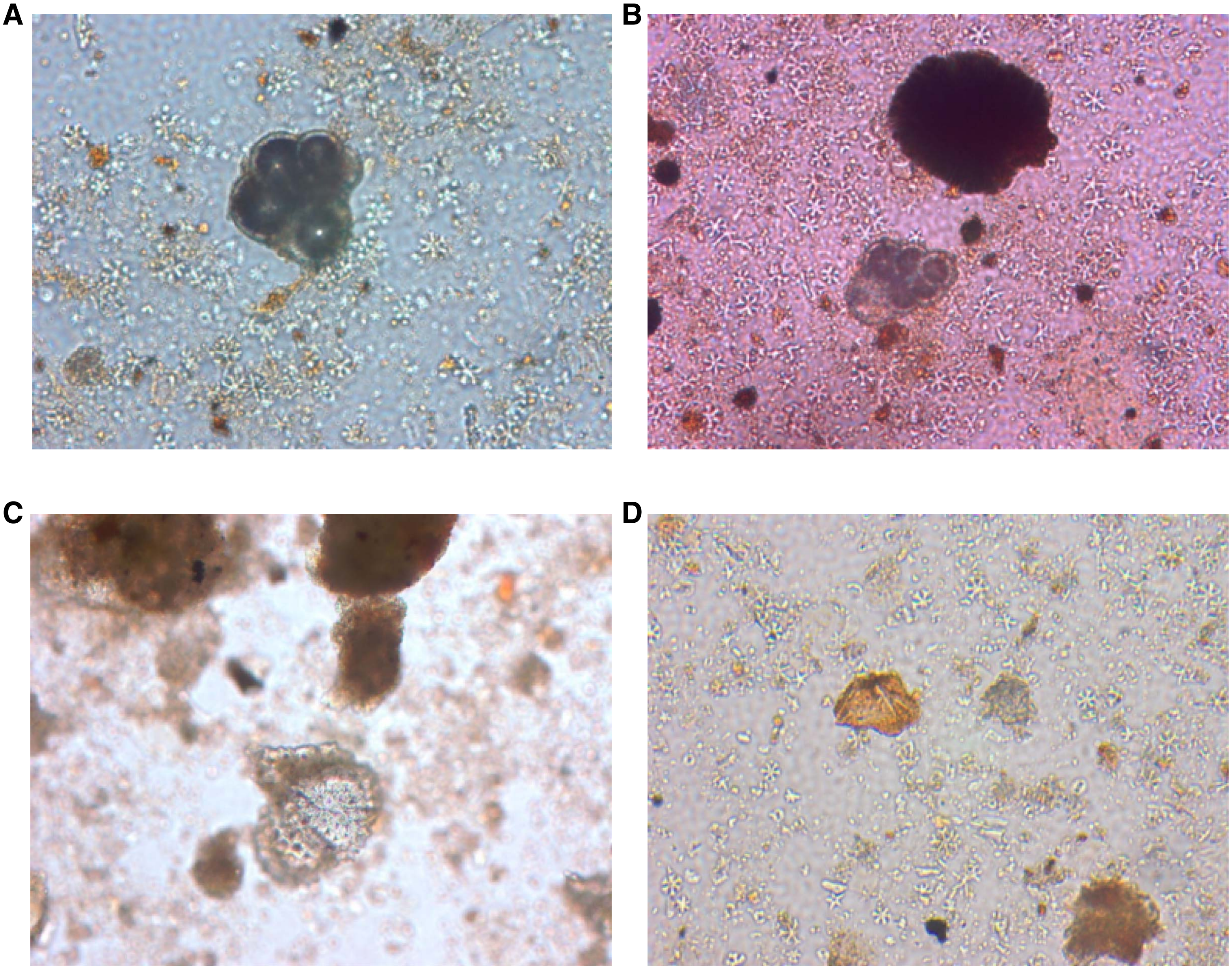

Figure F31. DEBI-pt scanning image of subsample of Sample 336-U1382A-10R-3-MBIOD. **A.** Visible image showing broken plagioclase-olivine-phyric fine-grained basalt. Clay and Fe oxyhydroxides partially replace olivine grains and fill vugs. **B.** Fluorescence image showing the presence of altered material (maroon) and bacteria (green). The bacteria are heterogeneously distributed and are localized to the iron oxides. They appear to be concentrated in the lowermost part of the rock, which features a crack and is noticeably vuggy. Scale bar = 10 mm.

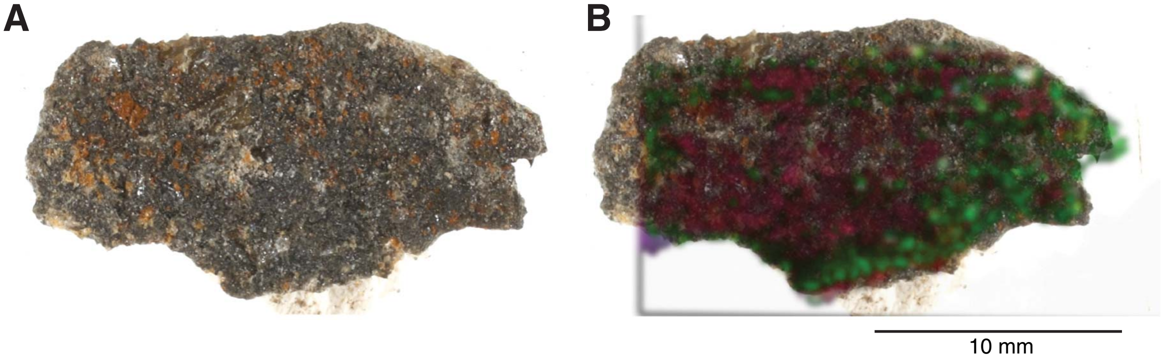

Figure F32. Gamma ray attenuation (GRA) density and moisture and density (MAD) measurements, Hole U1382A. **A.** GRA bulk density and density from discrete measurements. Gray intensity indicates more intense filtering. **B.** Bulk, dry, and grain densities calculated for discrete samples. **C.** Porosity. **D.** Void ratio.

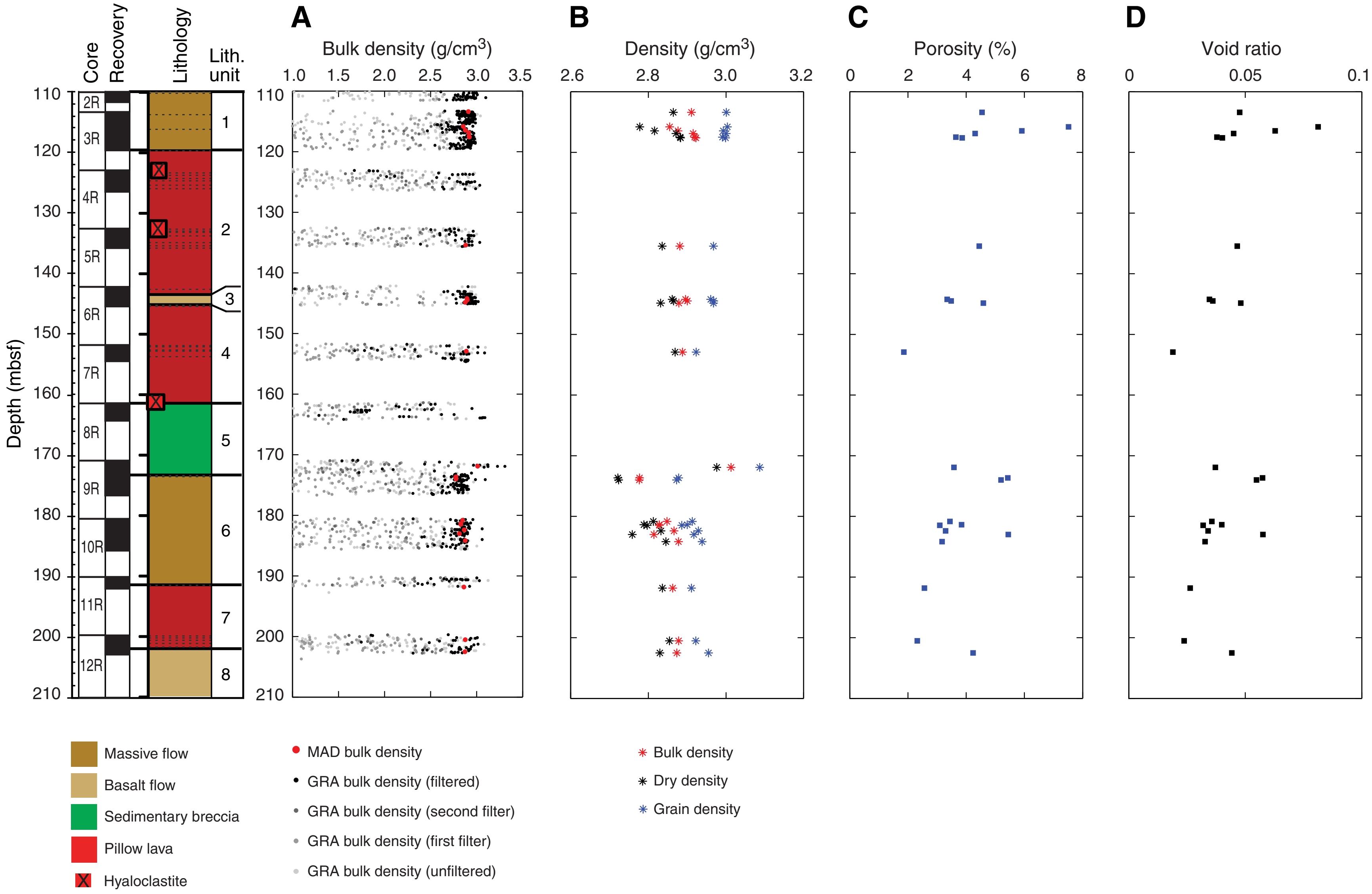

Figure F33. Whole-round and point magnetic susceptibility, Hole U1382A. Gray intensity indicates more intense filtering.

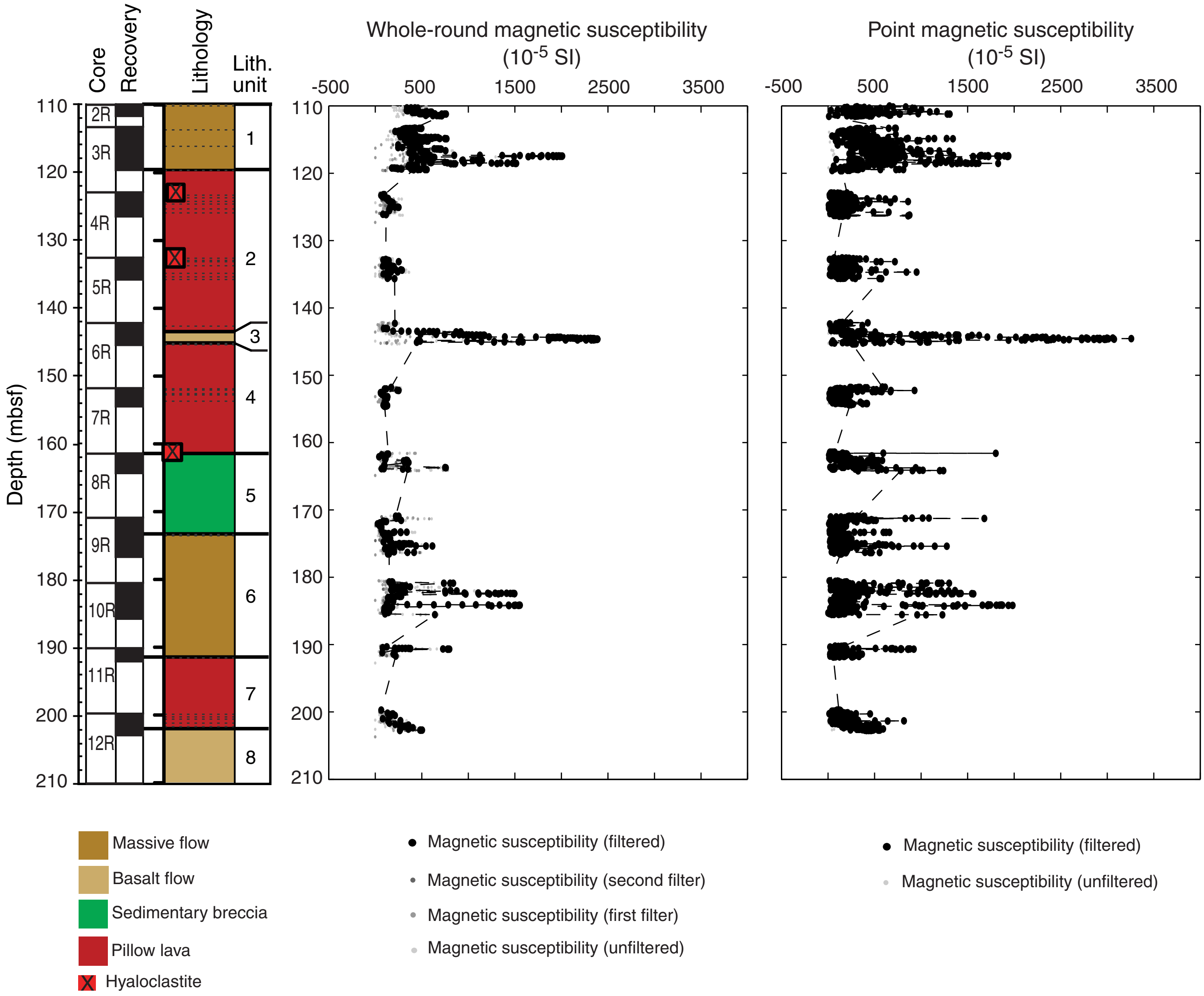

Figure F34. Natural gamma radiation (NGR) total counts per second (cps) and potassium percentage based on NGR and inductively coupled plasma–atomic emission spectroscopy (ICP-AES) values, Hole U1382A.

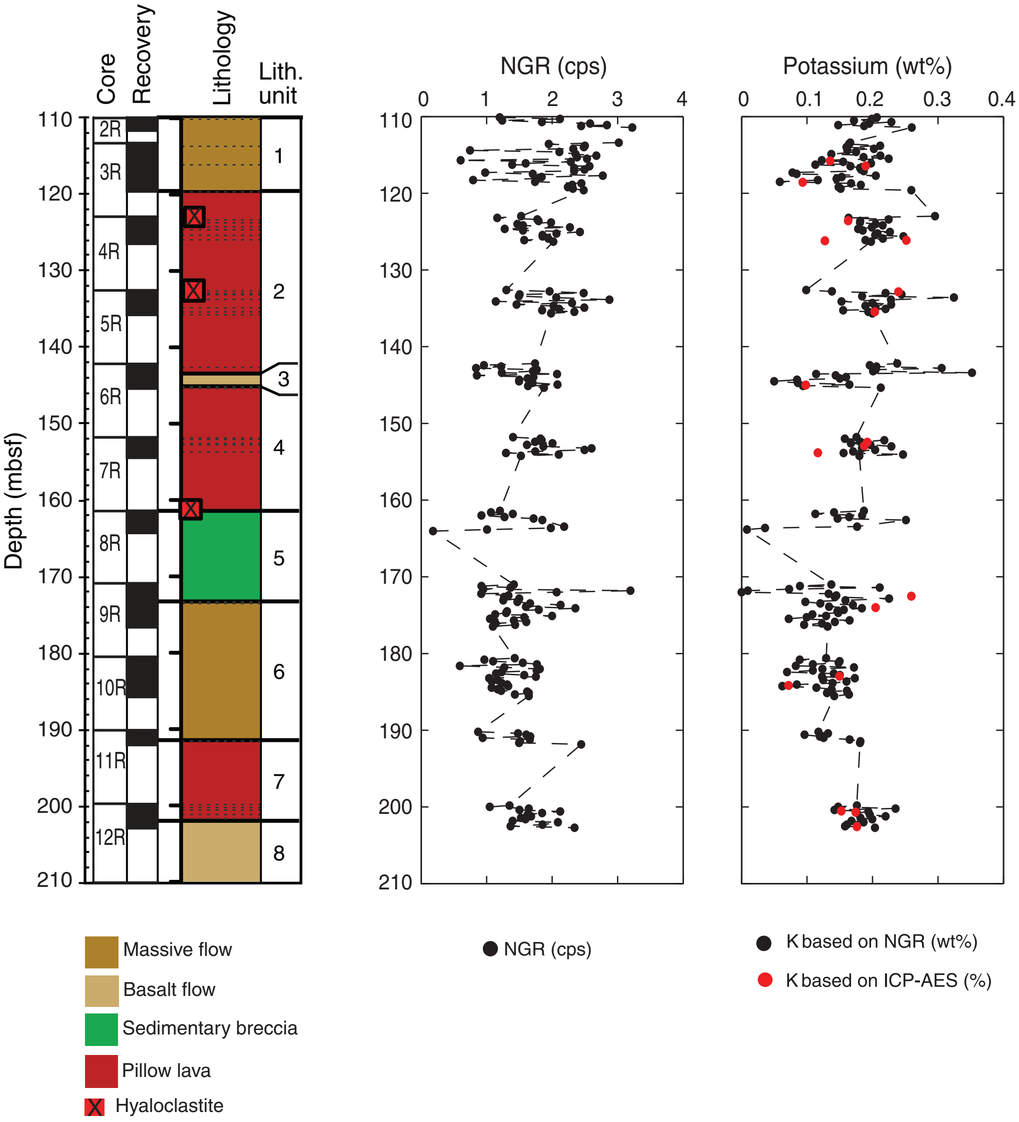

Figure F35. Summary of natural gamma ray log measurements, Hole U1382A. Note that gamma ray measurements are in gAPI. Measurements include total gamma ray (TGR), potassium abundance, thorium, and uranium. FMS p2, FMS p1, and FMS dl = FMS-HNGS Pass 2, Pass 1, and downlog, respectively. K core = from NGR measured on the cores.

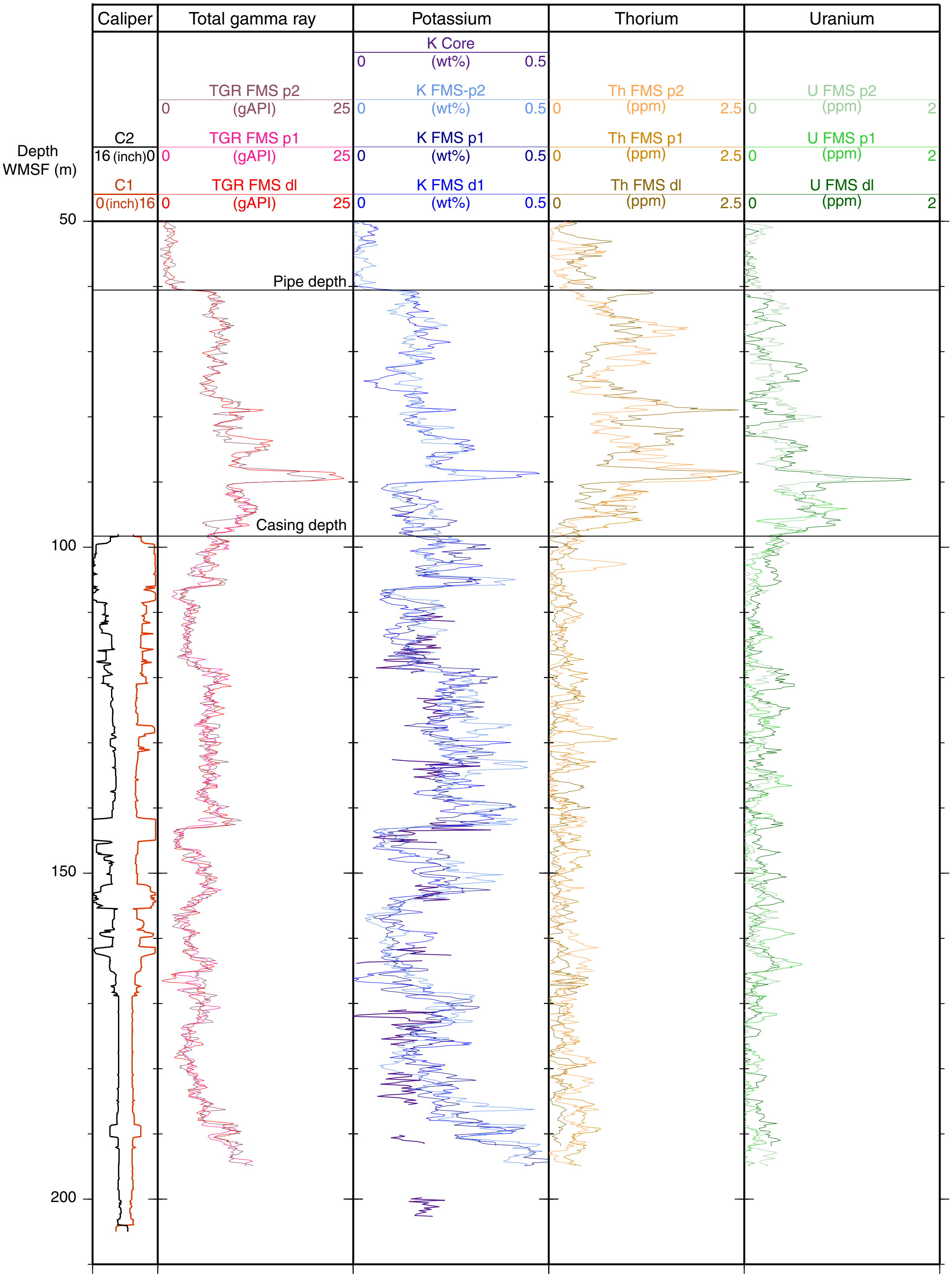

Figure F36. Compressional *P*-wave velocity measurements for *x*-, *y*-, and *z*-axes and percentage of alteration, Hole U1382A.

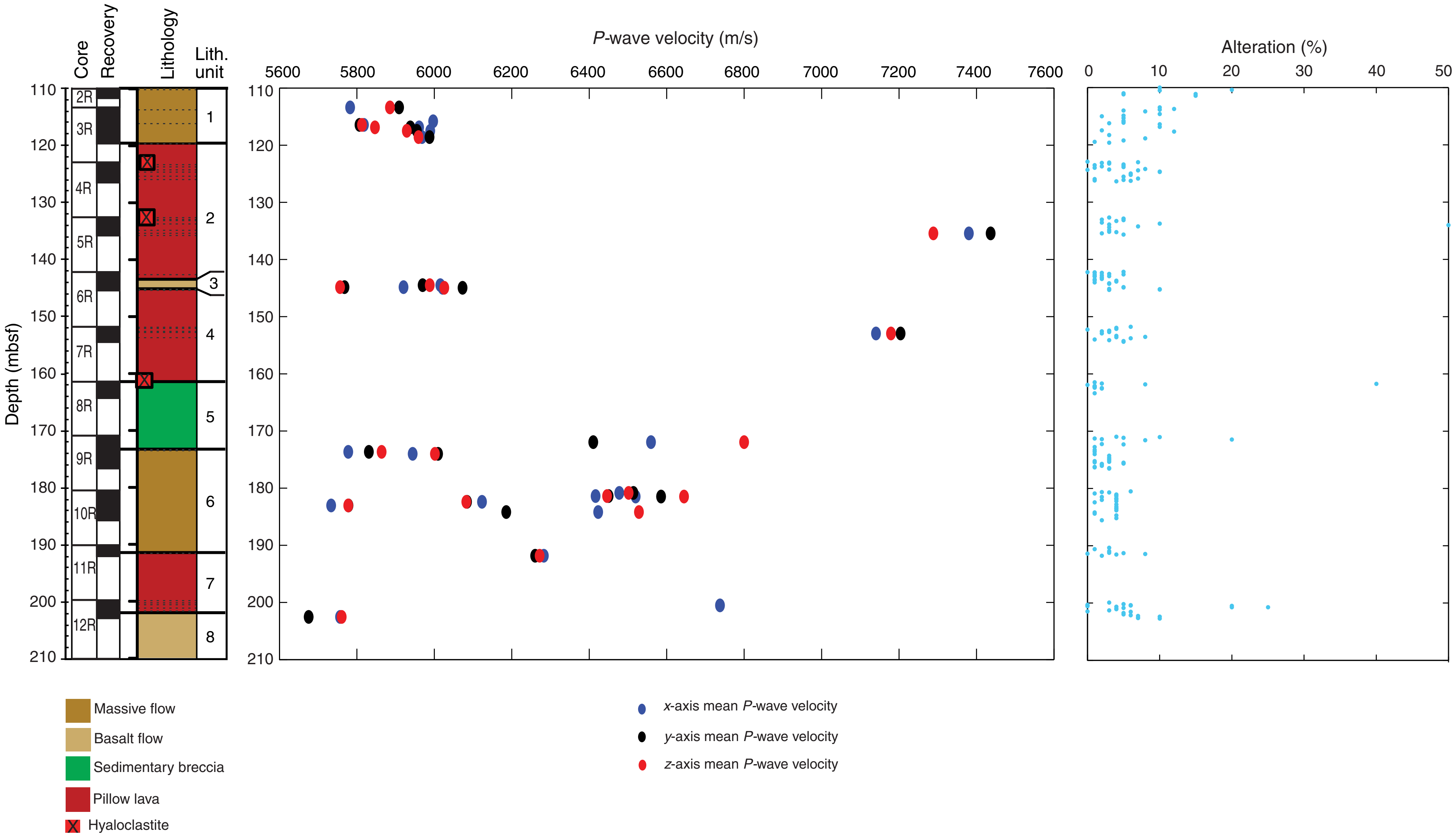

Figure F37. Velocity as a function of porosity, Hole U1382A.

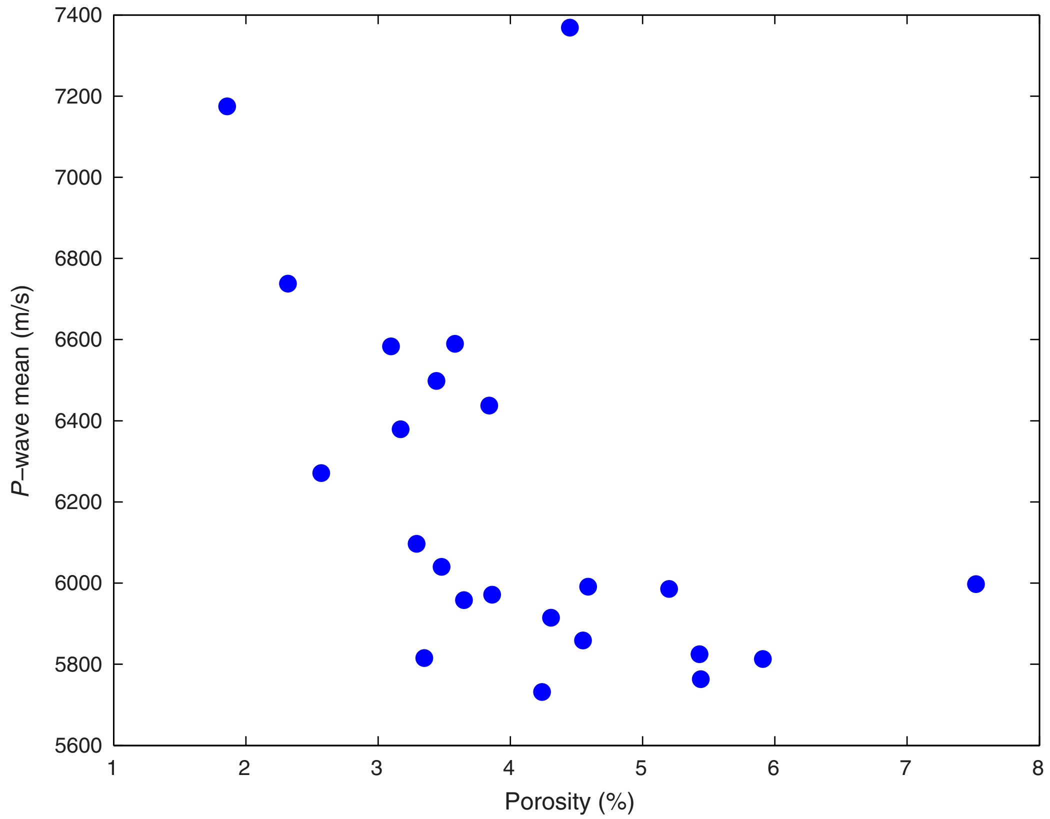

Figure F38. Thermal conductivity values, Hole U1382A.

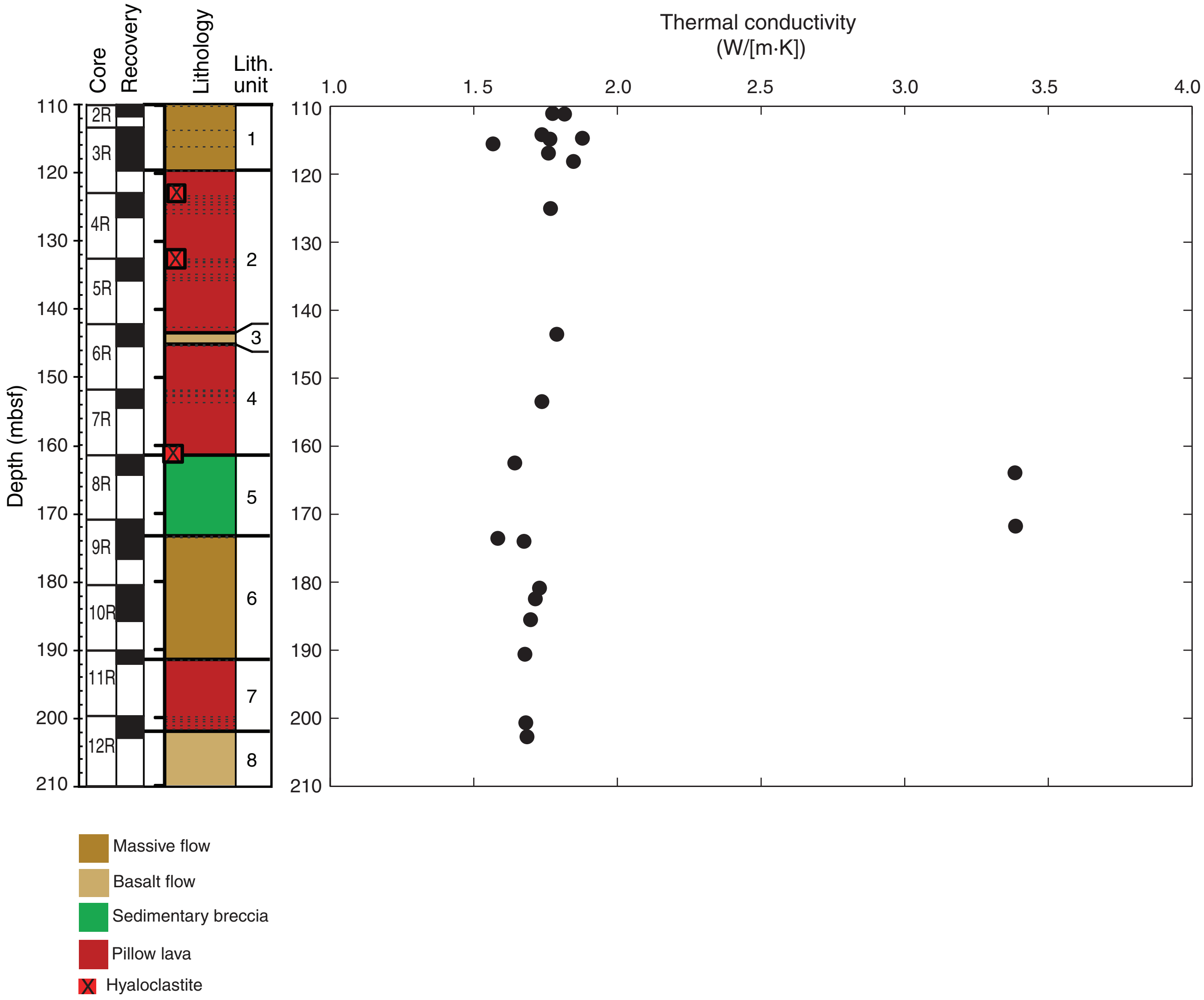

Figure F39. Color reflectance and tristimulus axes values, Hole U1382A. L*, a* (green = negative values, red = positive values), b* (blue = negative values, yellow = positive values), and a*/b*.

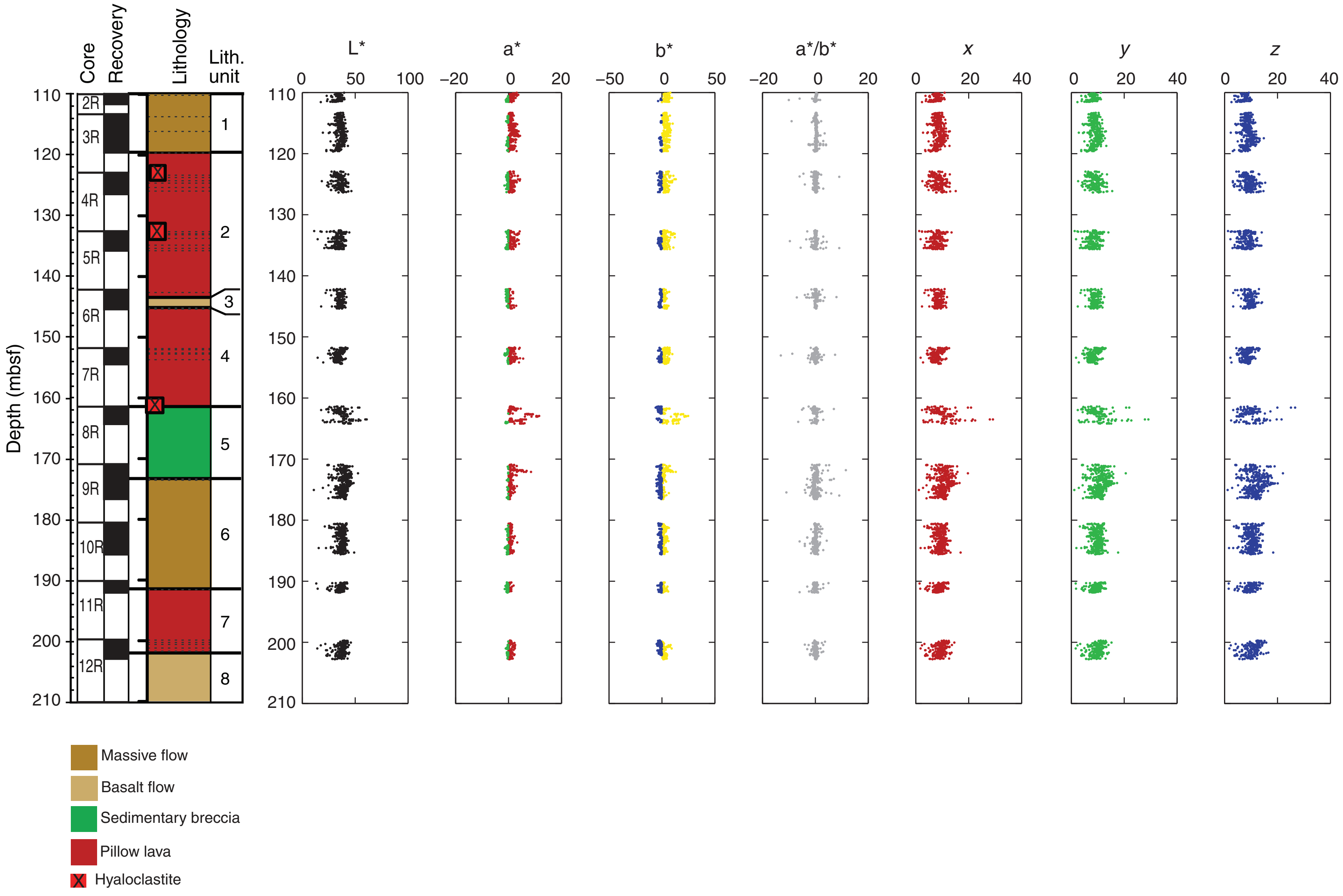

Figure F40. **A.** Adapted microbiology combination I tool string. LEH-MT = logging equipment head-mud temperature, EDTC = Enhanced Digital Telemetry Cartridge (gamma ray), HLDS = Hostile Environment Litho-Density Sonde, HRLA = High-Resolution Laterolog Array, ELIC = EFTB-Lamont Interface Cartridge, MFTM = Multifunction Telemetry Module, DEBI-t = Deep Exploration Biosphere Investigative tool. **B.** Schematic of Hole U1382A logging passes (a downlog from just above casing and an uplog to ~20 m below casing).

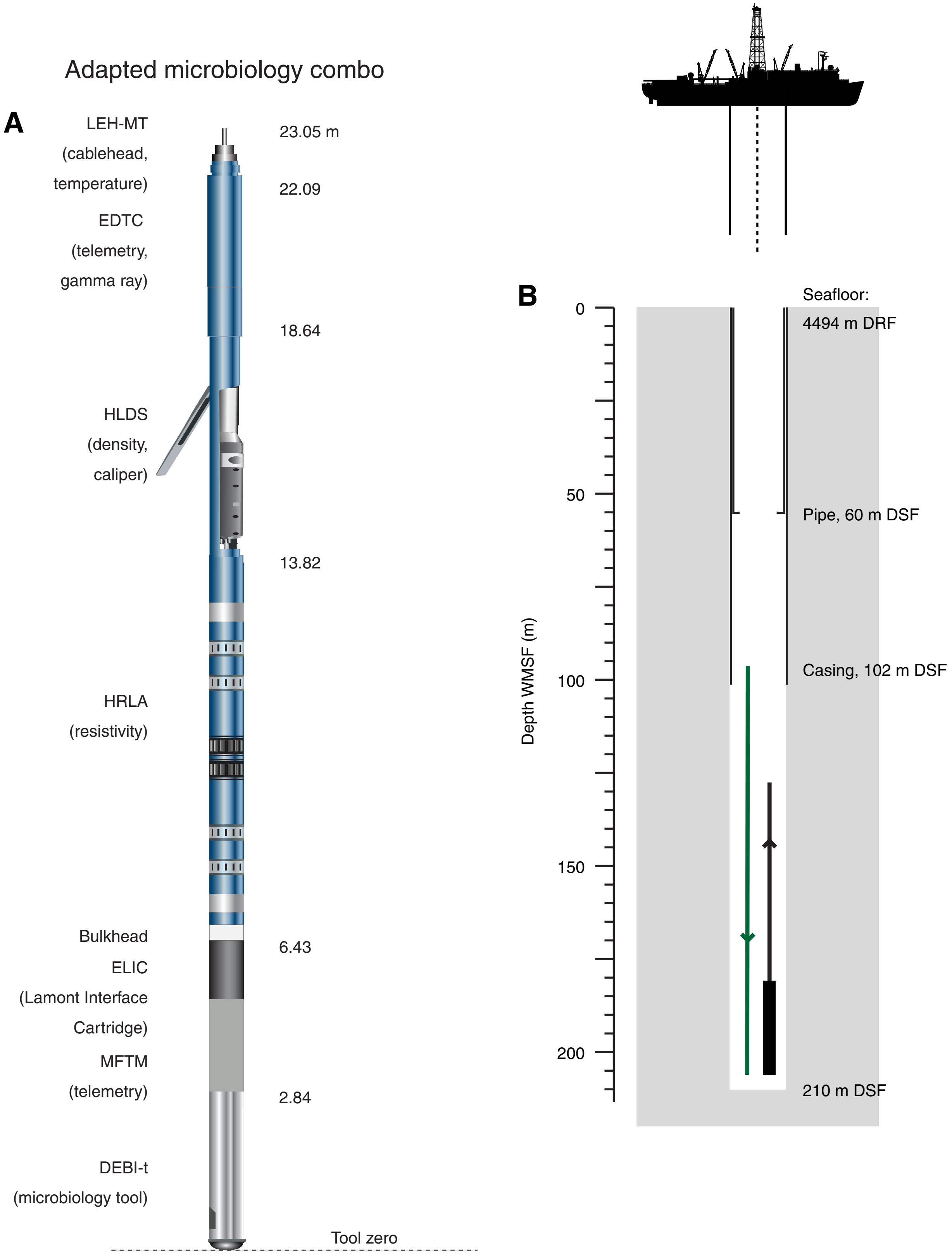

Figure F41. **A.** Formation MicroScanner (FMS)–Hostile Environment Natural Gamma Ray Sonde (HNGS) tool string. EDTC = Enhanced Digital Telemetry Cartridge, GPIT = General Purpose Inclinometry Tool. **B.** Schematic of Hole U1382A logging passes (two uplog passes).

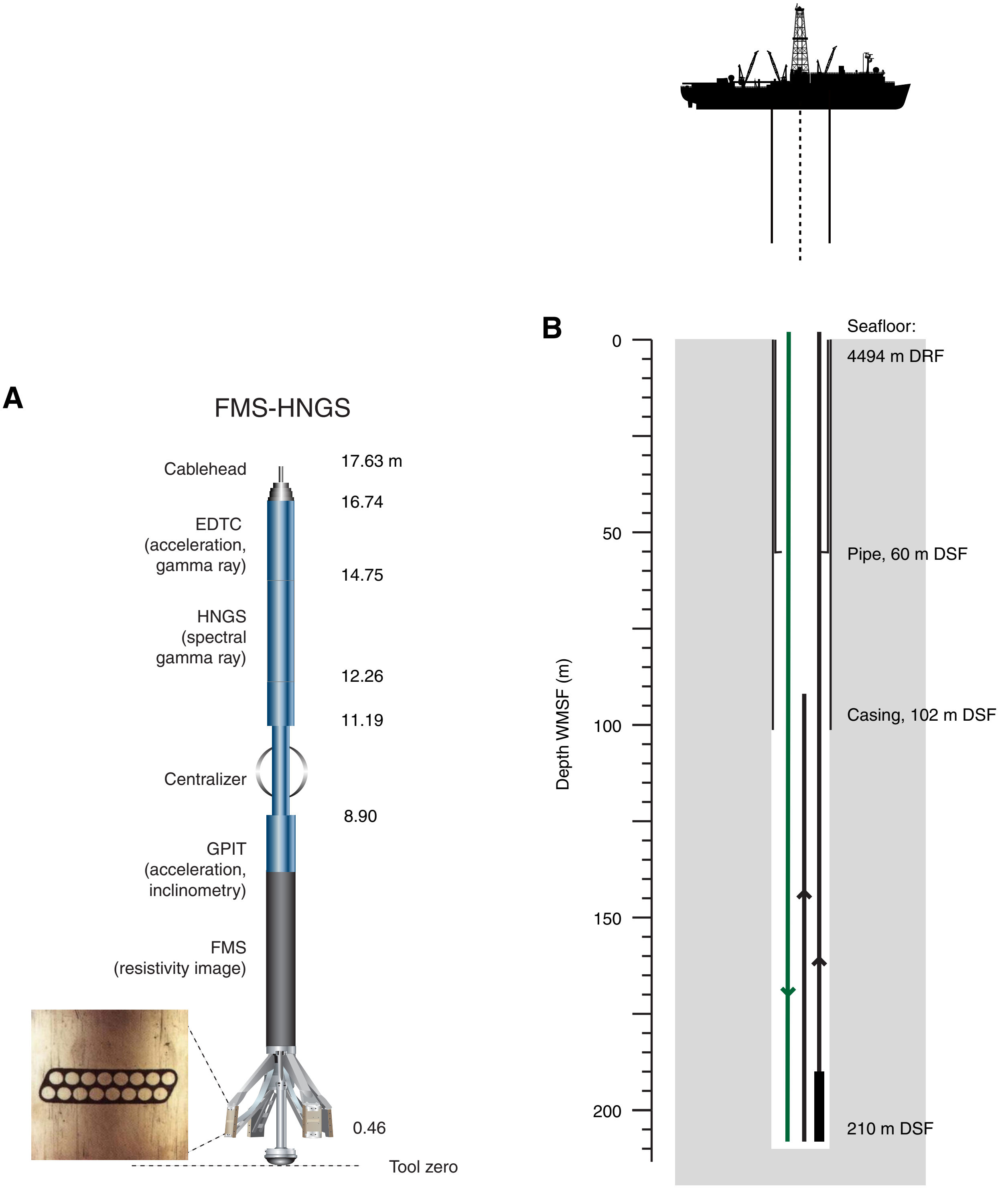

Figure F42. Summary of Hole U1382A logging results. Blue lines = log unit divisions, black lines = limits of pipe and casing. Measurements include borehole diameter (C1, C2 = FMS Pass 1; CALI = AMC I uplog), total gamma ray (TGR; FMS p2, FMS p1 = from FMS-HNGS Pass 1, Pass 2; FMS DL = from FMS-HNGS downlog; EDTC DL = from AMC I downlog), density (bulk density = from AMC I uplog, bulk density H = high-resolution data from AMC I uplog, MAD = moisture and density testing on discrete samples), resistivity (RLA5 UL, RLA5 DL = deepest resistivity from AMC I uplog, downlog; RLA4 UL and RLA4 DL = deep resistivity from AMC I uplog, downlog), and temperature (Temp UL, Temp DL = temperature from LEH-MT sensor on AMC I uplog, downlog). A summary of core recovery and lithologic units is provided at the far left (see Fig. F3 for full explanation).

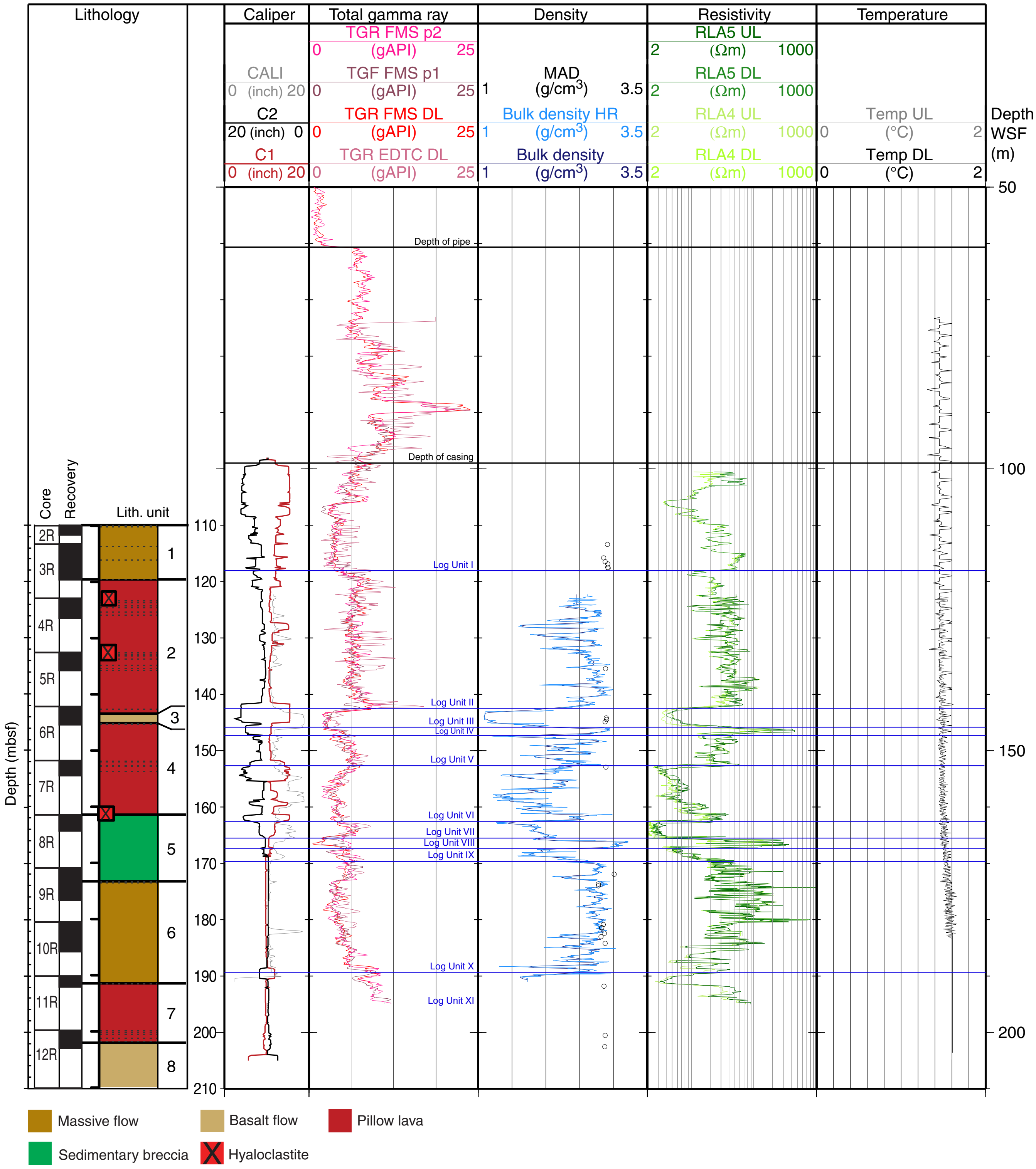

Figure F43. Comparison of total gamma ray (TGR), Holes U1382A and 395A. Measurements include Hole U1382A borehole diameter (C1 and C2 from Formation MicroScanner [FMS] Pass 1), Hole U1382A TGR (FMS DL, FMS p1, and FMS p2 = FMS-HNGS downlog, Pass 1, and Pass 2, respectively), Hole 395A borehole diameter (C1 and C2 from FMS Pass 2 [Leg 174B]), Hole 395A TGR (174B ARI = from Azimuthal Resistivity Imager [Leg 174B]; 174B DIT = from Dual Induction Tool [Leg 174B]; 395A 2U2 = from microbiology combo Run 2, Uplog 2 [Expedition 336]; 395A 2D1 = from microbiology combo Run 2, Downlog 1 [Expedition 336]). At far right is the electrofacies (EFA) log for Hole 395A (after Bartetzko et al., 2001) and units defined for Hole U1382A using FMS electrical images. Dashed lines = correlation lines between main features in TGR curves. Note that gamma ray from Hole U1382A has been correlated to open-hole gamma ray data collected during Leg 174B.

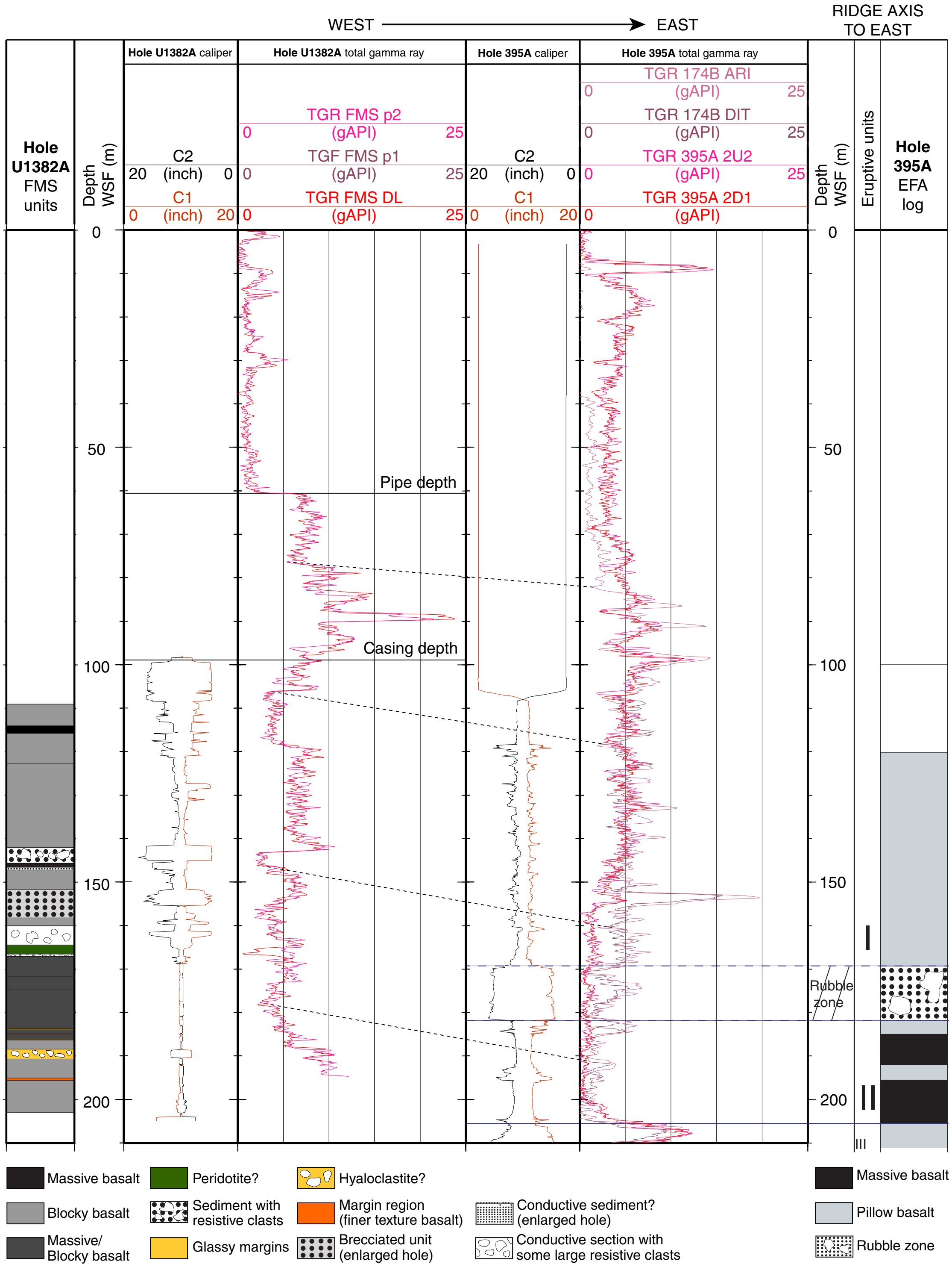

Figure F44. DEBI-t photon intensity data from Hole U1382A downlog.

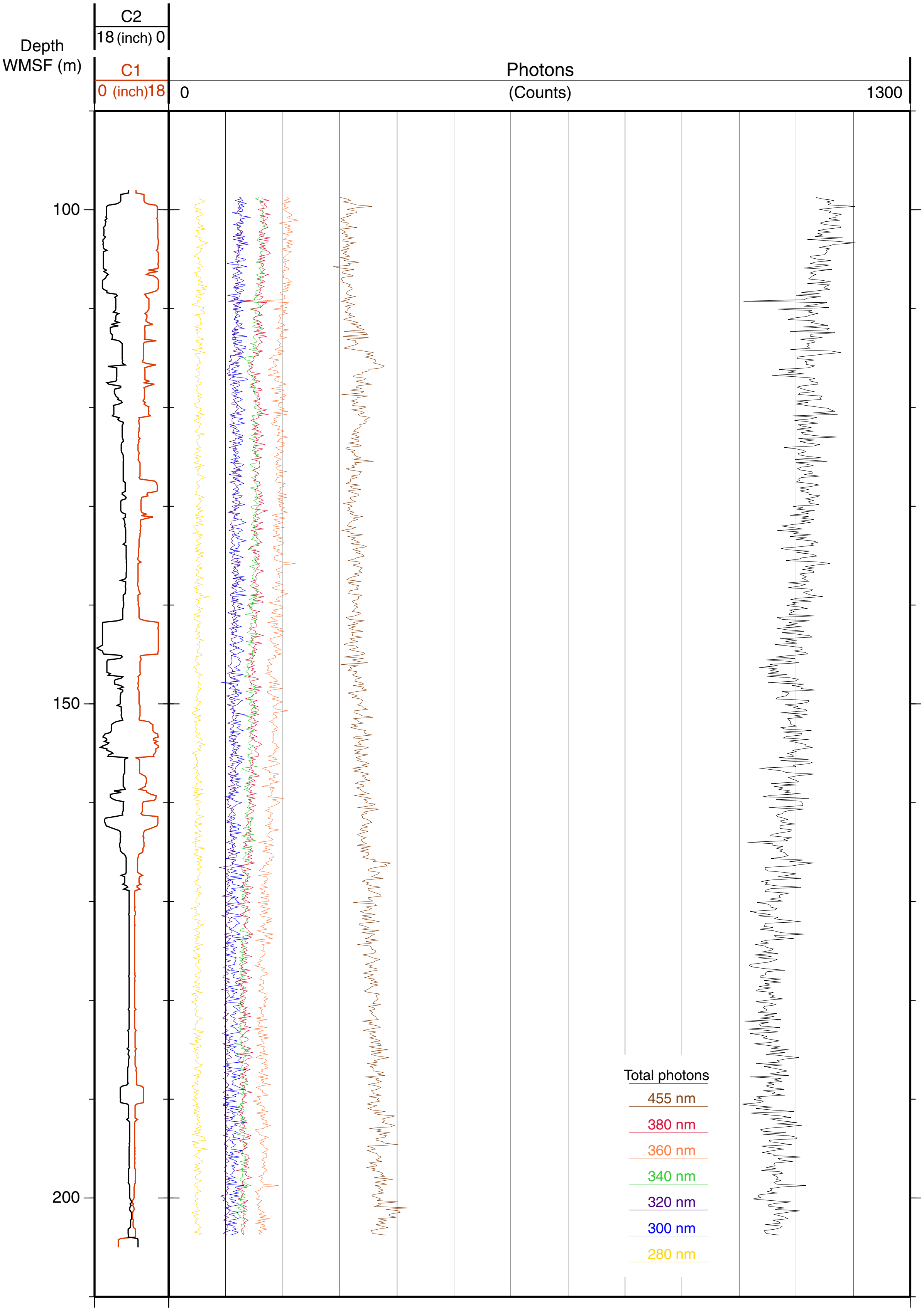

Figure F45. DEBI-t photon intensity data from Hole U1382A uplog.

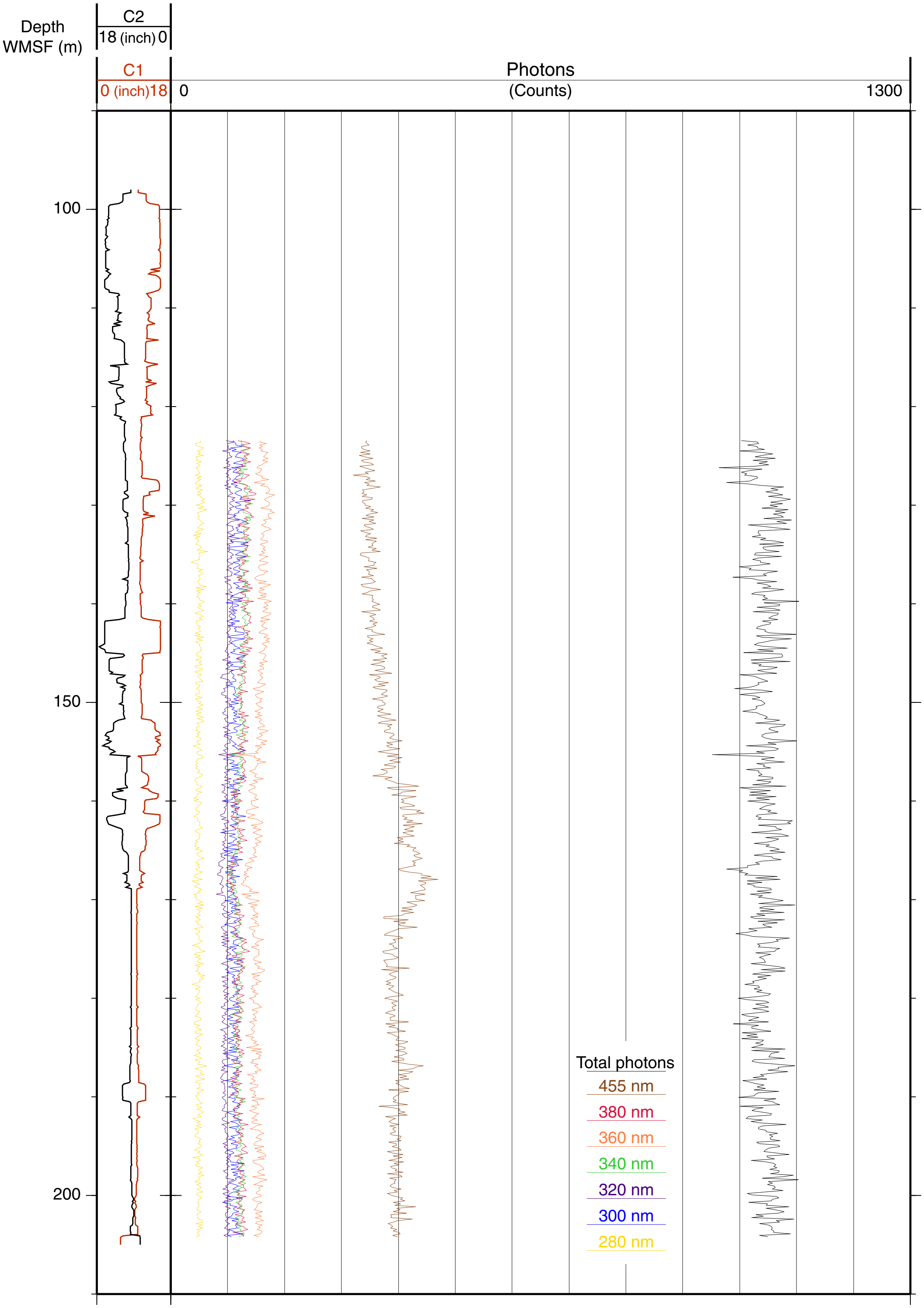

Figure F46. Summary comparing DEBI-t photon intensity data, Holes 395A and U1382A. The depth to which any pipe or casing was present is represented by a black line, and the shaded gray areas highlight the open-hole section.

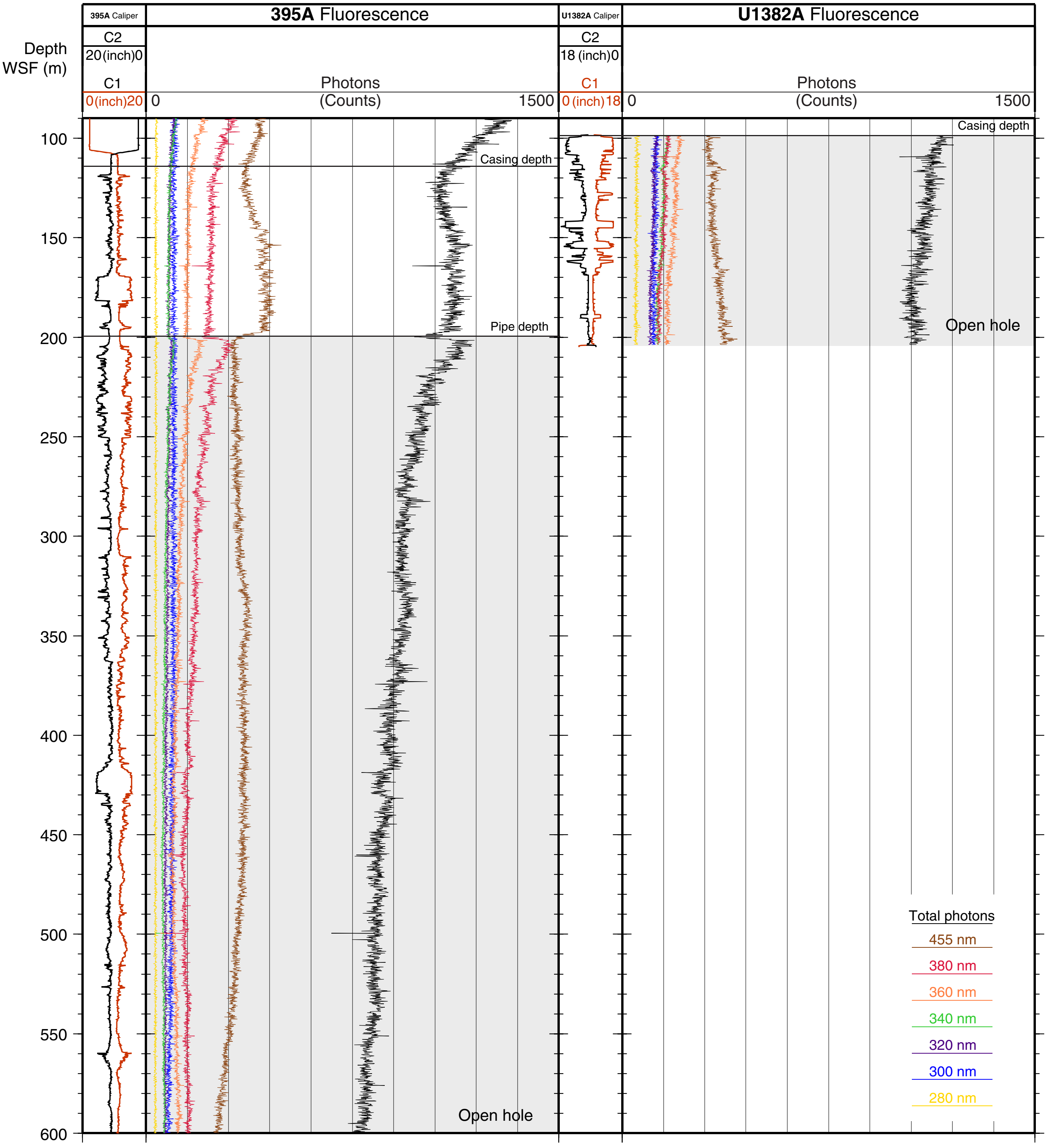

Figure F47. Composite of features imaged by the Formation MicroScanner (FMS), Hole U1382A. Note that images here are shown from both Pass 1 and 2 of the FMS-HNGS tool string. **A.** Very resistive peridotite unit surrounded by more conductive sediment/breccia. **B.** Massive basalt unit. **C.** Four potential flow units. **D.** Area of conductive sediment with some slightly more resistive clasts. A similar unit is also visible in Hole 395A FMS images (~6.4 m lower downsection). A high-resolution bulk density curve (in blue) is shown to the right of each FMS image for information.

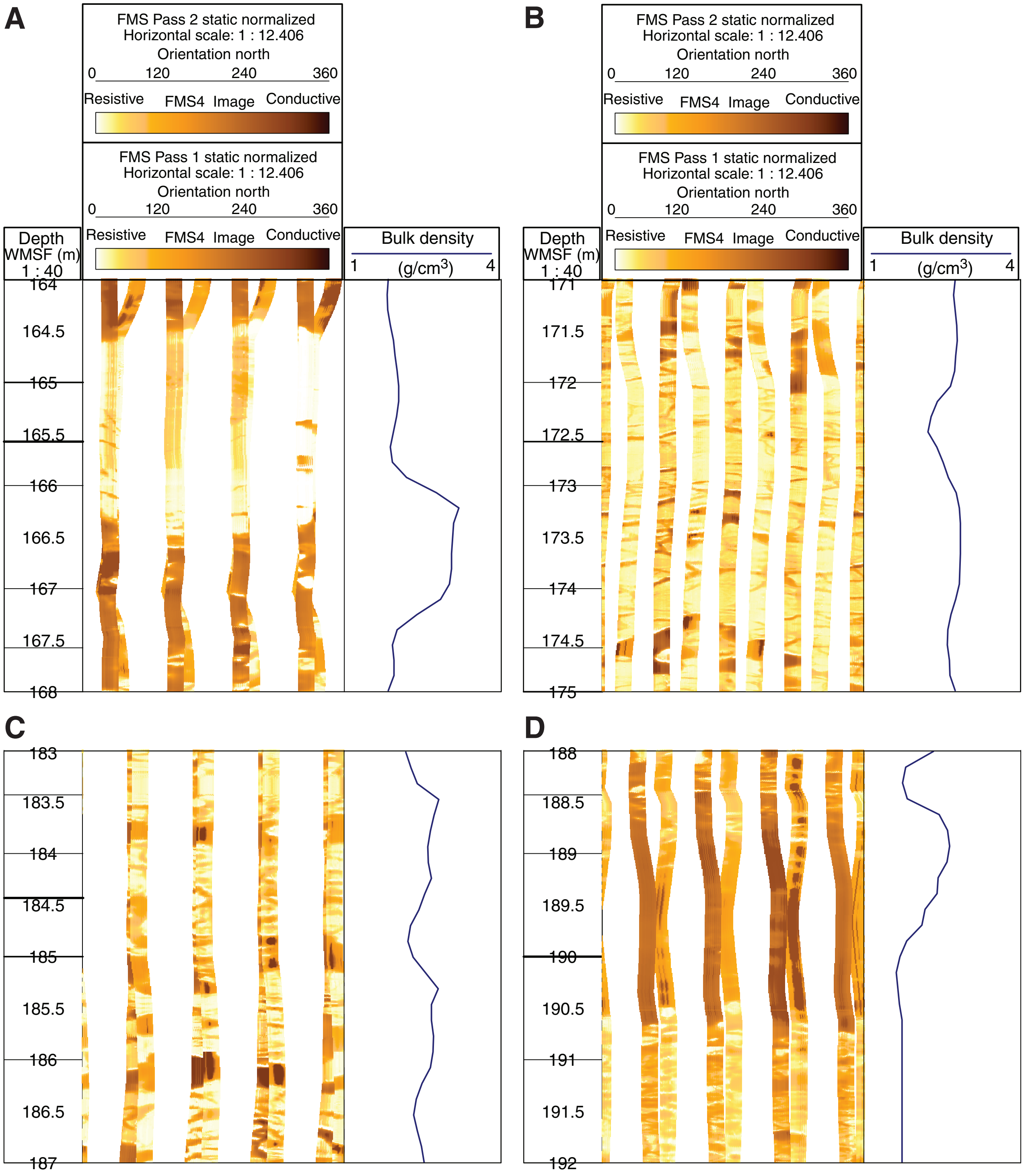

Figure F48. Composite showing preliminary core-log integration using core and Formation MicroScanner (FMS) imagery. **A.** Summary showing (from left to right) caliper logs (C1, C2 from FMS Pass 1 and single caliper [LCAL] from AMC I uplog), FMS dynamically normalized image showing a resistive boulder feature in Hole U1382A, total gamma ray curve, bulk density curve, and resistivity (RLA3-5 = medium to deep penetration measurement). **B.** Close-up of area of interest, with caliper measurement to the left of the FMS image. Core image to the right is set at the appropriate level on the image and lined up using the distinctive sinusoidal natural fracture (highlighted by the alteration halos on either side). **C.** High-resolution image of the outside of whole-round Section 336-U1382A-6R-3. The four images have been mosaicked together. Dashed lines = ties between A, B, and C.

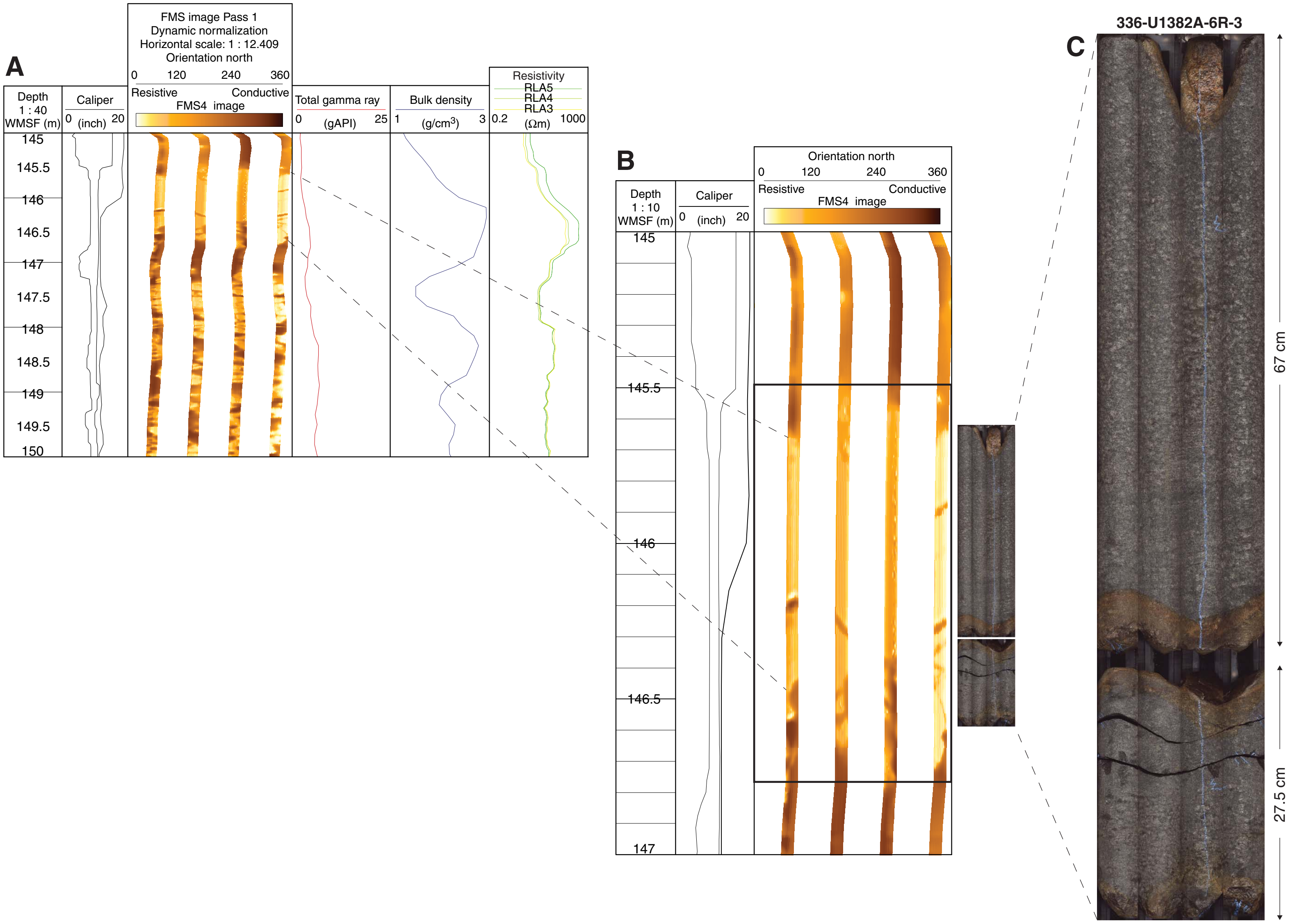

Figure F49. Pressure and temperature records collected with Micro-Smart downhole electronic Gauge 4986 during attempted packer experiments, Hole U1382A. I = inflation, D = unplanned deflation.

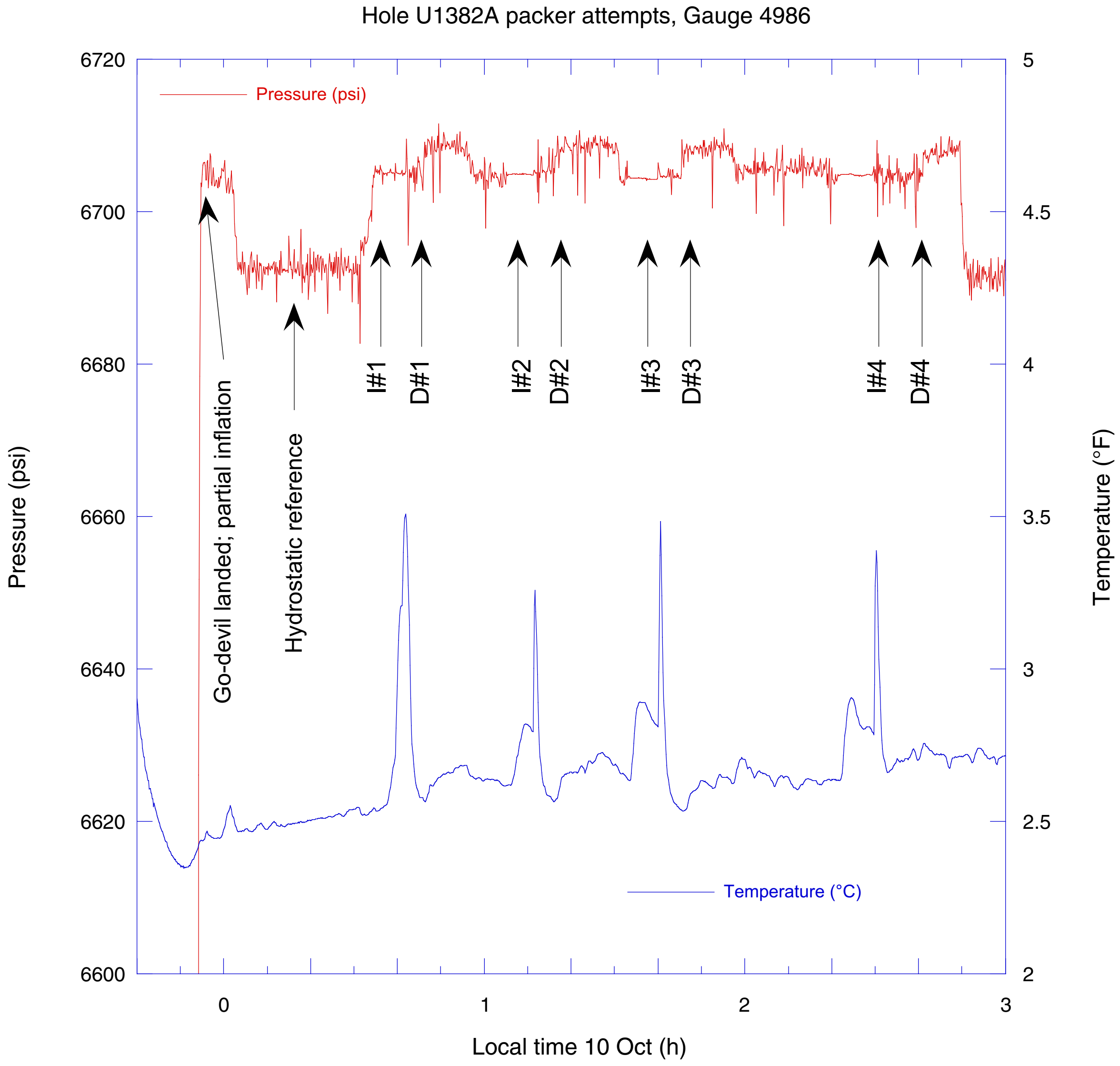

Table T1. Summary of operations, Hole U1382A. Operations included (A) installing a reentry cone with 53 m of 16 inch casing, (B) drilling a 14.75 inch hole, (C) installing/cementing 10.75 inch casing, (D) RCB coring, (E) downhole logging and packer experiments, and (F) installing a new subseafloor borehole observatory (CORK). (Continued on next three pages.)

	Start		End		Task time	
Operational task	Date (2011)	Time (h)	Date (2011)	Time (h)	Hours	Days
(A) Start round-trip for Hole U1382A: install reentry cone and 16 inch casing						
Install reentry cone	1 Oct	1230	1 Oct	1400	1.50	0.06
Handle BHA	1 Oct	1400	1 Oct	1500	1.00	0.04
Rig up/down for casing	1 Oct	1500	1 Oct	1545	0.75	0.03
Case with 16 inch casing from 0 to 53 mbsf at 3 joints/h, plus 0 h	1 Oct	1545	1 Oct	1730	1.75	0.07
Rig up/down for casing	1 Oct	1730	1 Oct	1730	0.00	0.00
Make up DQ running tool and replace master bushings	1 Oct	1730	1 Oct	1830	1.00	0.04
Pick up drill collars	1 Oct	1830	1 Oct	1915	0.75	0.03
Pull master bushings/lower and engage DQ running tool with reentry cone	1 Oct	1915	1 Oct	1945	0.50	0.02
Pick up reentry cone and open moonpool doors/lower reentry cone	1 Oct	1945	1 Oct	2030	0.75	0.03
Pick up tapered drill collar and 2 stands of 5.5 inch transition drill pipe	1 Oct	2030	1 Oct	2115	0.75	0.03
Damaged face on top joint of 5.5 inch transition drill pipe; lay out 2 stands and replace with 2 new stands of 5.5 inch transition drill pipe						
Trip: surface to mudline, plus 0.75 h in 4494 m of water	1 Oct	2115	2 Oct	0630	9.25	0.39
Repair broken hydraulic hose on iron roughneck after RIH with 2 stands of 5 inch drill pipe						
Install float valve in BHA—pipe trip slowed for periodic pipe filling						
Deploy camera system at 70 stands while RIH with drill string	2 Oct	0630	2 Oct	0700	0.50	0.02
Pick up top drive and space out drill pipe	2 Oct	0700	2 Oct	0745	0.75	0.03
Jet-in casing (takes 5 h)	2 Oct	0745	2 Oct	1030	2.75	0.11
Release running tool	2 Oct	1030	2 Oct	1030	0.00	0.00
Set back top drive	2 Oct	1030	2 Oct	1100	0.50	0.02
Trip: mudline to surface, plus 0 h in 4494 m of water	2 Oct	1100	2 Oct	1730	6.50	0.27
Recover camera system while POOH with drill string	2 Oct	1730	2 Oct	1800	0.50	0.02
Handle BHA	2 Oct	1800	2 Oct	1930	1.50	0.06
(B) Drill 14.75 inch hole with tricone bit for 10.75 inch casing						
Handle BHA	2 Oct	1930	2 Oct	2000	0.50	0.02
Trip: surface to mudline, plus 0 h in 4494 m of water	2 Oct	2000	3 Oct	0330	7.50	0.31
Maneuver ship for reentry	3 Oct	0330	3 Oct	0345	0.25	0.01
Pick up top drive and space out drill pipe; official reentry time of 0348 h	3 Oct	0345	3 Oct	0415	0.50	0.02
Move bit from (mudline) 0 to 53 mbsf	3 Oct	0415	3 Oct	0445	0.50	0.02
Handle camera system	3 Oct	0445	3 Oct	0530	0.75	0.03
Drill ahead sediment to basement: 53–91 mbsf at 30 m/h	3 Oct	0530	3 Oct	0715	1.75	0.07
Drill ahead basement: 91–110 mbsf at 5 m/h	3 Oct	0715	3 Oct	1200	4.75	0.20
Circulation	3 Oct	1200	3 Oct	1245	0.75	0.03
Basement at ~90 mbsf						
Wiper trip: 110 to 60 mbsf and back	3 Oct	1245	3 Oct	1315	0.50	0.02
Circulation	3 Oct	1315	3 Oct	1515	2.00	0.08
Set back top drive (clear seafloor at 1605 h)	3 Oct	1515	3 Oct	1545	0.50	0.02
Trip: depth to surface: 110 mbsf to surface, plus 0 h in 4494 m of water	3 Oct	1545	3 Oct	2230	6.75	0.28
Handle BHA	3 Oct	2230	3 Oct	2300	0.50	0.02
(C) Make up and install 10.75 inch casing to 102 mbsf						
Make up stand with DQ running tool and stand back in derrick	3 Oct	2300	3 Oct	2330	0.50	0.02
Slip/Cut drill line	3 Oct	2330	4 Oct	0130	2.00	0.08
Rig up/down for casing	4 Oct	0130	4 Oct	0215	0.75	0.03
Case with 10.75 inch casing from 0 to 102 mbsf at 4 joints/h, plus 0 h	4 Oct	0215	4 Oct	0445	2.50	0.10
Make up 10.75 inch casing hanger and weld coupling/weld all casing couplings	4 Oct	0445	4 Oct	0500	0.25	0.01
Make up DQ running tool to casing hanger/pull bushings/lower though rotary table	4 Oct	0500	4 Oct	0600	1.00	0.04
Make up 2 stands of 8.25 inch drill collars	4 Oct	0600	4 Oct	0615	0.25	0.01
Trip: surface to mudline, plus 0 h in 4494 m of water	4 Oct	0615	4 Oct	1300	6.75	0.28
Handle camera system	4 Oct	1300	4 Oct	1330	0.50	0.02
Maneuver ship for reentry; reenter at 1355 h	4 Oct	1330	4 Oct	1400	0.50	0.02
Pick up top drive and space out drill pipe	4 Oct	1400	4 Oct	1430	0.50	0.02
RIH with 10.75 inch casing/land casing hanger (land at 1515 h)	4 Oct	1430	4 Oct	1515	0.75	0.03
Cement casing shoe	4 Oct	1515	4 Oct	1700	1.75	0.07
Release cone/casing hanger	4 Oct	1700	4 Oct	1715	0.25	0.01
Displace drill pipe and perform survey of Hole 395A reentry cone	4 Oct	1715	4 Oct	1815	1.00	0.04
Trip: depth to surface: (mudline) 0 mbsf to surface, plus 1.25 h in 4494 m of water	4 Oct	1815	5 Oct	0100	6.75	0.28
Recover camera system	5 Oct	0100	5 Oct	0130	0.50	0.02
Handle BHA	5 Oct	0130	5 Oct	0215	0.75	0.03
De-torque DQ running tool and prepare to make up RCB coring assembly	5 Oct	0215	5 Oct	0300	0.75	0.03
(D) RCB coring						
Make up RCB core barrel/center bit assembly	5 Oct	0300	5 Oct	0400	1.00	0.04

Table T1 (continued). (Continued on next page.)

	Start		End		Task time	
Operational task	Date (2011)	Time (h)	Date (2011)	Time (h)	Hours	Days
Make up C-7 RCB core bit and outer core barrel assembly	5 Oct	0400	5 Oct	0500	1.00	0.04
Space out core barrels	5 Oct	0500	5 Oct	0530	0.50	0.02
Install center bit	5 Oct	0530	5 Oct	0600	0.50	0.02
Handle BHA	5 Oct	0600	5 Oct	0700	1.00	0.04
Trip: surface to mudline, plus 0 h in 4494 m of water	5 Oct	0700	5 Oct	1300	6.00	0.25
Handle camera system	5 Oct	1300	5 Oct	1330	0.50	0.02
Maneuver ship for reentry; reenter at 1337 h	5 Oct	1330	5 Oct	1330	0.00	0.00
Handle camera system	5 Oct	1330	5 Oct	1430	1.00	0.04
Trip: mudline to depth: 0–87 mbsf, plus 0 h	5 Oct	1430	5 Oct	1445	0.25	0.01
Pick up top drive and space out drill pipe	5 Oct	1445	5 Oct	1515	0.50	0.02
Tag cement 14 m above casing shoe at 88 mbsf or 4582 mbrf						
Slow circulation (SCR)	5 Oct	1515	5 Oct	1530	0.25	0.01
Drill out cement: 87–110 mbsf at 10 m/h, or 0 h	5 Oct	1530	5 Oct	1745	2.25	0.09
Circulation will take 1.25 h	5 Oct	1745	5 Oct	1900	1.25	0.05
Recover RCB center bit	5 Oct	1900	5 Oct	2015	1.25	0.05
Check core barrel spaceout against center bit spaceout	5 Oct	2015	5 Oct	2045	0.50	0.02
Pump down RCB core barrel and record SCRs	5 Oct	2045	5 Oct	2115	0.50	0.02
RCB core basement: 110.0–113.3 mbsf at 5 m/h; Core 336-U1382A-2R on deck at 2245 h	5 Oct	2115	5 Oct	2245	1.50	0.06
RCB core basement: 113.3–122.9 mbsf at 5 m/h; Core 336-U1382A-3R on deck at 0525 h	5 Oct	2245	6 Oct	0530	6.75	0.28
RCB core basement: 122.9–132.5 mbsf at 5 m/h; Core 336-U1382A-4R on deck at 0910 h	6 Oct	0530	6 Oct	0915	3.75	0.16
RCB core basement: 132.5–142.1 mbsf at 5 m/h; Core 336-U1382A-5R on deck at 1220 h	6 Oct	0915	6 Oct	1215	3.00	0.13
RCB core basement: 142.1–151.7 mbsf at 5 m/h; Core 336-U1382A-6R on deck at 1555 h	6 Oct	1215	6 Oct	1600	3.75	0.16
RCB core basement: 151.7–161.3 mbsf at 3 m/h; Core 336-U1382A-7R on deck at 2045 h	6 Oct	1600	6 Oct	2045	4.75	0.20
Work drill string (hole trouble on Core 7R)	6 Oct	2045	6 Oct	2130	0.75	0.03
Trip: wiper trip: 161.3 mbsf to 102 mbsf and back	6 Oct	2130	7 Oct	0015	2.75	0.11
Circulation	7 Oct	0015	7 Oct	0100	0.75	0.03
Deploy core barrel	7 Oct	0100	7 Oct	0130	0.50	0.02
RCB core basement: 161.3–170.9 mbsf at 4 m/h; Core 336-U1382A-8R on deck at 0415 h	7 Oct	0130	7 Oct	0415	2.75	0.11
RCB core basement: 170.9–180.5 mbsf at 4 m/h; Core 336-U1382A-9R on deck at 0905 h	7 Oct	0415	7 Oct	0900	4.75	0.20
RCB core basement: 180.5–190.1 mbsf at 4 m/h; Core 336-U1382A-10R on deck at 1325 h	7 Oct	0900	7 Oct	1330	4.50	0.19
RCB core basement: 190.1–199.7 mbsf at 4 m/h; Core 336-U1382A-11R on deck at 1710 h	7 Oct	1330	7 Oct	1715	3.75	0.16
RCB core basement: 199.7–210 mbsf at 4 m/h	7 Oct	1715	7 Oct	2130	4.25	0.18
Circulation	7 Oct	2130	7 Oct	2200	0.50	0.02
RIH with wireline and recover Core 336-U1382A-12R; on deck at 2320 h	7 Oct	2200	7 Oct	2330	1.50	0.06
Planning used 5 m/h based on ROP for first 100 m of basement in Hole 395A while coring; actual round-trip wireline time was ~1.5 h						
Problem with stabbing sinker bars delayed going after Core 3R until ~0400 h						
Wiper trip 1: 210–80 mbsf and back; a couple of tight spots—likely bridges but not bad overall	7 Oct	2330	8 Oct	0130	2.00	0.08
Circulation	8 Oct	0130	8 Oct	0200	0.50	0.02
Wiper trip 2: 210–80 mbsf and back; all good (lowered without rotation or circulation)—no fill, bridges, or ledges; flush hole with high-vis mud followed with 2 volumes of saltwater	8 Oct	0200	8 Oct	0245	0.75	0.03
Circulation	8 Oct	0245	8 Oct	0330	0.75	0.03
Wiper trip 3: 210–80 mbsf and back (without circulation or rotation; ultimately required rotation and circulation); tagged bridges at 4663, 4666, 4677, and 4682 m; no fill on bottom	8 Oct	0330	8 Oct	0500	1.50	0.06
This time no circulation on bottom						
Pull back above 4663 mbrf; lower with no pump or circulation						
Wiper trip 4: 210–80 mbsf and back	8 Oct	0500	8 Oct	0530	0.50	0.02
Attempt final wiper trip to/from casing shoe without circulation or rotation; if successful, POOH without additional circulation						
Wiper trip 5: 210–80 mbsf and back	8 Oct	0530	8 Oct	0630	1.00	0.04
Set back top drive	8 Oct	0630	8 Oct	0715	0.75	0.03
Trip: depth to surface: 210 mbsf to surface, plus 0 h in 4494 m of water; clear seafloor at 0729 h	8 Oct	0715	8 Oct	1400	6.75	0.28
Handle BHA	8 Oct	1400	8 Oct	1430	0.50	0.02
Clear rotary table at 1430 h						
Make up and paint 6.75 inch stand of perforated drill collar for CORK (will take 2 h)	8 Oct	1430	8 Oct	1645	2.25	0.09
(E) Downhole logging, packer experiment, and hole depth check						
Handle BHA	8 Oct	1645	8 Oct	1745	1.00	0.04
Trip: surface to mudline, plus 1.25 h in 4494 m of water	8 Oct	1745	9 Oct	0000	6.25	0.26
Handle camera system	9 Oct	0000	9 Oct	0030	0.50	0.02
Rig up circulating head/pump pig to clear pipe of any rust	9 Oct	0030	9 Oct	0100	0.50	0.02
Rig down circulating head/spaceout for reentry	9 Oct	0100	9 Oct	0130	0.50	0.02
Maneuver ship for reentry; reenter Hole U1382A at 0138 h	9 Oct	0130	9 Oct	0145	0.25	0.01
Trip: mudline to depth: 0–60 mbsf, plus 0.25 h	9 Oct	0145	9 Oct	0200	0.25	0.01
Rig up	9 Oct	0200	9 Oct	0300	1.00	0.04
Triple combo with DEBI-t: log 60–250 mbsf at 275 m/h; power failure downhole on logging tools; back to surface after almost completing first pass	9 Oct	0300	9 Oct	1215	9.25	0.39
FMS-sonic: log 60–250 mbsf at 275 m/h	9 Oct	1215	9 Oct	2100	8.75	0.36

Table T1 (continued). (Continued on next page.)

	Start		End		Task time	
Operational task	Date (2011)	Time (h)	Date (2011)	Time (h)	Hours	Days
FMS tools unable to reenter drill pipe—problems started at ~1612 h; tool was freed at 1815 h; nothing left in hole—damage consisted of a bent pad on 1 caliper arm						
Rig down	9 Oct	2100	9 Oct	2200	1.00	0.04
Pick up top drive and space out drill pipe	9 Oct	2200	9 Oct	2230	0.50	0.02
Pressure test system	9 Oct	2230	9 Oct	2245	0.25	0.01
Set packer depth	9 Oct	2245	9 Oct	2315	0.50	0.02
Install pressure gauges and deploy packer setting go-devil	9 Oct	2315	10 Oct	0000	0.75	0.03
Stand by 30 min for hydrostatic pressure reference	10 Oct	0000	10 Oct	0030	0.50	0.02
Inflate and lock packer element by setting weight down	10 Oct	0030	10 Oct	0045	0.25	0.01
Packer slipped 3 times. Hold for ~5 min. Fine balance between too much weight down and large heave (2.5–3.0 m)–induced release						
Packer held >10 min but then deflated again; flow testing was abandoned						
Inflate and lock packer element by setting weight down (will take 1.75 h)	10 Oct	0045	10 Oct	0245	2.00	0.08
Wireline trip to get go-devil out of packer (will take 1.75 h); end of drill string packer permeability flow testing	10 Oct	0245	10 Oct	0445	2.00	0.08
Break out pressure gauges and lay out knobby	10 Oct	0445	10 Oct	0500	0.25	0.01
Set back top drive	10 Oct	0500	10 Oct	0515	0.25	0.01
Lower drill string for depth check to total depth of 210 mbsf; passed through problem zone (per caliper log) at 112–132 mbsf twice with no overpull or drag						
Trip: depth to depth: 60–210 mbsf, plus 0.75 h in 4494 m of water	10 Oct	0515	10 Oct	0630	1.25	0.05
Trip: depth to surface: 210 mbsf to surface, plus 0 h in 4494 m of water; clear seafloor at 0655 h	10 Oct	0630	10 Oct	1245	6.25	0.26
Handle BHA (will take 1.25 h)	10 Oct	1245	10 Oct	1330	0.75	0.03
Logging bit cleared rotary table at 1328 h						
Slip and cut drill line	10 Oct	1330	10 Oct	1500	1.50	0.06
(F) Make up CORK observatory						
Make up CORK stinger assembly, packer, and 4.5 inch casing, plus umbilicals (will take 7 h)	10 Oct	1500	10 Oct	2200	7.00	0.29
Open stabber, change elevator bales, position CORK head, make up running tool, and make up CORK head to top of casing string	10 Oct	2200	10 Oct	2300	1.00	0.04
Remove bushings and lower CORK head into moonpool for umbilical termination	10 Oct	2300	10 Oct	2315	0.25	0.01
Cut umbilicals to length, install miniscreens, and make up final connections to L-CORK head	10 Oct	2315	11 Oct	0000	0.75	0.03
Hang off CORK head in moonpool on C-plates and elevators	11 Oct	0000	11 Oct	0045	0.75	0.03
Remove CORK running tool	11 Oct	0045	11 Oct	0100	0.25	0.01
Make up and lower OsmoSampler string into CORK						
Make up instrument string and top plug	11 Oct	0100	11 Oct	0200	1.00	0.04
Troubleshoot top plug latch, check release load with strain gauge, and modify latch	11 Oct	0200	11 Oct	0230	0.50	0.02
Spend 37 min to repair damage to iron roughneck track	11 Oct	0230	11 Oct	0315	0.75	0.03
Torque up pup joint on CORK running tool	11 Oct	0315	11 Oct	0315	0.00	0.00
Remove master bushing	11 Oct	0315	11 Oct	0330	0.25	0.01
Make up CORK running tool with CORK head and remove C-plates/open moonpool	11 Oct	0330	11 Oct	0330	0.00	0.00
Attach packer inflate hose and safety line from running tool to CORK head/lower to moonpool	11 Oct	0330	11 Oct	0400	0.50	0.02
Replace bushings at rig floor	11 Oct	0400	11 Oct	0415	0.25	0.01
Pick up first stand of drill collars	11 Oct	0415	11 Oct	0430	0.25	0.01
Inspect valve settings on CORK head prior to “dunking”	11 Oct	0430	11 Oct	0445	0.25	0.01
Open moonpool doors	11 Oct	0445	11 Oct	0445	0.00	0.00
Lower/Raise CORK below keel to purge air from all lines	11 Oct	0445	11 Oct	0500	0.25	0.01
Install osmo pump/check all valve positions and secure with rubber bands	11 Oct	0500	11 Oct	0530	0.50	0.02
Remove grating and open moonpool doors	11 Oct	0530	11 Oct	0545	0.25	0.01
Test-fit camera system sleeve over the CORK	11 Oct	0545	11 Oct	0615	0.50	0.02
Make up remainder of BHA and RIH with 2 stands of 5.5 inch transition pipe	11 Oct	0615	11 Oct	0630	0.25	0.01
Trip: surface to mudline, plus 1 h in 4494 m of water	11 Oct	0630	11 Oct	1530	9.00	0.38
Deploy camera system	11 Oct	1530	11 Oct	1600	0.50	0.02
Maneuver ship for reentry; reenter Hole U1382A at 1630 h	11 Oct	1600	11 Oct	1630	0.50	0.02
Pick up top drive and space out drill pipe	11 Oct	1630	11 Oct	1730	1.00	0.04
Land CORK (1820 h) and inflate packer	11 Oct	1730	11 Oct	1815	0.75	0.03
Deploy ROV platform						
Recover camera system (TV/sonar) from seafloor	11 Oct	1815	11 Oct	2030	2.25	0.09
Assemble ROV platform with camera system	11 Oct	2030	11 Oct	2145	1.25	0.05
Deploy and release ROV platform; platform released and settled over CORK head at 0055 h	11 Oct	2145	12 Oct	0100	3.25	0.14
Recover camera system (TV/sonar) from seafloor	12 Oct	0100	12 Oct	0215	1.25	0.05
Remove deployment slings and platform deployment tool	12 Oct	0215	12 Oct	0230	0.25	0.01
Troubleshoot/repair subsea TV/sonar system	12 Oct	0230	12 Oct	0245	0.25	0.01
Deploy camera system (TV/sonar) to seafloor	12 Oct	0245	12 Oct	0415	1.50	0.06
	12 Oct	0415	12 Oct	0430	0.25	0.01
Pull out of hole						
Set back top drive	12 Oct	0430	12 Oct	0500	0.50	0.02
Trip: mudline to surface, plus 1.25 h in 4494 m of water	12 Oct	0500	12 Oct	1100	6.00	0.25

Table T1 (continued).

Operational task	Start		End		Task time	
	Date (2011)	Time (h)	Date (2011)	Time (h)	Hours	Days
Recover camera system	12 Oct	1100	12 Oct	1130	0.50	0.02
Handle BHA	12 Oct	1130	12 Oct	1145	0.25	0.01
CORK running tool clears the rig floor at 1145 h						
Beacon back on deck at 1210 h						
Hole U1382A totals:	1 Oct	1230	12 Oct	1145	263.25	10.97

Times are local ship time (Universal Time Coordinated [UTC] – 3 h) for all onsite operations. BHA = bottom-hole assembly, DQ = Dril-Quip, TDC = tapered drill collar, RIH = run in hole, POOH = pull out of hole. RCB = rotary core barrel. SCR = slow circulation rate.

Table T2. Coring summary, Site U1382.

Hole U1382A

Latitude: 22°45.3531′N
Longitude: 46°04.8911′W
Time on site (h): 263.3 (1230 h, 1 October to 1145 h, 12 October 2011; ship local)
Seafloor (drill pipe measurement below rig floor in meters; DRF): 4494.0
Distance between rig floor and sea level (m): 11.1
Water depth (drill pipe measurement from sea level in meters): 4482.9
Total penetration (drilling depth below seafloor in meters; DSF): 210.0
Total depth (drill pipe measurement from rig floor in meters; DRF): 4704.0
Total length of cored section (m): 100.0
Total core recovered (m): 33.3
Core recovery (%): 33
Total number of cores: 11

Core	Date (2011)	Local time (h)	Depth DSF (m)		Interval cored (m)	Length of core recovered (m)	Curated length (m)	Recovery (%)
			Top of cored interval	Bottom of cored interval				
336-U1382A-								
1-1			*****Drilled from 0.0 to 53.13 m DSF*****					
1-2			*****Drilled from 53.13 to 110.0 m DSF*****					
2R	6 Oct	0145	110.0	113.3	3.3	1.31	1.60	40
3R	6 Oct	0825	113.3	122.9	9.6	6.00	6.36	63
4R	6 Oct	1210	122.9	132.5	9.6	3.00	3.49	47
5R	6 Oct	1520	132.5	142.1	9.6	2.43	3.17	25
6R	6 Oct	1955	142.1	151.7	9.6	2.43	3.27	25
7R	6 Oct	2345	151.7	161.3	9.6	1.99	2.71	21
8R	7 Oct	0715	161.3	170.9	9.6	2.59	2.90	27
9R	7 Oct	1205	170.9	180.5	9.6	4.51	5.67	47
10R	7 Oct	1625	180.5	190.1	9.6	3.89	5.10	41
11R	7 Oct	2010	190.1	199.7	9.6	1.41	1.75	15
12R	8 Oct	0220	199.7	210.0	10.3	2.23	2.23	22
				Totals:	100.0	31.79	38.25	32

Local time is Universal Time Coordinated (UTC) – 3 h. DRF = drilling depth below rig floor, DSF = drilling depth below seafloor. R = rotary core barrel core, numeric core type = drilled interval.

Table T3. Configuration of new subseafloor borehole observatory (CORK) completion hardware deployed in Hole U1382A.

Part number	Description	Diameter (inch)		Connection		Measured length (m)	Cumulative bottom depth (mbsf)	Comments
		Outside	Inside	Up	Down			
	CORK	5.00	4.05		4.50 8RD STC pin	1.32	1.3	1.18 m CORK + 0.14 mbsf
27	Casing, 4.5 inch, 10.5 lb	5.00	4.05	4.50 8RD cplg box	4.50 8RD STC pin	11.50	12.8	
28	Casing, 4.5 inch, 10.5 lb	5.00	4.05	4.50 8RD cplg box	4.50 8RD STC pin	13.75	26.6	
29	Casing, 4.5 inch, 10.5 lb	5.00	4.05	4.50 8RD cplg box	4.50 8RD STC pin	13.73	40.3	
30	Casing, 4.5 inch, 10.5 lb	5.00	4.05	4.50 8RD cplg box	4.50 8RD STC pin	11.31	51.6	
31	Casing, 4.5 inch, 10.5 lb	5.00	4.05	4.50 8RD cplg box	4.50 8RD STC pin	11.48	63.1	
32	Casing, 4.5 inch, 10.5 lb	5.00	4.05	4.50 8RD cplg box	4.50 8RD STC pin	11.47	74.6	
33	Casing, 4.5 inch, 10.5 lb	5.00	4.05	4.50 8RD cplg box	4.50 8RD STC pin	13.77	88.3	
OH5071	Casing pup, 4.5 inch, 10.5 lb	5.00	4.05	4.50 8RD cplg box	4.50 8RD STC pin	2.00	90.3	
OH5071	Casing pup, 4.5 inch, 10.5 lb	5.00	4.05	4.50 8RD cplg box	4.50 8RD STC pin	2.00	92.3	
D2	Packer, combo, 4.5 inch, coated	10.50	4.05	4.50 8RD cplg box	4.50 8RD STC pin	9.07	101.4	10.75 inch 54 lb casing to 102 mbsf
OJ3221	Landing seat, 3.375 inch, coated	5.00	3.375	4.50 8RD STC box	4.50 8RD STC pin	0.19	101.6	
OJ3225	Crossover, 4-1/2 inch LTC × 4-1/2 inch EUE	5.00	4.00	4.50 8RD LTC box	4.50 8RD EUE pin	0.18	101.8	
76	Casing, 4.5 inch, fiberglass - red	5.00	3.91	4.50 8RD EUE box	4.50 8RD EUE pin	8.80	110.6	
77	Casing, 4.5 inch, fiberglass - red	5.00	3.91	4.50 8RD EUE box	4.50 8RD EUE pin	8.77	119.3	
78	Casing, 4.5 inch, fiberglass - red	5.00	3.91	4.50 8RD EUE box	4.50 8RD EUE pin	8.84	128.2	
79	Casing, 4.5 inch, fiberglass - red	5.00	3.91	4.50 8RD EUE box	4.50 8RD EUE pin	8.83	137.0	
80	Casing, 4.5 inch, fiberglass - red	5.00	3.91	4.50 8RD EUE box	4.50 8RD EUE pin	8.83	145.8	
OJ3226	Crossover, 4-1/2 inch EUE × 4-1/2 inch STC	5.50	4.00	4.50 8RD EUE box	4.50 8RD STC pin	0.19	146.0	
OJ3282	Crossover, 4.5 inch × 5.5 inch, coated	5.50	4.05	4.50 8RD LTC box	5.50 8RD LTC pin	0.19	146.2	
OJ3283	Casing, 5.5 inch, perforated, coated, 14 lb	6.05	5.01	5.50 8RD LTC cplg	5.50 8RD STC pin	3.12	149.3	
OJ3284	Casing, 5.5 inch, perforated, coated, 14 lb	6.05	5.01	5.50 8RD LTC cplg	5.50 8RD STC pin	6.12	155.5	
OJ3284	Casing, 5.5 inch, perforated, coated, 14 lb	6.05	5.01	5.50 8RD LTC cplg	5.50 8RD STC pin	6.12	161.6	Miniscreens*
OJ3281	Crossover, 5.5 inch × 6.75 inch, coated	6.75	4.13	5.50 8RD LTC box	5.5 FH pin	0.48	162.1	
OJ3285	Drill collar, perforated, coated	6.75	4.13	5.50 FHM box	5.5 FHM pin	4.29	166.3	
OJ3285	Drill collar, perforated, coated	6.75	4.13	5.50 FHM box	5.5 FHM pin	4.29	170.6	
OJ3285	Drill collar, perforated, coated	6.75	4.13	5.50 FHM box	5.5 FHM pin	4.29	174.9	
OJ3285	Drill collar, perforated, coated	6.75	4.13	5.50 FHM box	5.5 FHM pin	4.29	179.2	
OJ3285	Drill collar, perforated, coated	6.75	4.13	5.50 FHM box	5.5 FHM pin	4.29	183.5	
OJ3285	Drill collar, perforated, coated	6.75	4.13	5.50 FHM box	5.5 FHM pin	4.29	187.8	
OJ3286	Bullnose, coated	6.75	4.13	5.50 FHM box	Bullnose	0.91	188.7	

* = 160.0–161.6 m microbiology umbilicals (0.5 inch ID Tefzel), 158.0 m stainless steel pressure and packer inflation umbilicals (1 × 0.5 inch OD and 2 × 0.25 inch OD), and 160–161 m stainless steel geochemistry umbilicals (3 × 0.25 inch OD and 3 × 0.125 inch OD). Part numbers beginning with "OJ" designate USIO engineering part numbers; numbers 27–80 are identification numbers assigned when casing was loaded and measured. ID = inside diameter, OD = outside diameter. 8RD = size of threaded tubing connection, STC = short thread coupling, cplg = coupling, LTC = long thread coupling, EUE = external upset ends connection, FH = full hole threaded tool joint, FHM = full hole modified tool joint, box = female threaded connection, pin = male threaded connection.

Table T4. Downhole instrument string deployed in Hole U1382A CORK.

Item	Length (m)	Connector length (m)*	Depth (mbsf)	FLOCS or O_2 probe ID	Temperature probe[†]
Bottom of top plug			–6.45		
Spectra with hose	1 (1.02)		–5.43		
Small sinker bar - 10 lb	0.3		–5.13		
Spectra[‡]	39.5 (40.09)		34.96		
Middle sinker bar - 100 lb	1.524		36.49		
Spectra[‡]	66.2 (67.19)				
Landing seat, 3.375, coated			101.60		
Spectra[‡]	43.4 (44.05)		145.65		
MBIO OS	5.73	0.16	151.54	90/91	O 9913817
Enrichment OS	5.2	0.16	156.90	92/93	
Standard OS	2.63	0.16	159.69		
Oxygen probe	0.58	0.16	160.43	22004	
Acid-addition OS	5.2	0.16	165.79		
BOSS OS	5.2	0.16	171.15		
Copper OS - Gas	2.63	0.16	173.94		
Sinker bar - 150 lb	3.19	0.16	177.29		A 1857005

* = a stainless steel coupler was used to join two packages and join packages to the sinker bar. † = temperature probes were purchased from Onset (O) and Antares (A). Probes are located 53 cm from the top of the OsmoSampler packages. ‡ = Spectra lengths are given in measured units and expected lengths based on stretch within the hole (in parentheses); some downhole depths for Spectra are not given because additional line was used to ensure that the plugs could seat at the correct depths. Lifting loops were weaved at 10.5, 23, and 35.5 m for the 43.4 m long rope; 14.3, 26.8, 39.3, 51.8, and 64.3 m for the 66.2 m long rope; and 2, 14.5, and 27.5 for the 39.5 m long rope. FLOCS = Flow-through Osmo Colonization System. MBIO = microbiology, OS = OsmoSampler, BOSS = BioOsmoSampling System.

Table T5. Summary of basement stratigraphy and subunits recovered in Hole U1382A.

Lith. unit	Subunit	Depth (mbsf)		Lithology	Vesicles	Description	Groundmass alteration (%)
		Top	Bottom				
1	1-1	110.00	110.17	Aphyric fine-grained basalt	Nonvesicular	Massive flow	~10
	1-2	110.17	113.63	Aphyric medium-grained basalt	Nonvesicular	Massive flow	5–20
	1-3	113.71	116.20	Aphyric fine- to medium-grained basalt	Nonvesicular	Massive flow	2–10
	1-4	116.20	119.61	Aphyric fine- to medium-grained basalt	Nonvesicular	Massive flow	1–12
2	2-1	119.61	123.20	Aphyric cryptocrystalline basalt	Sparsely vesicular (0.5%–3%)	Pillow flow	0–7
	2-2	123.26	123.65	Aphyric cryptocrystalline basalt	Sparsely vesicular (0%–3%)	Pillow flow	1–5
	2-3	123.65	124.25	Aphyric cryptocrystalline basalt	Sparsely vesicular (0%–3%)	Pillow flow	1–8
	2-4	124.25	124.57	aphyric cryptocrystalline to glassy basalt	Sparsely vesicular (0%–1%)	Pillow flow	0–7
	2-5	124.57	124.64	Breccia - hyaloclastite			
	2-6	124.64	125.26	Aphyric cryptocrystalline to fine-grained basalt	Sparsely vesicular (0.5%–3%)	Pillow flow	6–10
	2-7	125.26	125.95	Aphyric cryptocrystalline basalt	Sparsely vesicular (0%–3%)	Pillow flow	5–7
	2-8	125.95	126.39	Aphyric cryptocrystalline basalt	Sparsely vesicular (0%–5%)	Pillow flow	1–6
	2-9	132.50	132.62	Aphyric cryptocrystalline to glassy basalt	Sparsely vesicular (0%–1%)	Pillow flow	3
	2-10	132.62	132.91	Aphyric cryptocrystalline to fine-grained basalt	Sparsely vesicular (1%–5%)	Pillow flow	5
	2-11	132.91	133.12	Aphyric cryptocrystalline to fine-grained basalt	Sparsely vesicular (0%–5%)	Pillow flow	2–5
	2-12	133.12	133.66	Aphyric cryptocrystalline basalt	Sparsely vesicular (0%–3%)	Pillow flow	2–4
	2-13	133.66	133.73	Breccia - hyaloclastite			
	2-14	133.73	134.74	Aphyric cryptocrystalline to fine-grained basalt	Sparsely vesicular (0%–3%)	Pillow flow	3–10
	2-15	134.74	135.29	Aphyric cryptocrystalline basalt	Sparsely vesicular (0%–3%)	Pillow flow	3–4
	2-16	135.29	135.63	Aphyric cryptocrystalline basalt	Sparsely vesicular (0%–1%)	Pillow flow	2
	2-17	135.63	142.58	Aphyric cryptocrystalline to fine-grained basalt	Mostly nonvesicular (0%–0.5%)	Pillow flow	0–5
	2-18	142.58	143.46	Aphyric cryptocrystalline basalt	Sparsely vesicular (0%–3%)	Pillow flow	1–5
3	3	143.46	145.17	Aphyric medium-grained basalt	Nonvesicular	Massive flow	1–10
4	4-1	145.17	145.24	Aphyric cryptocrystalline basalt	Nonvesicular	Pillow flow	10
	4-2	145.24	145.38	Aphyric cryptocrystalline basalt	Sparsely vesicular (3%–5%)	Pillow flow	3–10
	4-3	151.70	151.83	Aphyric medium/fine-grained basalt	Nonvesicular	Massive/Pillow flow	6
	4-4	151.83	152.02	Aphyric cryptocrystalline basalt	Sparsely vesicular (0%–3%)	Pillow flow	4
	4-5	152.02	152.55	Aphyric cryptocrystalline to fine-grained basalt	Sparsely vesicular (0%–5%)	Pillow flow	0–3
	4-6	152.55	152.65	Aphyric cryptocrystalline basalt	Sparsely vesicular (3%)	Pillow flow	2–3
	4-7	152.65	153.63	Aphyric cryptocrystalline basalt	Sparsely vesicular (0%–3%)	Pillow flow	2–8
	4-8	153.63	154.41	Aphyric cryptocrystalline to fine-grained basalt	Sparsely vesicular (0%–5%)	Pillow flow	1–6
5	5	161.30	173.24	Sedimentary-plutonic-volcanic breccia			
6	6-1	173.24	173.38	Plagioclase-olivine-phyric fine-grained basalt	Sparsely vesicular (3%)	Massive flow	~1
	6-2	173.38	183.10	Plagioclase-olivine-phyric fine-grained basalt	Sparsely vesicular (0%–5%)	Massive flow	1–6
	6-3	183.21	191.24	Plagioclase-olivine-phyric fine-grained basalt	Sparsely vesicular (0%–5%)	Massive flow	1–6
7	7-1	191.24	191.33	Aphyric cryptocrystalline basalt	Sparsely vesicular (0%–3%)	Pillow flow	5
	7-2	191.33	191.85	Aphyric cryptocrystalline to microcrystalline basalt	Sparsely vesicular (0.5%–3%)	Pillow flow	0–8
	(7-3)	199.70	200.10	Plagioclase-olivine-phyric microcrystalline basalt	Sparsely vesicular (0.5%–5%)	Massive flow	3
	7-4	200.10	200.33	Aphyric cryptocrystalline basalt	Very sparsely vesicular (0%–0.5%)	Pillow flow	0–5
	7-5	200.33	200.91	Aphyric cryptocrystalline to microcrystalline basalt	Sparsely vesicular (0.5%–3%)	Pillow flow	0–20
	7-6	200.95	201.44	Aphyric cryptocrystalline to microcrystalline basalt	Sparsely vesicular (0%–3%)	Pillow flow	3–4
	7-7	201.44	201.93	Aphyric cryptocrystalline to microcrystalline basalt	Sparsely vesicular (0%–3%)	Pillow flow	0–6
8	8	201.93	202.76	Aphyric fine- to medium-grained basalt	Mostly nonvesicular (0%–1%)	Massive flow	6–10

Table T6. Summary of primary and secondary mineralogy determined by thin section microscopy observation and X-ray diffraction (XRD). (Continued on next two pages.)

Core, section (Piece)	Lith. unit	Thin section	Rock name	Grain size	Texture	Thin section		XRD	
						Primary minerals	Secondary minerals	Primary minerals	Secondary minerals
336-U1382A-									
3R-2 (11)	1–3	1	Aphyric sparsely vesicular basalt	Medium grained	Granular to intersertal	Olivine Plagioclase Clinopyroxene Fe-Ti oxide Sulfide	FeOOH‡ Carbonate Clay	Mixed plagioclase (mostly anorthite) Mixed diopside and augite olivine	Phillipsite Smectite/Zeolite*
3R-3 (3)	1–4	2	Aphyric avesicular basalt	Medium grained	Subophitic	Olivine Plagioclase Clinopyroxene Fe-Ti oxide Sulfide	Clay Palagonite Clay + FeOOH	Mixed plagioclase (mostly anorthite) Mixed diopside and augite olivine	Celadonite Smectite/Zeolite*
3R-4 (11)	1–4	3	Aphyric sparsely vesicular basalt	Medium grained	Subophitic	Olivine Plagioclase Clinopyroxene Fe-Ti oxide Sulfide	Clay	Mixed plagioclase (mostly anorthite) Mixed diopside and augite olivine	Celadonite Zeolite (Chabazite†)
4R-1 (10)	2–2	4	Aphyric avesicular basalt	Crypto- to microcrystalline	Aphyric	Olivine Plagioclase Clinopyroxene Fe-Ti oxide Sulfide	Clay Clay + FeOOH	Mixed plagioclase (mostly anorthite) Mixed diopside and augite olivine	
4R-3 (8)	2–7	5	Aphyric avesicular basalt	Microcrystalline	Aphyric	Olivine Plagioclase Clinopyroxene Fe-Ti oxide Sulfide	Clay Clay + FeOOH	Mixed plagioclase (mostly anorthite) Mixed diopside and augite olivine (at detection limit)	Celadonite
4R-3 (9)	2–7	6	Aphyric avesicular basalt	Fine grained	Intersertal	Olivine Plagioclase Clinopyroxene Fe-Ti oxide Sulfide	Clay FeOOH Pyrite	Mixed plagioclase (mostly anorthite) Mixed diopside and augite olivine	Celadonite
5R-1 (7)	2–9	7	Aphyric sparsely vesicular basalt	Microcrystalline	Aphyric	Olivine Plagioclase Clinopyroxene Fe-Ti oxide	FeOOH‡ Clay Zeolite	Mixed plagioclase (mostly anorthite) Mixed diopside and augite olivine (at detection limit)	
5R-3 (5)	2–15	8	Aphyric sparsely vesicular basalt	Microcrystalline	Aphanitic	Olivine Plagioclase Clinopyroxene Fe-Ti oxide	Clay	Mixed plagioclase (mostly anorthite) Mixed diopside and augite olivine	Zeolite (Chabazite†)
6R-3 (2B)	4–1	9	Aphyric avesicular basalt	Fine grained	Intersertal to ophitic	Olivine Plagioclase Clinopyroxene Fe-Ti oxide Sulfide	Clay	Mixed plagioclase (mostly anorthite) Mixed diopside and augite olivine	
7R-1 (14)	4–5	10	Aphyric sparsely vesicular basalt	Fine grained	Subophitic to intersertal	Olivine Plagioclase Clinopyroxene Fe-Ti oxide Sulfide	FeOOH‡ Clay Zeolite	Mixed plagioclase (mostly anorthite) Mixed diopside and augite, olivine, and quartz (at detection limit)	
7R-2 (12)	4–8	11	Aphyric sparsely vesicular basalt	Glassy to microcrystalline	Glassy to spherulitic to variolitic	Olivine Plagioclase Fe-Ti oxide Sulfide	Clay	Mixed plagioclase (mostly anorthite) Mixed diopside and augite olivine	Celadonite

Table T6 (continued). (Continued on next page.)

Core, section (Piece)	Lith. unit	Thin section	Rock name	Grain size	Texture	Thin section		XRD	
						Primary minerals	Secondary minerals	Primary minerals	Secondary minerals
7R-1 (22)	4–7	12	Aphyric sparsely vesicular basalt	Microcrystalline	Intersertal	Olivine Plagioclase Clinopyroxene Fe-Ti oxide	Clay FeOOH[‡]	Mixed plagioclase (mostly anorthite) Mixed diopside and augite olivine	Zeolite (Chabazite[†])
8R-1 (4)	5	14	Olivine gabbro	Coarse to medium grained	Porphyroclastic	Plagioclase Clinopyroxene Olivine Ilmenite	Serpentine Magnetite Chlorite Tremolite Prehnite Clinozoisite Clay		
9R-1 (5)	5	15	Olivine gabbro mylonite	Medium to fine grained	Mylonitic	Olivine Plagioclase Clinopyroxene Ilmenite			
9R-1 (12)	5	16	lherzolite	Coarse to medium grained	Coarse granular	Olivine Plagioclase Clinopyroxene Spinel Orthopyroxene	Calcite Magnetite Serpentine Plagioclase Pyrite Manganese**		
9R-1 (14b)	5	17	Harzburgite	Coarse grained	Coarse granular	Olivine Clinopyroxene Spinel Orthopyroxene	Serpentine Calcite Magnetite Plagioclase Manganese**		
8R-4 (6)	5	18	Harzburgite	Coarse grained	Coarse granular	Olivine Orthopyroxene Clinopyroxene Spinel	Serpentine Calcite Manganese**		
8R-4 (3)	5	19	Olivine gabbro	Coarse grained	Porphyroclastic	Olivine Plagioclase Clinopyroxene Ilmenite	Chlorite Sericite Magnetite		
8R-4 (8)	5	20	lherzolite	Coarse grained	Coarse granular	Olivine Orthopyroxene Clinopyroxene Spinel Plagioclase	Serpentine Magnetite Chlorite		
9R-2 (3)	5	21	Plagioclase-phyric avesicular basalt	Crypto- to microcrystalline	Hyaloophitic to aphanitic	Olivine Plagioclase Clinopyroxene Fe-Ti oxide	Oxide Clay Clay + FeOOH[‡]	Mixed plagioclase (mostly anorthite) Mixed diopside and augite olivine	
9R-3 (3)	6–2	22	Plagioclase-phyric sparsely vesicular basalt	Fine grained	Intersertal	Olivine Plagioclase Clinopyroxene Fe-Ti oxide	Clay Zeolite	Mixed plagioclase (mostly anorthite) Mixed diopside and augite olivine	Zeolite (Chabazite[†]) Celadonite
10R-2 (10)	6–2	23	Plagioclase-phyric sparsely vesicular basalt	Crypto- to microcrystalline	Aphanitic	Olivine Plagioclase Clinopyroxene Fe-Ti oxide	Clay Clay + FeOOH[‡] Pyrite	Mixed plagioclase (mostly anorthite) Mixed diopside and augite olivine	Possible carbonate

Table T6 (continued).

						Thin section		XRD	
Core, section (Piece)	Lith. unit	Thin section	Rock name	Grain size	Texture	Primary minerals	Secondary minerals	Primary minerals	Secondary minerals
10R-3 (11)	6–3	24	Plagioclase-olivine-phyric sparsely vesicular basalt	Fine grained	Intersertal	Olivine Plagioclase Fe-Ti oxide Sulfide	Clay Clay + FeOOH[‡] Carbonate	Mixed plagioclase (mostly anorthite) Mixed diopside and augite olivine	Zeolite (Chabazite[†])
12R-1 (18)	7–5	25	Aphyric sparsely vesicular basalt	Microcrystalline to fine grained	Intersertal	Olivine Plagioclase Fe-Ti oxide Sulfide	Clay Clay + FeOOH[‡] Pyrite	Mixed plagioclase (mostly anorthite) Mixed diopside and augite olivine	
12R-1 (21)	7–5	26	Aphyric sparsely vesicular basalt	Fine grained	Intersertal	Olivine Plagioclase Clinopyroxene Fe-Ti oxide	Clay Clay + FeOOH[‡]	Mixed plagioclase (mostly anorthite) Mixed diopside and augite olivine	Phillipsite
12R-3 (4)	8	27	Aphyric avesicular basalt	Fine to medium grained	Subophitic	Olivine Plagioclase Clinopyroxene Fe-Ti oxide	Clay + FeOOH[‡]	Mixed plagioclase (mostly anorthite) Mixed diopside and augite olivine	Celadonite Smectite/Zeolite* Zeolite (Chabazite[†])
5R-1 (22)	2–13	NA						Forsterite	Phillipsite-Na celadonite

* = Potential smectite, but smectite/zeolite regions are overlapping and unresolvable. † = tentatively identified as chabazite (Ca-bearing zeolite). ‡ = iron oxyhydroxide. ** = manganese oxides and/or oxyhydroxide.

Table T7. Shipboard geochemical analyses, Hole U1382A.

	336-U1382A-																		
Core, section:	3R-2	3R-3	3R-4	4R-1	4R-3	4R-3	5R-1	5R-3	6R-3	7R-1	7R-1	7R-2	9R-2	9R-3	10R-2	10R-3	12R-1	12R-1	12R-3
Top depth (mbsf):	115.79	116.47	118.55	123.59	126.15	126.20	132.82	135.45	144.98	152.46	152.93	153.85	172.52	174.00	182.98	184.17	200.53	200.70	202.55
Bottom depth (mbsf):	115.81	116.50	118.59	123.63	126.18	126.23	132.86	135.48	145.00	152.49	152.96	153.88	172.54	174.03	183.02	184.20	200.56	200.74	202.58
Major element oxide (wt%):																			
SiO_2	48.42	48.82	49.04	48.57	48.90	49.56	48.61	49.65	49.31	49.61	49.75	49.21	49.02	49.85	49.96	49.74	50.27	48.75	50.59
TiO_2	1.45	1.64	1.55	1.73	1.76	1.61	1.78	1.62	1.62	1.67	1.63	1.64	1.43	1.35	1.46	1.37	1.65	1.77	1.67
Al_2O_3	15.42	16.32	14.69	16.08	16.47	15.15	16.63	15.23	15.10	15.56	15.20	15.18	18.16	17.66	17.77	17.56	15.02	16.09	15.44
$Fe_2O_3^T$	12.10	12.94	12.03	12.87	12.72	11.55	13.70	11.66	11.57	12.54	11.54	12.24	10.12	8.77	9.92	9.28	10.68	11.29	10.45
MgO	7.61	5.41	9.45	6.16	5.32	8.31	4.48	7.83	8.72	6.10	7.85	8.09	6.49	6.95	5.49	7.20	8.23	6.97	7.18
CaO	11.51	11.19	10.03	11.01	11.04	10.50	10.89	10.56	10.28	10.94	10.53	10.44	11.46	12.21	11.88	11.75	10.98	11.69	11.27
Na_2O	3.19	3.27	2.95	3.20	3.27	3.02	3.39	3.06	3.12	3.20	3.14	2.92	2.88	2.85	3.19	2.88	2.81	3.03	3.02
K_2O	0.16	0.23	0.11	0.19	0.30	0.15	0.29	0.24	0.12	0.22	0.22	0.14	0.31	0.25	0.17	0.08	0.18	0.20	0.21
P_2O_5	0.15	0.19	0.15	0.19	0.23	0.15	0.24	0.16	0.16	0.16	0.14	0.16	0.14	0.13	0.16	0.13	0.17	0.20	0.17
Trace element (ppm):																			
Ba	9.03	10.5	7.77	11.1	11.9	6.10	16.8	8.36	8.42	10.9	8.64	10.3	12.2	6.34	8.44	5.41	6.80	9.07	8.56
Co	61.1	59.4	60.2	71.9	77.8	63.1	61.5	89.6	70.4	80.5	59.8	77.5	78.2	54.6	56.7	47.8	57.7	65.5	51.0
Cr	315	318	264	283	285	267	271	270	270	277	271	271	247	222	222	235	280	311	294
Cu	60.9	80.8	77.9	76.2	85.2	75.3	81.2	78.8	72.7	81.5	75.3	78.2	68.6	73.2	77.2	92.2	69.1	72.5	69.3
Ni	232	170	207	153	106	175	144	177	186	161	199	169	103	120	73.1	98.3	130	126	94.8
Sc	37.2	40.1	37.4	41.2	42.3	38.4	41.7	39.2	38.4	40.6	39.0	39.8	35.2	33.6	37.0	34.9	39.5	42.9	39.7
Sr	169	156	129	166	158	154	162	150	153	147	164	158	176	181	186	191	154	162	169
V	259	305	273	318	339	283	332	291	282	301	286	297	247	249	273	253	304	346	299
Y	33.7	37.1	34.1	39.9	40.0	36.9	39.0	36.6	37.6	38.1	39.0	37.7	30.9	29.3	32.9	30.8	37.1	40.2	35.7
Zn	82.4	97.5	80.6	96.1	102	86.8	90.6	92.4	85.7	80.0	89.4	62.6	44.4	45.5	69.0	64.6	43.7	69.2	37.9
Zr	91.1	107	98.4	113	116	108	114	106	103	110	107	109	99.7	91.6	104	96.2	116	123	119
Volatile element (wt%):																			
LOI	2.69	1.56	0.36	0.74	1.67	0.42	1.77	0.64	0.43	1.86	0.47	0.03	1.00	0.67	0.22	0.56	0.44	0.54	1.03
Total carbon	0.62	0.38	0.33	0.29	0.3	0.34	0.31	0.31	0.34	0.43	0.32	0.29	0.31	0.38	0.28	0.29	0.3	0.3	0.3
Nitrogen	0.25	0.25	0.26	0.23	0	0.26	0.24	0.24	0.26	0.24	0.25	0.22	0.25	0.23	0.21	0.22	0.23	0.24	0.24

LOI = loss on ignition.

Table T8. Sedimentary calcium carbonate and inorganic carbon, Hole U1382A.

Core, section	Depth (mbsf) Top	Depth (mbsf) Bottom	Calcium carbonate (wt%)	Inorganic carbon (wt%)
336-U1382A-				
8R-2 (squeezed)	162.76	162.89	23.1	2.77
8R-2 (squeezed)	162.76	162.89	20.8	2.49
8R-3	163.03	163.05	36.2	4.34
8R-3	163.03	163.05	36.4	4.36
8R-3 (squeezed)	163.06	163.15	35.9	4.30
8R-3 (squeezed)	163.06	163.15	35.8	4.29
8R-4	163.52	163.54	43.5	5.21
8R-4	163.52	163.54	43.9	5.27

Table T9. Distribution of microfossils in interbasalt sediments, Hole U1382A.

			Calcareous nannofossils							Other fossils			Minerals		
Core, section, interval (cm)	Smear slide	Lithology	*Discoaster quinqueramus* (NN11)	*Discoaster brouweri* (NN9–NN18)	*Discoaster variabilis* (NN9–NN16)	*Discoaster triradiatus* (NN9–NN21)	*Amaurolithus* spp. (NN11B–NN14)	Other nannoliths	Coccoliths	Planktonic foraminifers	Radiolarians	Dinoflagellates	Volcanic glass	Other minerals	Amorphous matter
336-U1382A-															
8R-2, 1–2	4	Ooze	xx	xx	xxx	—	—(?)	x	+		—		x	x	xx
8R-2, 6–7	5	Ooze	x	xx	xxx			x	+				xx	x	x
8R-2, 13–14	6	Ooze	xx	xx	xxx			x	+	—	—		x	x	x
8R-2, 26–34	10	Ooze	x	xx	xxx			x	x				xx	x	xx
8R-3, 1–2	7	Ooze	x	xx	xxx			x	x				x	x	x
8R-3, 7–8	8	Ooze	xx	xx	xxx	—		x	+	—	—		x	x	x
8R-3, 12–13	9	Ooze	x	x	xxx			x	+				xx	x	x
8R-3, 22–42	11	Ooze	xx	x	xxx			x	x				x	x	xx
8R-4, 7–8	1	Ooze	x	x	xxx			x	+				xx	x	x
8R-4, 15–16	2	Ooze	x	xx	xxx	—		x	x	—	—		x	x	x
8R-4, 24–25	3	Ooze	x	x	xxx			x	+			—	xx	x	x
8R-4, 37–38	12	Breccia	x	x	xx	—		x	x	—			xxx	xx	xx

xxx = abundant (>30%), xx = common (10%–30%), x = few (5%–10%), + = rare (1%–5%), — = trace (<1%).

Table T10. List of whole-round samples collected for microbiological analysis from Hole U1382A, along with subsamples collected and results of microsphere contamination checks. (Continued on next page.)

Label identifier	Depth (mbsf)		Description	DNA/RNA	Isotopes	Archive	DEBI-pt	Geochem pooled	Microspheres	
	Top	Bottom							First wash	Final wash
336-U1382A-2R-1-MBIOA	110.03	110.10	Massive, micro- to cryptocrystalline, minor yellow-brown alteration	x	x	x	x		Yes	No
336-U1382A-2R-1-MBIOC	110.55	110.63	Massive, minor red-yellow-brown alteration	x	x	x	x		Yes	Yes
336-U1382A-2R-1-MBIOB	110.75	110.81	Massive, minor red-yellow-brown alteration	x	x				Yes	Yes
336-U1382A-3R-1-MBIOB	113.63	113.70	Massive, oxidized, white-yellow-brown alteration in vein	x	x	x			Yes	No
336-U1382A-3R-1-MBIOA	114.27	114.45	Massive, oxidized, yellow-red-brown-white alteration	x	x	x			Yes	No
336-U1382A-3R-2-MBIOB	115.62	115.75	Massive, yellow-white-brown alteration in vein	x	x	x			No	No
336-U1382A-3R-2-MBIOA	116.03	116.10	Massive, extensive yellow-orange-brown alteration in vein	x	x	x			Yes	No
336-U1382A-3R-3-MBIOB	116.25	116.33	Massive, patchy orange-brown alteration	x	x	x			Yes	Yes
336-U1382A-3R-3-MBIOA	117.20	117.29	Massive, patchy orange-brown alteration	x	x	x			Yes	No
336-U1382A-3R-4-MBIOB	117.79	117.84	Massive, mostly brown oxidized halo	x	x	x			Yes	Yes
336-U1382A-3R-4-MBIOA	118.20	118.32	Massive, one end has 5 cm-deep brown oxidation halo	x	x		x		No	No
336-U1382A-4R-1-MBIOA	123.04	123.07	Aphyric cryptocrystalline basalt, extensive red-brown alteration	x	x				No	No
336-U1382A-4R-1-MBIOB	123.21	123.27	Aphyric cryptocrystalline basalt, gray-brown alteration	x	x	x			Yes	No
336-U1382A-4R-1-MBIOC	124.12	124.18	Aphyric cryptocrystalline basalt, extensive red-brown alteration	x	x	x		x	No	No
336-U1382A-4R-2-MBIOF	124.55	124.60	Fine-grained basalt, glassy margin, patchy red alteration	x	x	x			Yes	Yes
336-U1382A-4R-2-MBIOD	124.57	124.64	Aphyric fine-grained basalt, glassy margin, variolitic alteration	x	x	x			No	No
336-U1382A-4R-2-MBIOE	124.72	124.79	Fine-grained basalt, fractured, red alteration, altered vesicular	x	x	x			No	No
336-U1382A-5R-1-MBIOA	132.50	132.56	Aphyric, glassy margin, red alteration	x	x		x	x	No	No
336-U1382A-5R-1-MBIOB	133.18	133.25	Massive, aphyric, red alteration	x	x	x			No	No
336-U1382A-5R-1-MBIOC	133.38	133.48	Massive, aphyric, roller, red-brown alteration, vein, vesicular	x	x	x			Yes	No
336-U1382A-5R-1-MBIOD	133.69	133.72	Massive, aphyric, extensive red-white alteration, vein	x	x	x	x		Yes	No
336-U1382A-5R-2-MBIOE	134.08	134.17	Aphyric, variolitic, patchy alteration	x	x	x			No	No
336-U1382A-5R-2-MBIOF	134.47	134.57	Aphyric, sparsely vesicular, minimal alteration	x	x	x			No	No
336-U1382A-6R-1-MBIOA	142.40	142.50	Aphyric, cryptocrystalline, less vesicular, patchy alteration	x	x	x			Yes	Yes
336-U1382A-6R-1-MBIOB	142.71	142.76	Aphyric, cryptocrystalline, less vesicular, patchy alteration	x	x	x			No	No
336-U1382A-6R-1-MBIOC	143.24	143.34	Aphyric, cryptocrystalline, less vesicular, patchy alteration	x	x	x			Yes	No
336-U1382A-6R-2-MBIOD	143.74	143.83	Aphyric, cryptocrystalline, less vesicular, patchy alteration	x	x	x			Yes	No
336-U1382A-7R-1-MBIOA	153.06	153.15	Very fine grained, one end with orange-green-brown oxidation halo	x					Yes	No
336-U1382A-7R-2-MBIOB	153.88	153.93	Aphyric, glassy margin, red and orange-brown alteration	x	x	x	x	x	No	No
336-U1382A-8R-1-MBIOA	161.30	161.37	Ultramafic, pyroxene, evidence of low-temperature alteration	x	x			x	Yes	No
336-U1382A-8R-1-MBIOB	161.48	161.54	Porphyritic basalt	x	x	x		x	No	No
336-U1382A-8R-1-MBIOC	162.02	162.07	Ultramafic with large pyroxene porphyroclasts	x	x				No	No
336-U1382A-8R-2-MBIOF	162.85	162.93	Orange-brown sediment with small (<1 mm) basalt clasts	x					Yes	No
336-U1382A-8R-3-MBIOG	163.15	163.35	Gray-brown + orange-brown sediment with small (<1 mm) basalt clasts	x					No	No
336-U1382A-8R-4-MBIOD	163.77	163.84	Sedimentary breccia with basalt clasts, rusty colored, extensive carbonate veins	x	x			x	No	No
336-U1382A-8R-4-MBIOE	163.97	164.04	Ultramafic (harzburgite?) underneath breccia, carbonate vein	x	x				No	No
336-U1382A-9R-1-MBIOA	171.47	171.52	Massive roller, porphyritic basalt, yellow-brown patchy alteration	x	x	x			No	No
336-U1382A-9R-1-MBIOB	172.00	172.06	Serpentinized breccia, rusty-brown, carbonate vein	x	x	x			Yes	No
336-U1382A-9R-1-MBIOC	172.12	172.18	Sediment near serpentinized breccia	x	x	x			No	No
336-U1382A-9R-2-MBIOD	173.72	173.80	Medium-grained basalt, porphyritic, olivine-plagioclase, patchy rust alteration, vein	x	x	x			No	No
336-U1382A-10R-1-MBIOA	180.75	180.80	Medium-grained basalt, porphyritic, olivine-plagioclase, rust alteration halo	x	x	x			No	No
336-U1382A-10R-1-MBIOB	181.59	181.69	Medium-grained basalt, massive roller, patchy alteration	x	x	x			No	No
336-U1382A-10R-2-MBIOC	183.10	183.20	Medium-grained basalt, massive, porphyritic, vein with white diffuse alteration	x	x	x			No	No
336-U1382A-10R-3-MBIOD	183.70	183.81	Medium-grained basalt, massive, porphyritic, pervasive alteration	x	x	x	x		No	No
336-U1382A-11R-1-MBIOA	190.10	190.19	Medium-grained basalt, massive, porphyritic, yellow-brown alteration in vein	x	x	x			No	No
336-U1382A-11R-1-MBIOB	190.96	191.03	Medium-grained basalt, massive, porphyritic, red-brown alteration in vein	x	x	x			No	No
336-U1382A-12R-1-MBIOA	199.87	199.93	Porphyritic basalt, minor alteration	x	x				Yes	No
336-U1382A-12R-2-MBIOB	201.62	201.72	Aphyric basalt, minor alteration	x	x				No	No
336-U1382A-Drill bit cuttings	0.00	0.10	Sepiolite drilling mud scraped from bit	x					NA	NA

Table T10 (continued).

Label identifier	Depth (mbsf)		Description	DNA/RNA	Isotopes	Archive	DEBI-pt	Geochem pooled	Microspheres	
	Top	Bottom							First wash	Final wash
336-U1382A-Drilling Fluid	0.00	0.10	Sepiolite drilling mud from mud pump	x					NA	NA
			Total:	50	45	35	7	6		

See also the figures in the **“Appendix.”** DEBI-pt = Deep Exploration Biosphere Investigative portable tool. NA = sample not collected.

Table T11. Moisture and density, *P*-wave velocity measurements, and main petrology characteristics for discrete samples, Hole U1382A.

Core, section, interval (cm)	Depth (mbsf)		MAD					*P*-wave velocity (m/s)					Petrology				
	Top	Bottom	Bulk density (g/cm^3)	Dry density (g/cm^3)	Grain density (g/cm^3)	Porosity (%)	Void ratio	*x*	*y*	*z*	All axes Mean	All axes SD	Alteration (%)	Vesicles	Lith. unit	Main lithology	Description
336-U1382A-																	
3R-1W, 9–11	113.39	113.41	2.91	2.86	3.00	4.55	0.05	5783	5909	5886	5859	67	10	0	1–4	Aphyric fine- to medium-grained basalt	Massive flow
3R-2W, 100–102	115.8	115.82	2.85	2.78	3.00	7.52	0.08	5997	—	—	5997	—	17*	0			
3R-3W, 27–29	116.46	116.48	2.88	2.82	2.99	5.91	0.06	5818	5807	5813	5813	6	16*	0			
3R-3W, 69–71	116.88	116.9	2.92	2.87	3.00	4.31	0.05	5961	5938	5847	5915	60	10	0			
3R-3W, 130–132	117.49	117.51	2.92	2.88	2.99	3.65	0.04	5989	5955	5929	5958	30	2	0			
3R-4W, 96–98	118.56	118.58	2.92	2.88	3.00	3.86	0.04	5968	5987	5959	5972	15	3.5*	0			
5R-3W, 29–30	135.45	135.46	2.88	2.84	2.97	4.45	0.05	7380	7436	7289	7368	75	1.5*	2	2–16	Aphyric cryptocrystalline basalt	Pillow flow
6R-3W, 26–28	144.48	144.5	2.90	2.86	2.97	3.48	0.04	6015	5970	5988	6040	28	1.5*	0	3	Aphyric medium-grained basalt	Massive flow
6R-3W, 63–65	144.85	144.87	2.88	2.83	2.97	4.59	0.05	5920	5768	5756	5991	23	5	0			
6R-3W, 75–77	144.97	144.99	2.90	2.86	2.96	3.35	0.03	6022	6073	6026	5815	91	5	0			
7R-1W, 123–125	152.93	152.95	2.89	2.87	2.92	1.86	0.02	7141	7204	7179	7175	32	8*	0	4–7	Aphyric cryptocrystalline basalt	Pillow flow
9R-1W, 102–104	171.92	171.94	3.01	2.98	3.09	3.58	0.04	6559	6410	6800	6590	196	30*	0	5–5	Harzburgite	Coarse- and medium-grained granular to porphyroclastic
9R-2W, 130–132	173.65	173.67	2.78	2.72	2.88	5.43	0.06	5778	5831	5864	5824	44	1	2	6–2	Moderately to highly phyric microcrystalline to fine-grained basalt	Massive flow
9R-3W, 19–21	173.99	174.01	2.78	2.72	2.87	5.20	0.05	5944	6010	6002	5985	36	2*	0			
10R-1W, 34–36	180.84	180.86	2.85	2.81	2.91	3.44	0.04	6477	6514	6502	6498	19	1	3			
10R-1W, 88–90	181.38	181.4	2.83	2.79	2.90	3.84	0.04	6416	6450	6446	6437	18	2	2			
10R-1W, 98–100	181.48	181.5	2.83	2.80	2.89	3.10	0.03	6520	6586	6645	6583	63	2	2			
10R-2W, 49–51	182.4	182.42	2.87	2.83	2.93	3.29	0.03	6123	6084	6083	6097	23	1	2			
10R-2W, 109–111	183	183.02	2.81	2.76	2.92	5.44	0.06	5734	5778	5778	5763	26	15.5*	1			
10R-3W, 82–85	184.17	184.2	2.88	2.85	2.94	3.17	0.03	6423	6186	6528	6379	176	4*	2	6–3	Moderately to highly phyric microcrystalline to fine-grained basalt	Massive flow
11R-2W, 49–51	191.82	191.84	2.86	2.84	2.91	2.57	0.03	6283	6260	6272	6272	11	4	2	7–2	Aphyric cryptocrystalline to microcrystalline basalt	Pillow flow
12R-1W, 82–83	200.52	200.53	2.88	2.85	2.92	2.32	0.02	6738	—	—	6738	—	3*	1	7–5	Aphyric cryptocrystalline to microcrystalline basalt	Pillow flow
12R-3W, 31–33	202.51	202.53	2.87	2.83	2.95	4.24	0.04	5756	5676	5761	5731	48	2*	0	8	Aphyric fine- to medium-grained basalt	Massive flow

* = alteration observed in adjacent thin section. MAD = moisture and density. SD = standard deviation. — = not measured.

Table T12. Thermal conductivity and standard deviation values for rocks, Hole U1382A.

Core, section	Top depth (mbsf)	Mean thermal conductivity (W/[m·K])	Thermal conductivity (σ)
336-U1382A-			
2R1	111.09	1.775	0.011
2R-2	111.18	1.816	0.050
3R-1	114.70	1.878	0.015
3R-1	114.17	1.737	0.011
3R-2	114.85	1.765	0.037
3R-2	115.54	1.567	0.024
3R-3	116.90	1.760	0.048
3R-3	116.90	1.760	0.048
3R-4	118.10	1.847	0.034
4R-2	125.04	1.767	0.014
6R-2	143.53	1.789	0.022
7R-2	153.45	1.738	0.009
8R-1	162.46	1.643	0.011
8R-4	163.91	3.384	0.316
9R-1	171.73	3.386	0.079
9R-2	173.53	1.584	0.055
9R-3	174.00	1.675	0.007
10R-1	180.85	1.729	0.018
10R-2	182.42	1.714	0.007
10R-4	185.54	1.698	0.020
11R-1	190.62	1.678	0.012
12R-1	200.66	1.681	0.039
12R-3	202.71	1.686	0.008

Table T13. Summary of color reflectance values (minimum, maximum, mean, and standard deviation [SD]), Hole U1382A.

	L*	a*	b*	*x*-tristimulus	*y*-tristimulus	*z*-tristimulus
Minimum	10.80	–1.60	–6.00	1.20	1.20	1.20
Maximum	60.90	11.60	24.80	29.20	29.20	26.60
Mean	36.06	0.64	1.24	8.85	9.26	9.57
SD	4.67	1.32	3.40	2.32	2.38	2.66

Table T14. Logging operations summary, Hole U1382A.

Date (2011)	Time (h)	Activity
9 Oct	0215	Downhole logging operations start
9 Oct	0317	AMC I tool string run into hole
9 Oct	0534	Wireline heave compensation optimization performed with tool string entirely in casing
9 Oct	0638	Begin downlog at 4590.1 m WRF
9 Oct	0650	Reach total depth of 4700 m WRF
9 Oct	0654	Begin uplog
9 Oct	0718	Power cycle issue (possible short encountered); tool string power loss (4620 m WRF)
9 Oct	0720	Logging aborted and tool brought back to surface
9 Oct	1110	AMC I tool string rigged down
9 Oct	1218	FMS-HNGS tool string rigged up
9 Oct	1221	FMS-HNGS run into hole
9 Oct	1452	Begin downlog at 4490.8 m WRF; wireline heave compensator was not used because of low heave conditions
9 Oct	1517	Tool string reached total depth at 4703.1 m WRF
9 Oct	1519	Begin first pass
9 Oct	1535	End first pass
9 Oct	1536	Run tool string back down to total depth
9 Oct	1546	Begin second pass
9 Oct	1603	Tool string not able to reenter pipe (4558 m WRF)
9 Oct		Attempted to drop tool string back down; opened and closed calipers numerous times
9 Oct	1612	Preparations made to “carwash” the tool string into the pipe
9 Oct	1812	FMS-HNGS tool string successfully reenters pipe
9 Oct	2110	Tool string back to surface (some visible damage to FMS Pad 3)
9 Oct	2153	FMS-HNGS rigged down and logging operations concluded

AMC I = adapted microbiology combination I, FMS = Formation MicroScanner, HNGS = Hostile Environment Natural Gamma Ray Sonde. Time is reported as ship local (UTC – 3 h).

Appendix

Photographs of whole-round samples taken for microbiology are shown in Figures AF1, AF2, AF3, AF4, AF5, AF6, AF7, AF8, AF9, AF10, AF11, AF12, AF13, AF14, AF15, AF16, AF17, AF18, AF19, AF20, AF21, AF22, AF23, AF24, AF25, AF26, AF27, AF28, AF29, AF30, AF31, AF32, AF33, AF34, AF35, AF36, AF37, AF38, AF39, AF40, AF41, AF42, AF43, AF44, AF45, AF46, and AF47.

Figure AF1. Photograph of microbiology whole-round Sample 336-U1382A-2R-1-MBIOA.

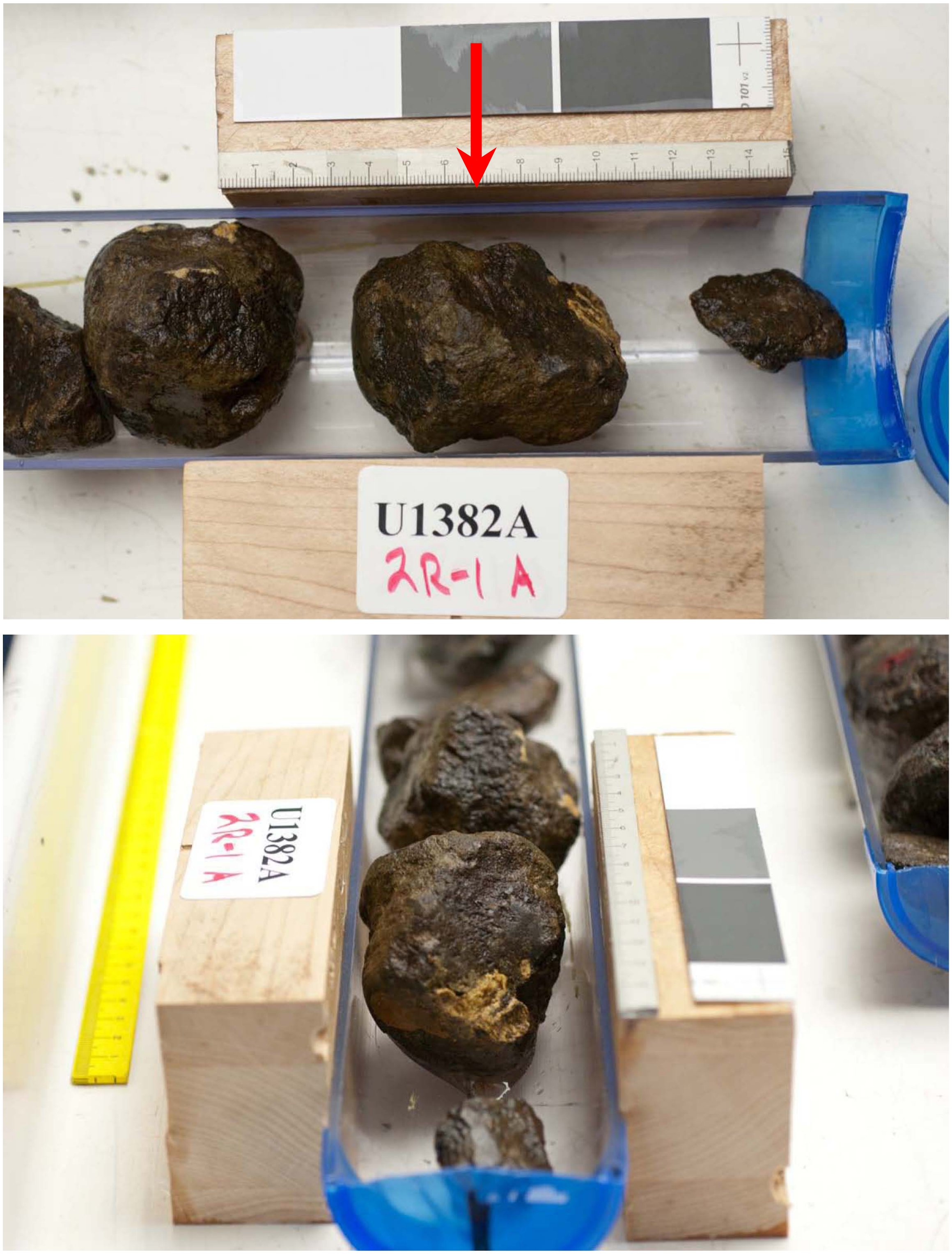

Figure AF2. Photograph of microbiology whole-round Sample 336-U1382A-2R-1-MBIOB.

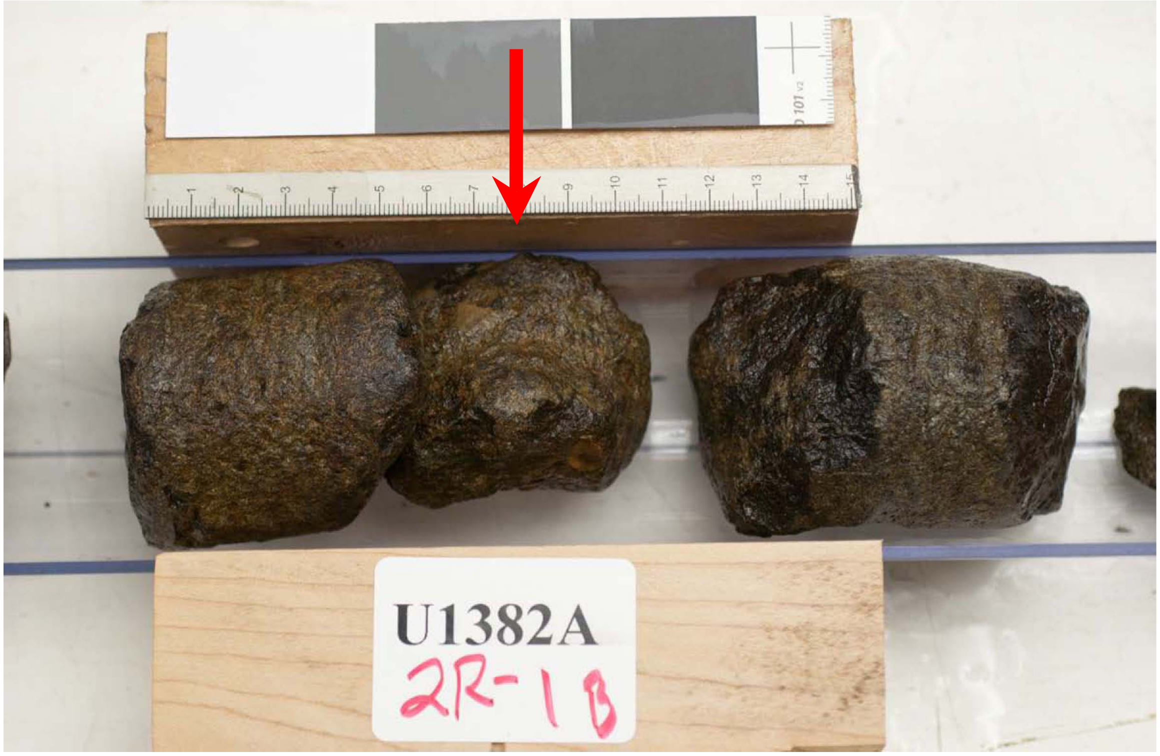

Figure AF3. Photograph of microbiology whole-round Sample 336-U1382A-2R-1-MBIOC.

Figure AF4. Photograph of microbiology whole-round Sample 336-U1382A-3R-1-MBIOA.

Figure AF5. Photograph of microbiology whole-round Sample 336-U1382A-3R-1-MBIOB.

Figure AF6. Photograph of microbiology whole-round Sample 336-U1382A-3R-2-MBIOA.

Figure AF7. Photograph of microbiology whole-round Sample 336-U1382A-3R-2-MBIOB.

Figure AF8. Photograph of microbiology whole-round Sample 336-U1382A-3R-3-MBIOA.

Figure AF9. Photograph of microbiology whole-round Sample 336-U1382A-3R-3-MBIOB.

Figure AF10. Photograph of microbiology whole-round Sample 336-U1382A-3R-4-MBIOA.

Figure AF11. Photograph of microbiology whole-round Sample 336-U1382A-3R-4-MBIOB.

Figure AF12. Photograph of microbiology whole-round Sample 336-U1382A-4R-1-MBIOA.

Figure AF13. Photograph of microbiology whole-round Sample 336-U1382A-4R-1-MBIOB.

Figure AF14. Photograph of microbiology whole-round Sample 336-U1382A-4R-1-MBIOC.

Figure AF15. Photograph of microbiology whole-round Sample 336-U1382A-4R-2-MBIOA.

Figure AF16. Photograph of microbiology whole-round Sample 336-U1382A-4R-2-MBIOB.

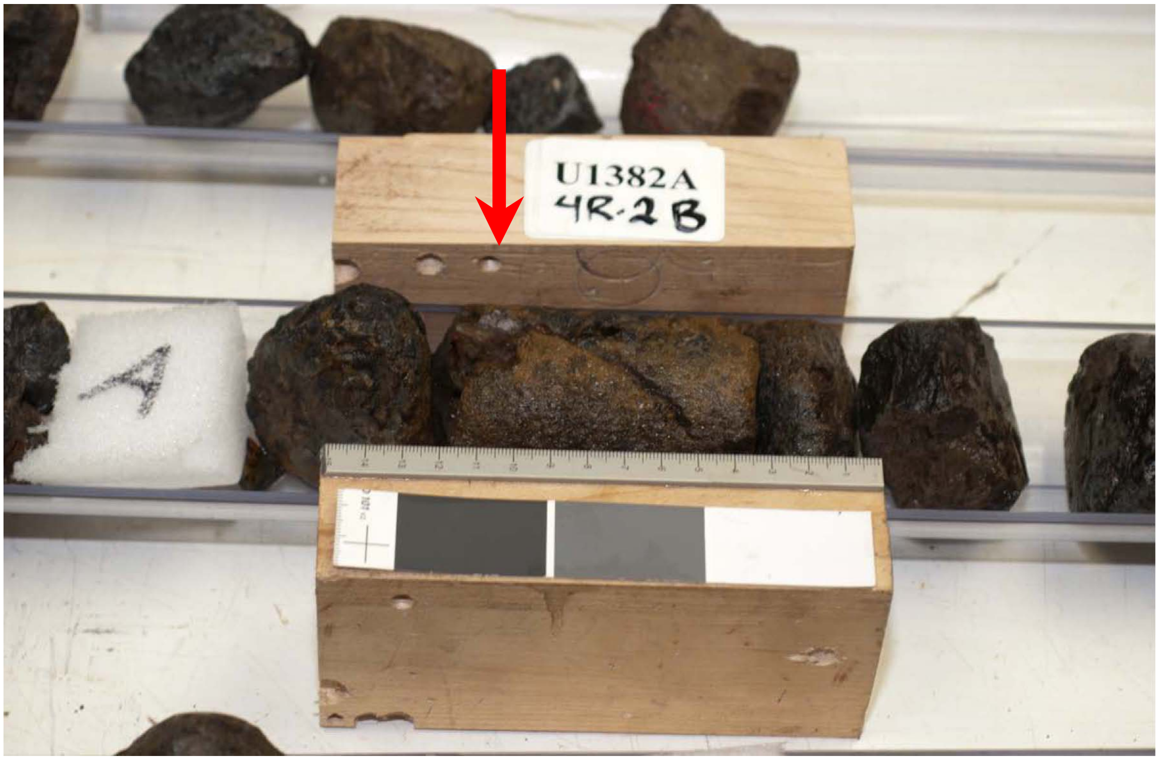

Figure AF17. Photograph of microbiology whole-round Sample 336-U1382A-4R-2-MBIOC.

Figure AF18. Photograph of microbiology whole-round Sample 336-U1382A-5R-1-MBIOA.

Figure AF19. Photograph of microbiology whole-round Sample 336-U1382A-5R-1-MBIOB.

Figure AF20. Photograph of microbiology whole-round Sample 336-U1382A-5R-1-MBIOC.

Figure AF21. Photograph of microbiology whole-round Sample 336-U1382A-5R-1-MBIOD.

Figure AF22. Photograph of microbiology whole-round Sample 336-U1382A-5R-2-MBIOE.

Figure AF23. Photograph of microbiology whole-round Sample 336-U1382A-5R-2-MBIOF.

Figure AF24. Photograph of microbiology whole-round Sample 336-U1382A-6R-1-MBIOA.

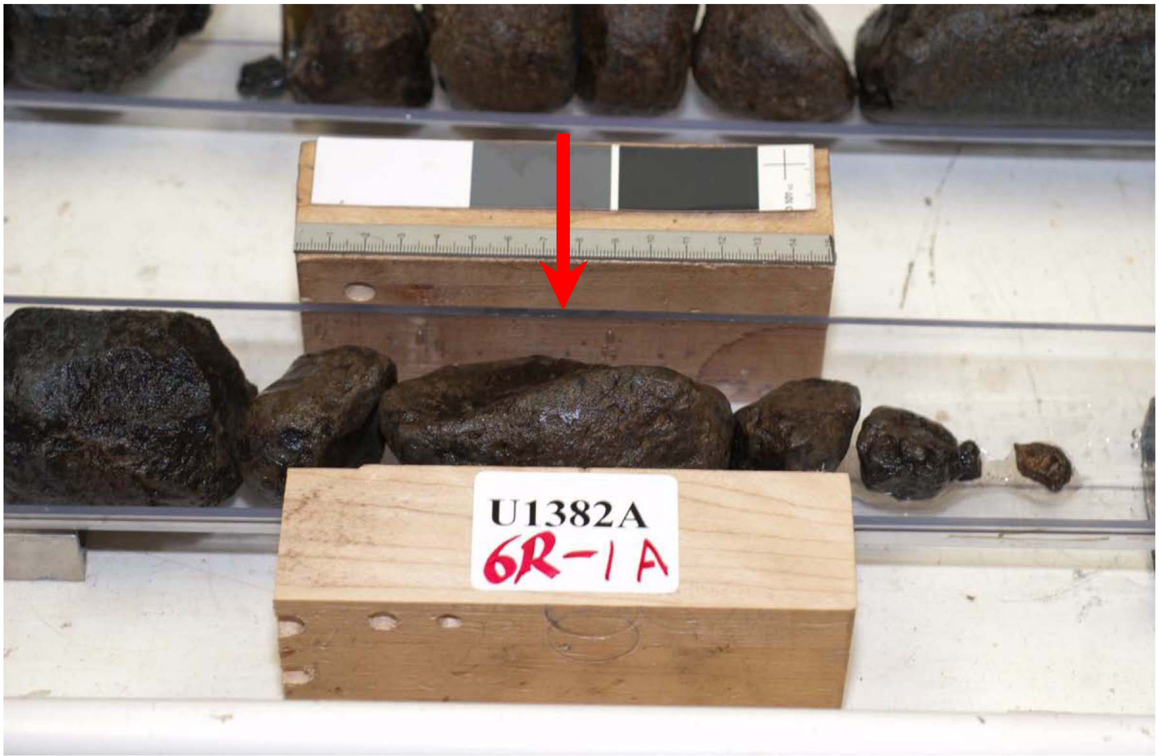

Figure AF25. Photograph of microbiology whole-round Sample 336-U1382A-6R-1-MBIOB.

Figure AF26. Photograph of microbiology whole-round Sample 336-U1382A-6R-1-MBIOC.

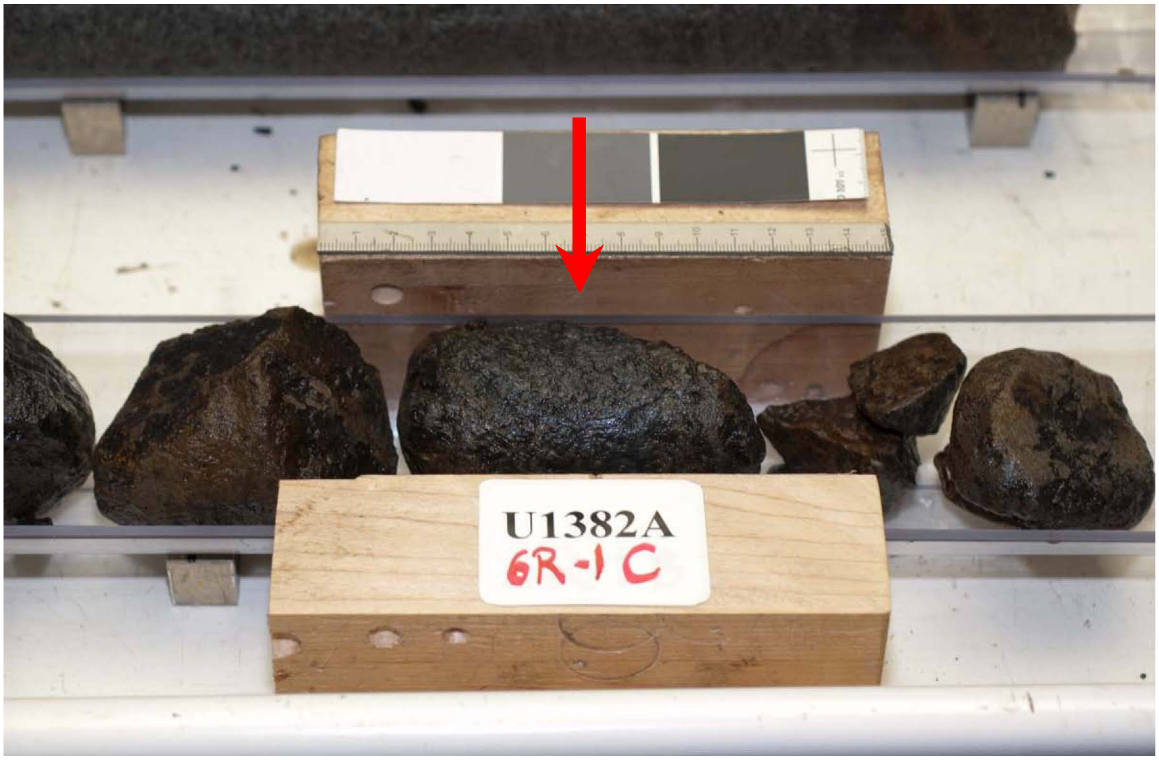

Figure AF27. Photograph of microbiology whole-round Sample 336-U1382A-6R-2-MBIOD.

Figure AF28. Photograph of microbiology whole-round Sample 336-U1382A-7R-1-MBIOA.

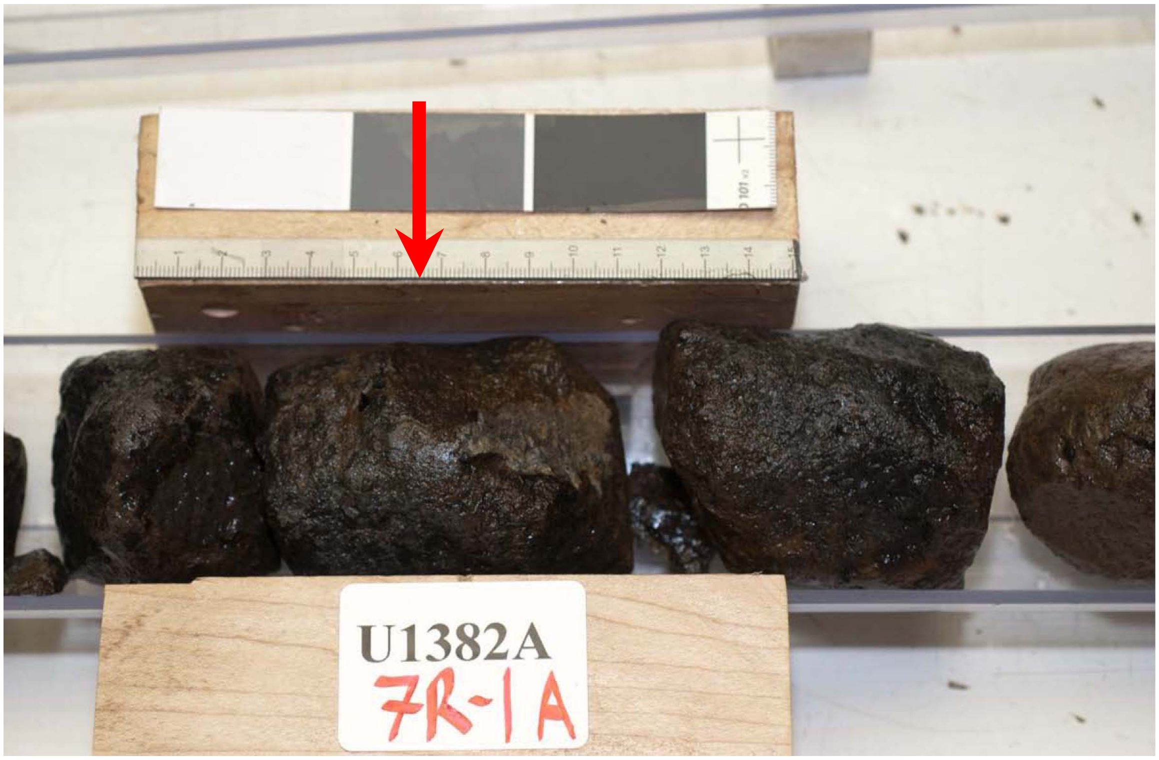

Figure AF29. Photograph of microbiology whole-round Sample 336-U1382A-7R-2-MBIOB.

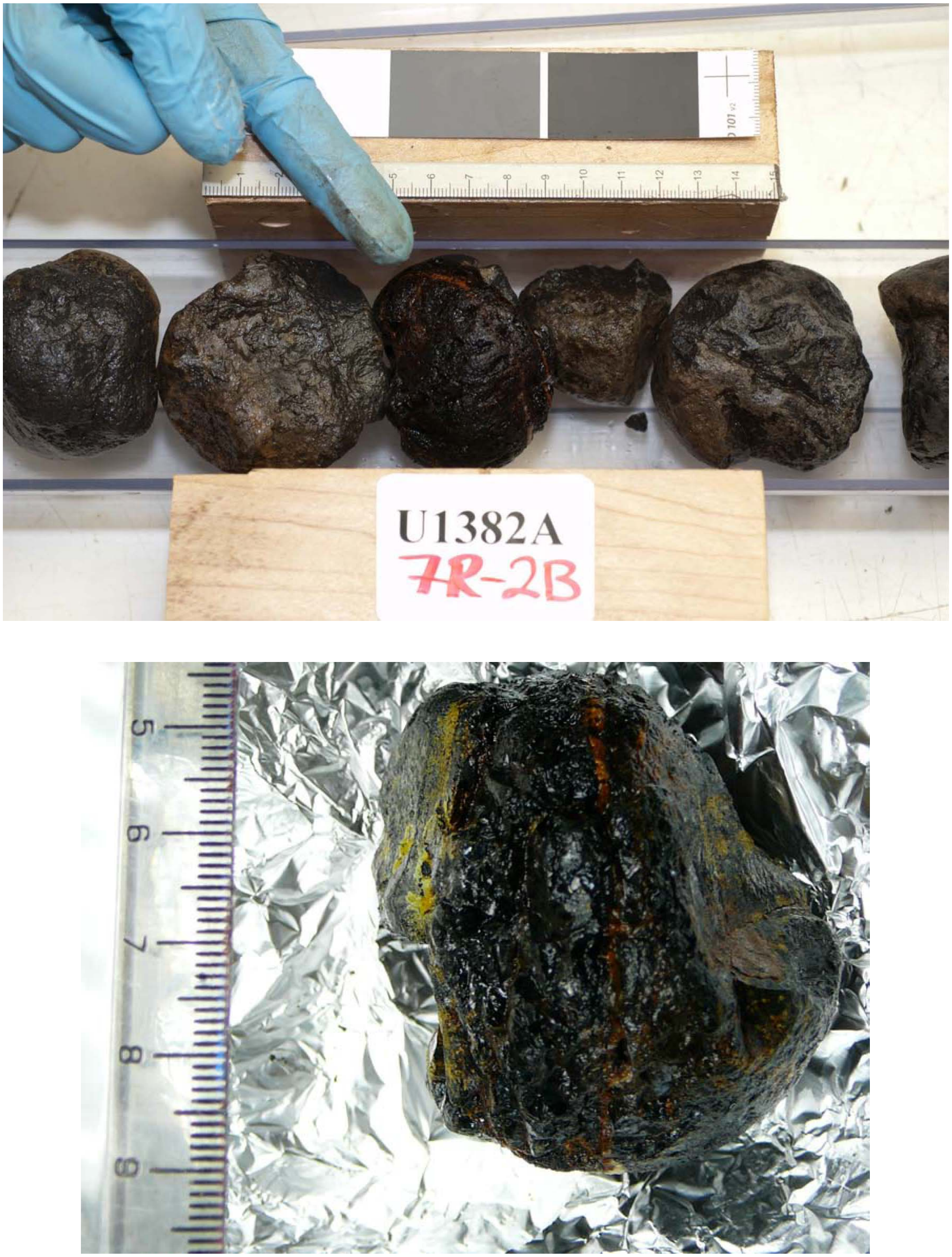

Figure AF30. Photograph of microbiology whole-round Sample 336-U1382A-8R-1-MBIOA.

Figure AF31. Photograph of microbiology whole-round Sample 336-U1382A-8R-1-MBIOB.

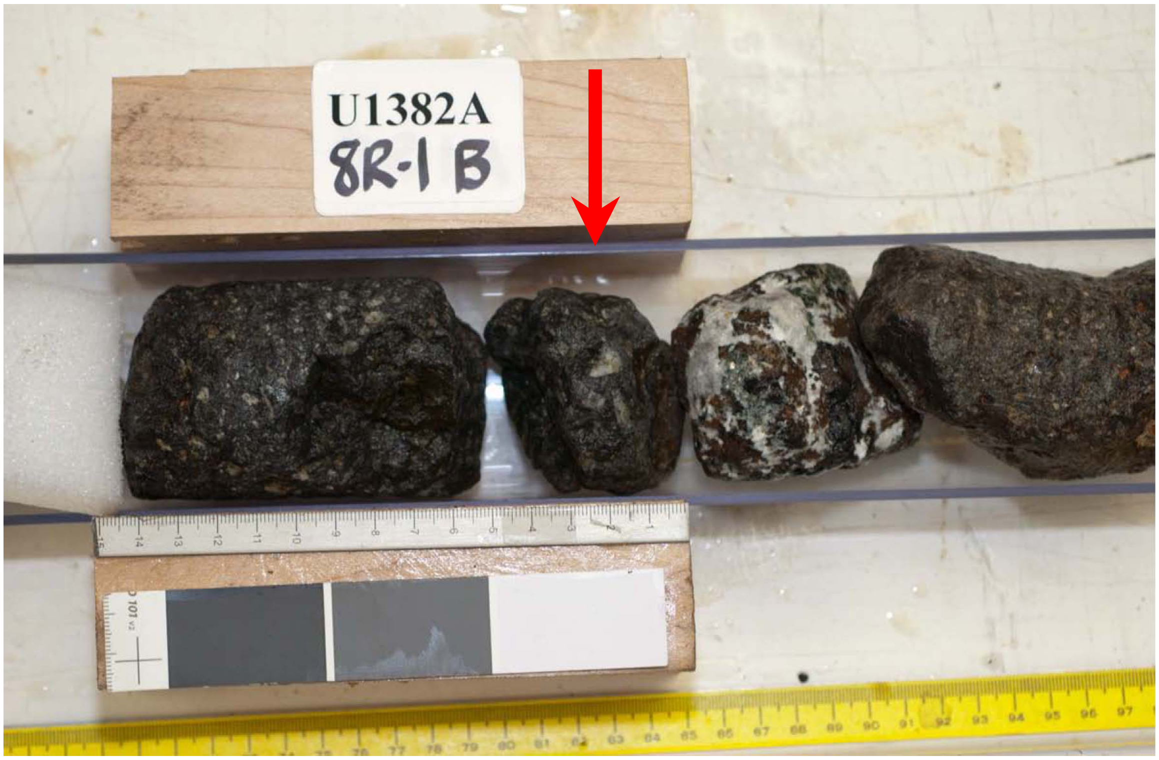

Figure AF32. Photograph of microbiology whole-round Sample 336-U1382A-8R-1-MBIOC.

Figure AF33. Photograph of microbiology whole-round Sample 336-U1382A-8R-4-MBIOD.

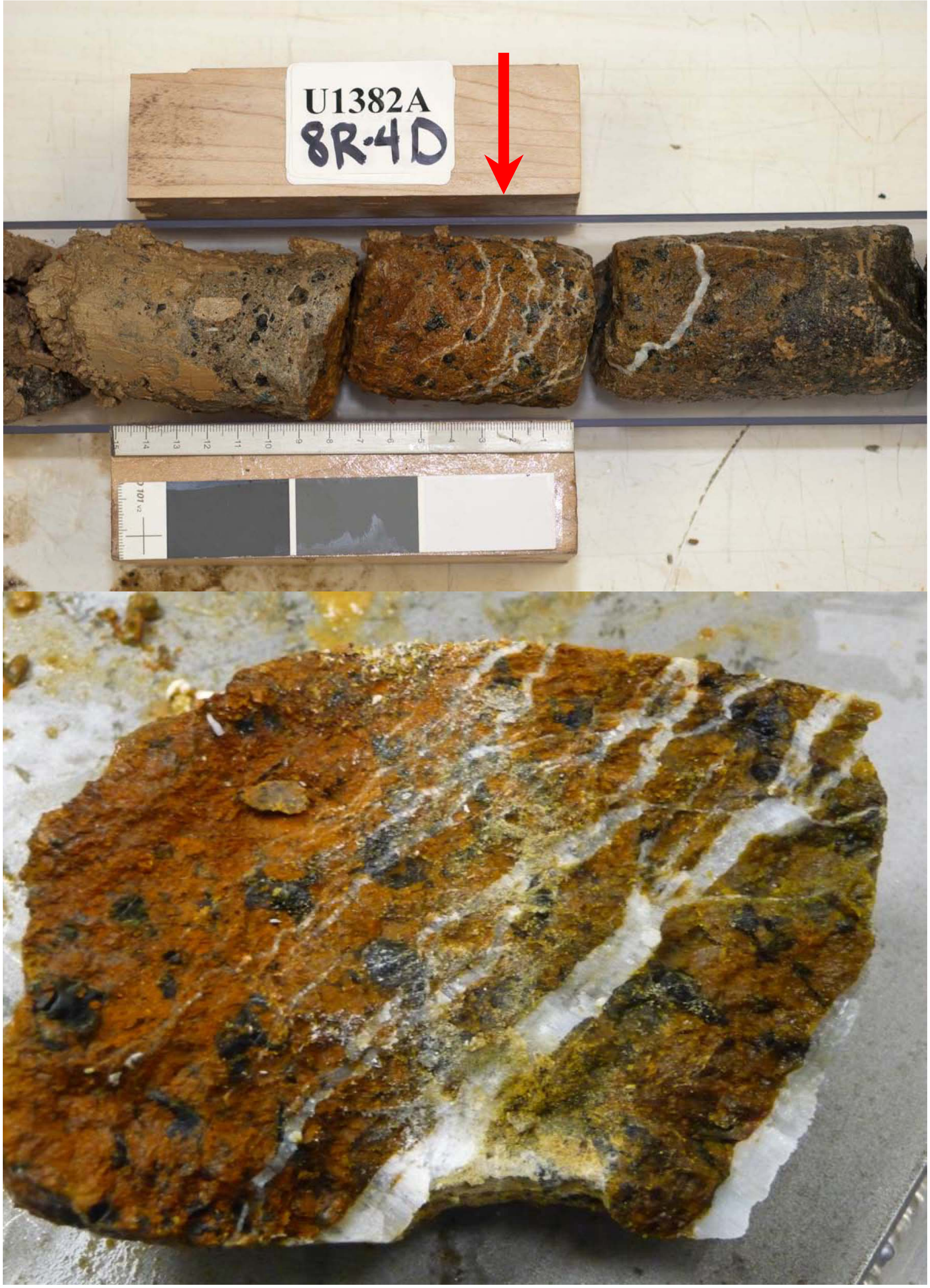

Figure AF34. Photograph of microbiology whole-round Sample 336-U1382A-8R-4-MBIOE.

Figure AF35. Photograph of microbiology whole-round Sample 336-U1382A-8R-MBIOF (sediment).

Figure AF36. Photograph of microbiology whole-round Sample 336-U1382A-9R-1-MBIOA.

Figure AF37. Photograph of microbiology whole-round Sample 336-U1382A-9R-1-MBIOB.

Figure AF38. Photograph of microbiology whole-round Sample 336-U1382A-9R-1-MBIOC.

Figure AF39. Photograph of microbiology whole-round Sample 336-U1382A-9R-2-MBIOD.

Figure AF40. Photograph of microbiology whole-round Sample 336-U1382A-10R-1-MBIOA.

Figure AF41. Photograph of microbiology whole-round Sample 336-U1382A-10R-1-MBIOB.

Figure AF42. Photograph of microbiology whole-round Sample 336-U1382A-10R-2-MBIOC.

Figure AF43. Photograph of microbiology whole-round Sample 336-U1382A-10R-3-MBIOD.

Figure AF44. Photograph of microbiology whole-round Sample 336-U1382A-11R-1-MBIOA.

Figure AF45. Photograph of microbiology whole-round Sample 336-U1382A-11R-1-MBIOB.

Figure AF46. Photograph of microbiology whole-round Sample 336-U1382A-12R-1-MBIOA.

Figure AF47. Photograph of microbiology whole-round Sample 336-U1382A-12R-2-MBIOB.